Creation and manipulation of quantum states in nanostructures

Marcus Schaffry
Linacre College

Thesis submitted for the degree of
Doctor of Philosophy
at the
University of Oxford
Trinity Term 2011

Supervisors: Dr. Brendon W. Lovett
Dr. Simon C. Benjamin
Dr. Erik M. Gauger

to my family and Shobha for all their love and support

Creation and manipulation of quantum states in nanostructures

Marcus Schaffry
Linacre College, University of Oxford
Trinity Term 2011

Abstract of Thesis Submitted for the Degree of Doctor of Philosophy

Nanostructures are promising building blocks for quantum technologies due to their reproducible nature and ability to self-assemble into complex structures. However, the need to control these nanostructures represents a key challenge. Hence, this thesis investigates the manipulation and creation of quantum states in certain nanostructures. The results of this thesis can be applied to quantum information processing and to extremely sensitive magnetic-field measurements.

In the first research chapter, we propose and examine methods for entangling two (remote) nuclear spins through their mutual coupling to a transient optically excited electron spin. From our calculations we identify the specific molecular properties that permit high entangling power gates for different protocols.

In the next research chapter, we investigate another method to create entanglement; this time between two remote electronic spins. This method uses a very sensitive magnetic-field sensor based on a crystal defect that allows the detection of single magnetic moments. The act of sensing the local field constitutes a two-qubit projective measurement. This entangling operation is remarkably robust to imperfections occurring in an experiment.

The third research chapter presents an augmented sensor consisting of a nitrogen-vacancy centre for readout and an 'amplifier' spin system that directly senses tiny local magnetic fields. Our calculations show that this hybrid structure has the potential to detect magnetic moments with a sensitivity and spatial resolution far beyond that of a sensor based on only a nitrogen-vacancy centre, and indeed this may be the physical limit for sensors of this class.

Finally, the last research chapter investigates measurements of magnetic-field strength using an ensemble of spin-active molecules. Here, we describe a quantum strategy that can beat the common standard strategy. We identify the conditions for which this is possible and find that this crucially depends on the decoherence present in the system.

Acknowledgements

First of all I would like to thank my supervisors Brendon Lovett, Simon Benjamin and Erik Gauger for their tremendous support and encouragement. In particular, I am very grateful that they built the base for my DPhil, namely sorting out the funding for it. Even more important, I am very obliged for all their countless hours that they spent on my supervision and for sharing all their expertise. The quality of the supervision was excellent and it is not possible to even think about an improvement. To put it in Simon's words: The supervision was *perfect*! And in my words: It was *unbelievable*! In summary, to have worked with you was a very special gift, for which I am very thankful.

Further, I gratefully acknowledge all co-authors of my publications: Harry Anderson, Arzhang Ardavan, Simon Benjamin, Andrew Briggs, Vasileia Filidou, Joseph Fitzsimons, Erik Gauger, Feliciano Giustino, Kevin Henbest, Steven Karlen, Kiminori Maeda, Yuichiro Matsuzaki, John Morton and Brendon Lovett. I very much enjoyed working with you and thank you for your contributions to my work. Moreover, I thank Avinash Kolli, Stephanie Simmons, Jason Smith, Brian Patton and Joachim Wabnig for fruitful discussions. I thank Simon Benjamin for working with me on the beautiful POV-ray figures (buckyball, nanodiamond). And for the tedious work of proof-reading I very thank Erik Gauger, Brendon Lovett, Simon Benjamin and Shobha Maharaj.

I also like to thank all members of the QIPIRC building, especially the QuNaT group for making our building such an enjoyable and pleasant environment to work in. Special thanks in this matter go to Erik Gauger, Volker Lang and Yimin Wu.

Moreover, I would like to thank all my friends and family for their support. In particular, I am very grateful for all my visitors that spared neither cost nor effort to travel to Oxford: Matthias Erdmann, Martin Göppel, Tobias Heinrich, Andreas, Maleen, Christopher and Patrick Holm, Margaretha, Wolfgang and Ludwig Hummel-Köllen, Stefan and Patrick Jaslowitzer, Annina Karpf, Ravindra Maharaj, Roman Pampus, Steffi Rahmig, Verena and Wolfgang Schaffry, Stefan Scholz, Johanna, Rowald, Christian and Verena Staufenbiel and Mirko Zeppmeisel. The time spent with you was invaluable and gave me the energy for my DPhil. Important in this respect, are also all the friends that I have got to know at college: Amr Abdelgany, Alexander Dilthey, Marko Jung, Sharen Lee, John Russel and Elsbeth van der Wilt. It is a privilege to have met all of you

and thank you for the nice time at college. By the way, did we ever sign up for a Guest Night?

For financial support, I am indebted to my parents, the Marie Curie Early Stage Training network QIPEST (MEST-CT-2005-020505), the EPSRC through QIP IRC (GR/S82176/01 and GR/S15808/01), the Department of Materials, Linacre College, the Royal Society, e-fellows.net and DAAD (German Academic Exchange Service). Furthermore, I would like to thank the CQT at the National University of Singapore for their hospitality.

To emphasise your importance, I thank you, Shobha, last. I would like to thank you for all your love and support. Thank you for always being there for me and sharing so many nice moments with me.

Contents

List of publications

This thesis is based on the following publications:

(i) M. Schaffry, V. Filidou, S. D. Karlen, E. M. Gauger, S. C. Benjamin, H. L. Anderson, A. Ardavan, G. A. D. Briggs, K. Maeda, K. B. Henbest, F. Giustino, J. J. L. Morton and B. W. Lovett. Entangling remote nuclear spins linked by a chromophore. *Physical Review Letters*, 104(20):200501, 2010. doi:10.1103/PhysRevLett.104.200501.

(ii) M. Schaffry, E. M. Gauger, J. J. L. Morton, J. Fitzsimons, S. C. Benjamin and B. W. Lovett. Quantum metrology with molecular ensembles. *Physical Review A*, 82(4):042114, 2010. doi:10.1103/PhysRevA.82.042114.

(iii) M. Schaffry, E. M. Gauger, J. J. L. Morton and S. C. Benjamin. Proposed spin amplification for magnetic sensors employing crystal defects. *Physical Review Letters*, 107(20):207210, 2011. doi:10.1103/PhysRevLett.107.207210.

(iv) M. Schaffry, S. C. Benjamin and Y. Matsuzaki. Quantum entanglement distribution using a magnetic field sensor. 2011. arXiv:1106.0613[quant-ph].

(v) M. Schaffry, B. W. Lovett and E. M. Gauger. Creating nuclear spin entanglement using an optical degree of freedom. *Physical Review A*, 84(3):032332, 2011. doi:10.1103/PhysRevA.84.032332.

Chapter 1

Introduction

Contents

1.1 Motivation and outline

These days nanostructures are having more and more impact on our everyday life. For example, they are used in cosmetics, in pharmaceuticals and most excitingly in information processing. Therefore it is very important to understand nanostructures more thoroughly. As these structures are by definition very small – on the atomic length scale – the physics of choice to describe them is quantum physics. With quantum physics one can define a new way of computing, called quantum computing. This way of computing will probably be much more powerful than ordinary computers are and ever will be. However, rigorous proofs for this claim are still missing. Quantum computers process quantum states for their computations, and therefore the question of how to successfully manipulate quantum states within nanostructures is of great importance. Many theoretical concepts have been developed to build a quantum computer, but for its realisation there is still a long way to go. For this reason, now, the focus should be on understanding small quantum systems. Present and near-future experiments have already to cope with many – sometimes too many – technical limitations. On the one hand, what we learn from these experiments can then be used to design experiments with larger quantum systems. On the other hand one can incorporate small quantum systems into a quantum technology with a real-world application. For example, as we see in this thesis, small quantum system can be used for very precise sensing of small magnetic fields. The research effort connected with the development of quantum technology based on small quantum systems will then promote the construction of a quantum computer.

We begin this thesis, in this chapter, with a broad introduction to various topics on which the research chapters are based. First, we introduce the basic concept of quantum information processing (QIP) by following its historical roots. We

will see in this context that the quantum phenomenon of quantum entanglement is very important and we will motivate this term in the succeeding section.

Although the theoretical concept of a quantum computer is well understood, its technical implementation is very difficult. The main reason for this is that a quantum computer is a quantum system and such a system is always coupled to its environment. The environment causes negative effects that ultimately destroy the calculations run by a quantum computer. Fortunately, quantum computers can tolerate a fair amount of information degradation by using clever techniques, called quantum error correction. To understand the causes of the errors a quantum system always needs to be described in combination with its environment. In this case the quantum system is called an open quantum system. We very briefly review important terms in this field in another section.

As mentioned before, another very useful application of entangled quantum systems is parameter estimation. Measurement devices with entangled states are fundamentally superior to conventional technologies. In Section 1.5, we introduce the relevant ideas in this field, in particular the quantum Fisher information.

We conclude the introduction with a section about the properties of two prominent quantum systems, buckminsterfullerenes and nitrogen-vacancy (NV) defects in diamond because the ideas of three research chapters can perhaps be realised with these nanostructures.

In the first research chapter, Chapter 2, we propose and examine methods for entangling two (remote) nuclear spins through their mutual coupling to a transient optically excited electron spin. From our calculations we identify the specific molecular properties that permit high entangling power gates for different protocols.

In Chapter 3, we investigate another method to create entanglement, this time

between two remote electronic spins. This method uses a very sensitive magnetic-field sensor based on a crystal defect that allows the detection of single magnetic moments. The act of sensing the local field constitutes a two-qubit projective measurement.

In Chapter 4, we present an augmented sensor consisting of an NV centre for readout and an 'amplifier' spin system that directly senses tiny local magnetic fields. Our calculations show that this hybrid structure has the potential to detect magnetic moments with a sensitivity and spatial resolution far beyond that of a simple NV centre, and indeed this may be the physical limit for sensors of this class.

Finally, in Chapter 5 we investigate measurements of the magnetic-field strength using an ensemble of spin-active molecules. Here, we describe a quantum strategy that can beat the common classical strategy. However, this depends crucially on the form of decoherence present in the system.

Each of the research chapters contains its own conclusion in which we summarise the key results and discuss possible future work.

1.2 Introduction to quantum information processing

1.2.1 Historical background and motivation

These days we store information digitally: This means that we map all types of information to ones and zeroes and store this information on a hard disk, CD, DVD, etc.. Quantum information is a generalisation of the term (digital) information and its definition is based on quantum mechanics, the most fundamental description of all physical systems at the atomic level. Devices that process

quantum information are called *quantum computers*. Historically there are two motivations for building such a device that became apparent in the beginning of the 1980s.

First, computer manufactures at that time wanted to achieve a significant reduction of the amount of energy consumed by computers. Computers dissipate energy because most of the operations, like for example the AND gate or OR gate, are irreversible. The irreversibility implies a loss of information. Landauer found that at least $k_B T \ln(2)$ (here T is the temperature of the computer and k_B is the Boltzmann constant) of energy is needed in order to delete one bit of information [107]. In the year 2000, a computer manufacturer brought the energy consumption down to about $500 k_B T \ln(2)$ for one logical operation [143], which is still far away from the theoretical minimum. In contrast, a reversible gate dissipates (almost) no energy, and for that reason, IBM researchers and others were concerned with reversible logic [21, 68]. As the dynamics in quantum mechanics are time-invariant, i.e. reversible, they started thinking about using quantum mechanics for reversible quantum computation.

Second, another motivation for developing a quantum computer goes back to Feynman, who wanted to simulate quantum mechanical solid state systems with a computer. He found that our computers are in principle not designed to solve this task, and, for this purpose, he suggested building a new computer based on quantum mechanics [65].

In the following years, Deutsch generalised the *Turing machine* [189], i.e. a model with which computers can be formally described, to a *quantum Turing machine* [55] and thereby created the theoretical concept for a quantum computer. In 1994, Shor achieved a major breakthrough in the field of quantum information processing (QIP) by proposing a quantum algorithm [174, 177], which can factor an integer n in polynomial time: $\mathcal{O}(n^2 \log(n) \log\log(n))$. The best

classical algorithm is based on the number field sieve [111, 110], whose running time is $\mathcal{O}(\exp(c[\log(n)]^{1/3}[\log\log(n)]^{2/3}))$, i.e. exponential. Thus, the quantum algorithm runs exponentially faster than the best know classical algorithm.

Besides the prospect of exponential speed-up, many authors writing about QIP motivate the construction of a quantum computer by also referring to the fact that the current computer technology will reach its limits in a few years (*Moore's law* [131]). In 1965 Moore predicted more or less correctly that the number of transistors per processor chip can be doubled about every 24 months[1] and in the same period, the processing performance of microprocessors doubles. Obviously, the miniaturisation reaches a limit, when the building blocks are so small that quantum mechanical effects dominate, and thus an inherently new technology is needed. At the moment it is not obvious that the only way to overcome the emerging difficulties is to build a quantum computer.

Obviously, to build a quantum computer is a highly desirable aim, and, unfortunately, it seems that it will not be achieved soon, as its technical implementation is still too difficult. But, research in the area of QIP is very important and significant for understanding counter-intuitive quantum mechanics more thoroughly. Hence, QIP should be considered as both a fundamental research area as well as an emerging technology. Moreover, it is crucial to pay more attention to the current technical limitations in proposals for experiments in order to realise a quantum computer sooner than it was previously thought.

[1] Originally, Moore predicted a doubling every 12 months [131]. Ten years later, at a SPIE conference (The International Society of Optical Engineering), he changed his prediction to every 24 months.

1.2.2 Qubits, gates and quantum circuits

A quantum computer is different from a conventional computer because it does not process bits, rather it processes *quantum bits*. A conventional computer can use quantum mechanical effects to process its information, but for this reason alone it does not merit the title quantum computer. It depends on the information that is processed! A quantum bit, *qubit* for short, is simply a quantum mechanical two level system [169], and a *state* of a qubit is a superposition of the corresponding two levels. Let us label these levels by $|0\rangle$ and $|1\rangle$, then a state of the qubit is described by the wave function $|\psi\rangle$

$$|\psi\rangle = a\,|0\rangle + b\,|1\rangle\,, \text{ with } |a|^2 + |b|^2 = 1 \text{ and } a, b \in \mathbb{C} \quad . \tag{1.1}$$

Examples of a qubit are a photon with its two polarisation directions (horizontally polarised, vertically polarised), two electronic states in an atom/ion (excited state, ground state), or a spin-1/2 particle (spin up, spin down). Graphically, the state of a qubit is often depicted as a point on the so-called *Bloch sphere* as Eq. (1.1) can be rewritten by using two angles θ and φ and neglecting a global phase that is physically irrelevant:

$$|\psi\rangle = \cos\left(\tfrac{\theta}{2}\right)|0\rangle + e^{i\varphi}\sin\left(\tfrac{\theta}{2}\right)|1\rangle \text{ and } \theta, \varphi \in \mathbb{R} \quad .$$

A *quantum computer* is then a device operating on a register of qubits. Well known operations on a qubit are the *rotations* $R_{\hat{n}}(\theta)$ about the real unit vectors $\hat{n} = (n_x, n_y, n_z)$ in three dimensions. The most prominent ones are the rotations about the x, y and z axis. If we identify

$$|0\rangle = \begin{pmatrix} 1 \\ 0 \end{pmatrix} \text{ and } |1\rangle = \begin{pmatrix} 0 \\ 1 \end{pmatrix} \quad ,$$

then the matrices representing these rotations in the $\{|0\rangle, |1\rangle\}$ basis are given by

$$R_{\hat{n}}(\theta) \coloneqq \exp(-i\theta\hat{n} \cdot \vec{\sigma}/2) = \cos\left(\tfrac{\theta}{2}\right) I - i \sin\left(\tfrac{\theta}{2}\right)(n_x\sigma_x + n_y\sigma_y + n_z\sigma_z) \quad ,$$

where σ_x, σ_y and σ_z are the *Pauli matrices*:

$$\sigma_x = \begin{pmatrix} 0 & 1 \\ 1 & 0 \end{pmatrix} \quad , \quad \sigma_y = \begin{pmatrix} 0 & -i \\ i & 0 \end{pmatrix} \quad , \quad \sigma_z = \begin{pmatrix} 1 & 0 \\ 0 & -1 \end{pmatrix} \quad \text{and}$$

I is the identity matrix.

These rotations play an important role in QIP because one can easily show that an arbitrary unitary transformation U on one qubit can be reduced to rotations about two nonparallel axes $\hat{n}$ and $\hat{m}$, like for example the y and the z axis, i.e. there are real numbers α, β, γ and δ, such that

$$U = e^{i\alpha} R_{\hat{n}}(\beta) R_{\hat{m}}(\gamma) R_{\hat{n}}(\delta) \quad .$$

Typically transformations on qubits are depicted by directed graphs, which are called *quantum circuits*, in analogy to ordinary circuits for classical computers. The direction of increasing time of the graph is defined from left to right, and, hence, arrows are usually neglected. Each edge represents a qubit and each node is an operation on the incoming edges (qubits) and hence called *gate*. In contrast to classical circuits, there is no branching of edges (FANOUT operation) because according to the *no-cloning-theorem* [201, 57] a quantum state cannot be copied. For an example of a quantum circuit see Fig. 1.1. Here, H stands for

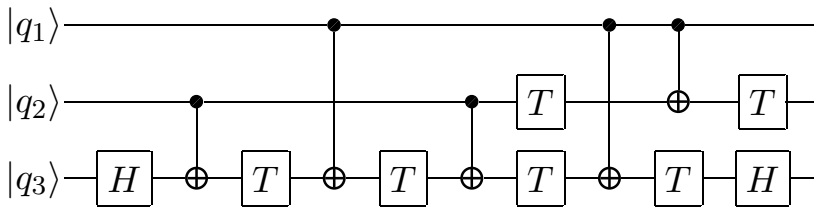

Figure 1.1: Example of a quantum circuit operating on three qubits.

the *Hadamard transformation* $H = \frac{1}{\sqrt{2}} \left(\begin{smallmatrix} 1 & 1 \\ 1 & -1 \end{smallmatrix}\right)$, and T stands for the $\frac{\pi}{8}$ gate

$$T = \begin{pmatrix} 1 & 0 \\ 0 & \exp\left(i\frac{\pi}{4}\right) \end{pmatrix} \quad . \tag{1.2}$$

The gates operating on two qubits will be explained soon.

The power of a quantum computer may arise from the fact that the space of states for $n \in \mathbb{N}$ qubits is given by the n-folded tensor product of $\mathbb{C}^2$, i.e. $(\mathbb{C}^2)^{\otimes n} \cong \mathbb{C}^{2^n}$. Hence, the matrices representing the unitary transformations $\mathcal{U}(2^n)$ on this space are exponentially large in n. It is easy to see that we cannot decompose a unitary of $\mathcal{U}(2^n)$ into unitaries of $\mathcal{U}(2)$, i.e. single qubit operations. But fortunately, we can decompose it into unitaries of $\mathcal{U}(4)$, i.e. two qubit gates, and $\mathcal{U}(2)$. An important two qubit gate in this context is the *controlled NOT gate* (CNOT gate), which operates on two qubits $(\mathbb{C}^2 \otimes \mathbb{C}^2)$

$$\mathrm{CNOT} = \begin{pmatrix} 1 & 0 & 0 & 0 \\ 0 & 1 & 0 & 0 \\ 0 & 0 & 0 & 1 \\ 0 & 0 & 1 & 0 \end{pmatrix} \quad ; \qquad \begin{aligned} |0\rangle \otimes |0\rangle &\mapsto |0\rangle \otimes |0\rangle \\ |0\rangle \otimes |1\rangle &\mapsto |0\rangle \otimes |1\rangle \\ |1\rangle \otimes |0\rangle &\mapsto |1\rangle \otimes |1\rangle \\ |1\rangle \otimes |1\rangle &\mapsto |1\rangle \otimes |1\rangle \end{aligned} \quad .$$

We see that the second qubit called the *target* qubit is flipped when the first qubit called the *control* qubit is in the state $|1\rangle$. If the control qubit is in the state $|0\rangle$, then nothing happens to the target qubit. In a quantum circuit the

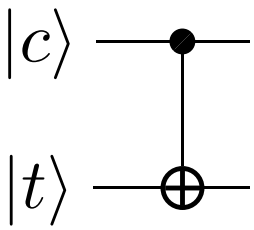

Figure 1.2: CNOT gate; top qubit = *control* qubit, bottom qubit = *target* qubit.

CNOT gate is depicted as in Fig. 1.2.

The CNOT is so famous because together with single qubit rotations, we get an *universal set* of quantum gates, i.e. a n-qubit gate can be represented by CNOT gates and rotations R_x, R_y and R_z. This was first shown by Barenco *et al.* in Ref. [14]. Up to now, several methods for this decomposition have become known [193, 137, 172, 188], and the minimum number of CNOTs needed to implement an arbitrary n-qubit operations is in the leading order $\frac{5}{6}4^n$ [25]. So, in general, one needs a number that is exponential in n of elementary gates in order to implement an arbitrary n-qubit gate.

1.2.3 Quantum algorithms

When people talk about quantum computers, they often get excited because of the enormous, predicted computing power. Some people working in this field sometimes push this too far by building the illusion that a quantum computer could solve all current problems within seconds, including **NP**-hard problems like the boolean satisfiability problem (SAT) [50], the graph colouring problem or the traveling salesman problem [96]. The truth is that up to now there are (mainly) four known classes of algorithms, in which the algorithm runs faster on a quantum computer than on a classical computer. For all other (classical) algorithms, there is currently no (quantum) speed-up known but their existence

is possible in general. Moreover, a quantum computer cannot solve problems that are impossible to solve with a classical computer. That is, both, a classical and a quantum computer can solve the same kind of problems, but a quantum computer solves certain problems faster. For the rest of this section, we consider the four classes.

The first class is given by all types of algorithms that are related to the efficient simulation of quantum mechanical systems [65, 116, 117]. With a classical computer, we need an exponential effort[2] in the size of the system, that is to say, increasing the size of the simulated system by a factor of N would require 2^N times more effort. With a quantum computer, we need only a polynomial effort in N. These algorithms will probably enable us to understand small quantum mechanical systems better.

The second group is given by all algorithms that are based on the quantum Fourier transformation. Algorithms in this class are for example the Deutsch-Jozsa-algorithm [56], Shor's algorithm for efficient factorisation and calculations of the discrete logarithm [174, 177] and the polynomial-time algorithm for the Abelian stabiliser problem [99]. A possible reason for the hype about quantum computers is given by the fact that with Shor's algorithm it would be possible to decode ciphers that are encrypted with the RSA algorithm [156]. This is possible because RSA is based on the fact that a classical computer needs a man's lifetime and longer to factorize very large numbers. At the moment RSA has many applications, and it is used for certificates (X.509 certificates), for secure communication protocols like IPSec, TLS and SSH and for email encryption (PGP and S/MIME). All these areas would be vulnerable with the existence of an adequate quantum computer.

[2] The effort is given by the amount of resources, by the duration of the calculations or by both.

The third class comprises problems that are based on Grover's algorithm for the (quantum) search of an entry in a list of length N [82]. The running time for Grover's algorithm is $\mathcal{O}(\sqrt{N})$, where a classical algorithm has to look through the whole list in the worst case, i.e. N steps are necessary in the worst case. It has been shown that this quadratic speed-up of Grover's algorithm is optimal [22] , i.e. there is no other algorithm that could solve the same problem faster.

These three classes of algorithm are very well-known in the field of QIP and often discussed in the literature. The fourth class of algorithm comprise all sorts of algorithms that can approximate the Jones polynomial of braids or links for certain roots of unity [69, 70, 8, 198]. The AJL-algorithm (Aharonov, Jones and Landau) approximates the Jones polynomial of an n-braid with m-crossings at any primitive root of unity $e^{i\frac{2\pi}{k}}$, where the running time of the algorithm is polynomial in m, n and k. Moreover, Aharonov and Arad showed that this algorithm solves a **BQP**-complete problem (for $k > 4, k \neq 6, 10$) [6, 7]. By definition, the complexity class ***BQP*** is the class of decision problems solvable by a uniform family of polynomial-size quantum circuits with a maximum error probability of $\frac{1}{4}$ [26, 46, 4]. **BQP** can be thought as the class of all feasible problems for a quantum computer. A problem L is said to be ***BQP**-complete* if the problem L is in **BQP** and every problem in **BQP** can be reduced to L with polynomial overhead. In summary, the algorithms in this fourth class of quantum algorithms provide an exponential speed-up compared to the classical analogues, and these problems make maximal use of the power of a quantum computer.

The question why these quantum algorithms are much faster than their classical analogues has not yet been answered satisfactorily [95]. In general, it is believed that entanglement is one reason for the power of a quantum computer. For this reason we will discuss this term in more detail now.

1.3 Entanglement

1.3.1 Definition and quantification

Entanglement, first recognised by Einstein, Podolsky and Rosen [61] and Schrödinger [168], is one of the most astonishing features of quantum physics. It implies a measurement correlation between two systems that is stronger than can exist in the classical world. Let $\mathcal{H}_A$ and $\mathcal{H}_B$ be the two Hilbert spaces describing the states of the systems A and B. A state of the composite system $|\psi_{AB}\rangle \in \mathcal{H}_A \otimes \mathcal{H}_B$ is said to be *separable* if it can be written as a product of states in A and B, i.e. $|\psi_{AB}\rangle = |\psi_A\rangle \otimes |\psi_B\rangle$ with $|\psi_A\rangle \in \mathcal{H}_A$ and $|\psi_B\rangle \in \mathcal{H}_B$. The two systems are said to be *entangled* when there is no such decomposition. For example, the *singlet* state $|\psi^-\rangle = \frac{1}{\sqrt{2}}\big(|01\rangle - |10\rangle\big)$ of two qubits is an entangled state. Similarly, one defines two ensembles A and B to be *separable* [196], when the density matrix[3] ρ_{AB} describing the state of the two ensembles, can be written in the form $\rho_{AB} = \sum_i p_i \rho_A^i \otimes \rho_B^i$, where ρ_A^i and ρ_B^i are density matrices of the systems A and B and p_i is a probability distribution. If two ensembles are not separable, then they are said to be *entangled*.

In order to show that a state is entangled, one uses an entanglement criterion or applies an entanglement measure to the given state rather than using the definition directly. But unfortunately, up to now, there exists no characterisation of entanglement for an arbitrary mixed state. As we will see soon, with entanglement measures we have similar problems.

According to Refs. [153, 39], one can distinguish operational entanglement criteria, like the partial transposition criterion [150, 127] or majorisation criterion [144], from nonoperational criteria. A criterion is called *operational* when one

[3] For a definition of a density matrix see Section 1.4.2 on page 31.

applies the same procedures to any density matrix and the output of the procedures tells us whether the state is entangled or not. An example for a procedure would be the calculation of the eigenvalues of the density matrix. For two qubits the partial transposition criterion is a complete characterisation of entanglement. This is in contrast to *nonoperational* criteria in which the procedure that one applies to the density matrix depends on the state that one wants to analyse. An example is an *entanglement witness* of a state ρ, which is a functional that separates the separable states from ρ. So if you have prior knowledge of a density matrix of an experiment, then one can construct an entanglement witness for this state and detect entanglement experimentally by performing some local measurements [85, 84, 38].

Another approach to detecting entanglement is to quantify it with an entanglement measure. An example is the entanglement entropy E_{entropy} [23]. For a state ρ_{AB} it is defined to be the von Neumann entropy $\operatorname{Tr}(-\rho_A \log_2 \rho_A)$ of the reduced system $\rho_A = \operatorname{Tr}_B \rho_{AB}$. This measure only makes sense for pure states, as for example $E_{\text{entropy}}(|\psi^-\rangle \langle\psi^-|) = 1 = E_{\text{entropy}}(\frac{1}{2} |01\rangle \langle 01| + \frac{1}{2} |10\rangle \langle 10|)$.

Since there are many entanglement measures, it is useful to state the properties that such a measure should have. In general, an (axiomatic) *entanglement measure* E for a bipartite system is a mapping from the set of density matrices describing the bipartite system to the positive real numbers with certain reasonable properties [153, 39]:

- $E(|\psi^-\rangle \langle\psi^-|) = 1$ (normalisation condition)
- For a separable state ρ_{AB} it holds that $E(\rho_{AB}) = 0$.
- $E(\rho_{AB})$ does not increase under local operations and classical operations.
- For a pure state $|\psi_{AB}\rangle \langle\psi_{AB}|$ the measure reduces to the entanglement

entropy:

$$E(|\psi_{AB}\rangle\langle\psi_{AB}|) = E_{\text{entropy}}(|\psi_{AB}\rangle\langle\psi_{AB}|) \quad .$$

A prominent example of an entanglement measure is the entanglement of formation E_{F} [200, 24]. For a given mixed state ρ, this measure is the minimal possible average entanglement (measured using entanglement entropy) over all pure state decompositions of ρ, i.e.

$$E_{\text{F}} = \inf\{\sum_i p_i E_{\text{entropy}}(|\psi_i\rangle\langle\psi_i|) \mid \rho = \sum_i p_i |\psi_i\rangle\langle\psi_i|\} \quad . \tag{1.3}$$

To calculate this quantity is in general very difficult, but for a two qubit system there are straightforward formulae.

To summarise the current knowledge about entanglement, one has to admit that there has been a lot of research in this field, but up to now for mixed states there are still many open questions and problems. For example, there is no unique measure for mixed states because the entanglement measures defined above are in general not linearly ordered, i.e. for two entanglement measures E_1 and E_2, there are states ρ_1 and ρ_2 with $E_1(\rho_1) < E_1(\rho_2)$ and $E_2(\rho_1) > E_2(\rho_2)$. Another important open question in this field is to decide whether the entanglement of formation is an additive measure, i.e. $E_{\text{F}}(\rho_{AB} \otimes \rho_{AB}) = E_{\text{F}}(\rho_{AB}) + E_{\text{F}}(\rho_{AB})$. These questions and many others need to be solved in order to understand the term entanglement completely. In the field of QIP a lot of effects, methods and ideas rely on entanglement. Hence, it is crucial for QIP to develop a theoretical characterisation of entanglement. To show this, we consider a publication of Zanardi *et al.* [207]. These authors consider unitary operations and want to quantify their power of entangling two systems. For this purpose, they define the *entangling power* e of a unitary operation U_{AB} with respect to the entanglement

measure E and the probability density p to be

$$e(U_{AB}) = \overline{E(U_{AB}\,|\psi_A\rangle \otimes |\psi_B\rangle)}^{\psi_A,\psi_B} \quad , \tag{1.4}$$

i.e. the average value of the entangling measure over all product states $|\psi_A\rangle\otimes|\psi_B\rangle$ that are distributed according to $p(|\psi_A\rangle \otimes |\psi_B\rangle)$. Obviously, the success of their approach, i.e. the entangling power, heavily depends on the chosen entanglement measure. In this way, the lack of a satisfactory entanglement measure affects many papers and their results in QIP.

1.3.2 Entanglement in experiments

From the experimental point of view, there are a lot of systems demonstrating entanglement. There are experiments with entangled photons [147], entangled atoms [86], entangled ions [157], an ion entangled with a photon [29], a single atom entangled with a single photon [197] and so forth. There is even evidence that in living organism like birds, entanglement is used for magnetic-field sensing [76, 40]. Creating and controlling entanglement is a delicate task and people think about different ways in order to create entangled states. So far, three general ways of creating entanglement have been identified [32]. The first one is to use the decay of a system into two parts. An example would be a spin zero particle that decays into two indistinguishable spin-1/2 particles. Because of the conservation of the spin, the bipartite system is in the singlet state $|\psi^-\rangle$. The second possibility is to use the interaction between two systems in order to build up an entangled state. This interaction can be a direct interaction, like in most experiments, or an indirect interaction mediated by a mediating system or the environment [77, 126]. The third possibility is given by the fact that a measurement can project a state onto an entangled state. An example

would be a Bell state measurement [32]. Note that for entanglement it is not necessary that the two spatial separated systems are close to each other. For instance, there is an experiment where the systems are one metre apart [129]. Here, Moehring *et al.* use a probabilistic scheme in order to entangle two distant atoms by projection. Unfortunately, the success rate is very low; they report only 30 successes per 10^9 attempts [129] and a 13-fold improvement of this rate in Ref. [124] but there are ideas that would help to increase this number [41].

1.4 Decoherence and quantum master equations

1.4.1 Decoherence and error correction

The Hilbert space of one qubit is isomorphic to $\mathbb{C}^2$ and the state space of n qubits is isomorphic to $(\mathbb{C}^2)^{\otimes n} \simeq \mathbb{C}^{2^n}$. The last identity could be another explanation (besides entanglement) for the power of quantum computers. It means that the state space of n qubits is exponentially large in the number of qubits but for processing the information one only acts on n qubits. The general state of such a register is a superposition of 2^n basis states. For quantum computation, it is necessary to maintain the coherence of this superposition. When this superposition is disturbed or even worse destroyed, one speaks of decoherence. The cause for decoherence is the unavoidable interaction of the system with the environment. In the beginning of quantum mechanics, one never spoke about decoherence because one only considered closed (isolated) quantum mechanical systems, and it was enough to struggle with the measurement problem. Only afterwards, one began to understand that it is essential to consider a quantum system together with its environment. Thus, the correct context in which to think of quantum system is as *open* quantum systems.

From a phenomenological point of view, one can distinguish roughly two types of decoherence [143]. First, the excited level in a qubit usually has a finite lifetime, i.e. an excited state relaxes to its ground state. The corresponding characteristic timescale is called the *relaxation time* or *spin-lattice time* and usually labelled T_1. The term 'spin-lattice time' originates from NMR, see [179, 1, 112, 183]. By definition a relaxation process always dissipates energy to the environment. In a solid, this is usually a lattice of atoms around the considered system. Second, the other decoherence effect, which in contrast is energy conserving, is the degradation of the phase information between the basis states of a given superposition. The characteristic time for this process is usually called *spin-spin relaxation time* or just *dephasing time* T_2. The terminology was again coined by researchers in NMR. When one considers an ensemble of spins, then the cause for this decoherence process is that every single system in the ensemble experiences a slightly different environment than the other spins.

We have seen that a quantum system, especially a quantum register, must be considered as an open quantum system. This implies imperfection of the quantum state that is used for the calculation. In addition to that, an application of a gate analogously also introduces an imperfection. In a classical computer one can detect and eliminate imperfection by introducing redundant information about the states. The redundant information can be a repetition, a checksum or the parity of the information. In more sophisticated schemes the information and redundant information is encoded with certain codes, like the binary Golay code or the Reed–Solomon code. Then from time to time one verifies whether the information is still consistent with the redundancy. If the encoding allows it and the encoded information is not corrupted too severely, then one can recover the original information with the redundancy. There are a whole range of different encoding methods and for a review see [100, 130].

However, in a quantum computer one cannot analogously apply these methods. One reason is that it is not possible to copy any quantum state. This is known as the no-cloning theorem [201, 57]. Moreover, a measurement of the qubit would destroy the superposition. Fortunately, Shor [175, 176] and Steane [181] found schemes that correct the ubiquitously occurring errors, and these schemes were developed further thereafter. Here, the basic idea is to change the basis in which the information is stored. This is usually done by defining a *logic* qubit to be a whole register of physical qubits, and the calculation is performed on the logic qubits. Obviously, there is a lot of overhead required by this method but the benefit from this is that it has been shown that when the error rate is below a certain number, typically 10^{-5} to 10^{-4}, then all the errors during a computation can be corrected and one computes the correct result [143]. To achieve gates or qubits with such a low error rate is quite demanding.

1.4.2 Quantum master equations

To consider decoherence quantitatively, one typically uses quantum master equations. Before we introduce those, we first gather some facts about quantum mechanics and closed quantum systems [170]. A state of a closed quantum system is given by a vector in a Hilbert space. It has been shown that there is an alternative description of states that uses density matrices [194]. A *density matrix* is a positive Hermitian operator of trace-class 1. There is a one-to-one correspondence between states and density matrices. The advantage of using density matrices over state vectors is that with density matrices one can also describe an ensemble of systems. This works as follows: Let us assume we have an ensemble of systems, e.g. a lot of qubits. Further, we assume that all these systems are in one of the states $|\psi_i\rangle$ $(i = 1, \ldots, n)$ and let p_i be the relative proportion of systems in state $|\psi_i\rangle$, i.e. $\sum_{i=1}^{n} p_i = 1$, then the quantum mechanical density matrix describing

the state of the system is given by $\rho = \sum_{i=1}^{n} p_i \left|\psi_i\right\rangle \left\langle\psi_i\right|$. The time-evolution of the ensemble is given by the von Neumann equation $i\hbar\dot{\rho}(t) = [H, \rho(t)]$, which is the analogue of the Schrödinger equation. To describe the dynamics of one subsystem that is part of a composite system, one traces out the complementary systems. A consequence of this procedure is that the dynamics of the subsystem is usually not unitary, although the dynamic of the whole system is unitary. This is the fundamental principle for dealing with open quantum systems and master equations. Very useful references and the standard text books for master equations which we consider now are [42, 72, 36].

Typically, one starts with the system of interest, adds a bath that represents the environment and adds a coupling between the bath and the system. Thus one considers a large system, which is described by the Hamiltonian:

$$\hat{H} = \hat{H}_S + \hat{H}_B + \hat{H}_I \quad ,$$

where $\hat{H}_S$ is the system Hamiltonian, $\hat{H}_B$ the Hamiltonian describing the bath, e.g. an electromagnetic field and $\hat{H}_I$ is the Hamiltonian that describes how the bath interacts with the system. To get the exact dynamics of the system of interest, the problem is solved for $\hat{H}$ first, and then the environment is traced out. For most systems this is not possible, and, usually, several assumptions and approximations are used to describe the system. A typical assumption is that the environment has no memory of the past. This assumption is the so-called Markov approximation. For that reason, a master equation, i.e. an equation that fully describes the time-evolution of an open quantum system that uses this approximation is called a *Markovian master equation*. It can be shown that every Markovian master equation that satisfies some further (technical) conditions can

be written as a master equation in *Lindblad form*, i.e.

$$\dot{\rho}_S(t) = -\frac{i}{\hbar}[\hat{H}_S, \rho_S(t)] + \sum_i \gamma_i \left(L_i \rho_S(t) L_i^\dagger - \frac{1}{2}(L_i^\dagger L_i \rho_S(t) + \rho_S(t) L_i^\dagger L_i) \right) \quad , \quad (1.5)$$

where L_i are the so-called Lindblad operators and ρ_S is the density matrix of the system of interest. We see that the von Neumann equation is extended by terms that describe the decoherence. Here, each Lindblad operator represents a different decoherence mechanism, or *channel*. For example, pure dephasing can be described by the Lindblad operator $L = \sigma_z$. Hence, the Lindblad master equation can often help to understand the decoherence mechanisms of a system by its illustrative form.

1.5 Parameter estimation

So far in this introduction, we have motivated the study of quantum states in nanostructures with the prospect of building a quantum computer. However, this is not the only possible application of the research described in this thesis. Another promising application that has the potential to be implemented in the near future is to use quantum systems as probes for sensitive measurements. For example, we will see in Chapter 4 that with crystal defects in diamond tiny magnetic fields can be sensed.

In this section, we analyse this in an abstract way, and our presentation is based on the references [101, 34, 149]. In general, a measurement of a continuous variable always implies an uncertainty in the results. Here, we would like to find the fundamental limits for this uncertainty. For this purpose, we consider the measurement of a continuous variable as a three-step process: First, we prepare

a quantum system in a certain known initial state ρ_0. Second, this system acts as a probe for an effect that we would like to observe and evolves to the state ρ_λ. Third, we measure the quantum system in order to learn about the effect characterised by the parameter λ that acted on the system. Obviously, the choice of the initial state and the method of measuring the final state tremendously affect the information that we learn about the parameter λ. Here, we only consider the uncertainty that originates from the uncertainty in the measurement process. We describe the measurement as a POVM (positive operator valued measure) [143], i.e. a set of Hermitian positive semidefinite operators $\{\Pi_x\}$ each associated with the measurement outcome x. The probability of measuring x when the system is in the state ρ_λ is given by the Born rule

$$p(x|\lambda) = \mathrm{Tr}[\Pi_x \rho_\lambda] \tag{1.6}$$

with $\int dx\ \Pi_x = 1$. As the measurement outcome is probabilistic, we need to repeat the experiment including the measurement over and over again and then estimate the value of the parameter λ by using the measurement outcomes $x_1, \ldots, x_N$. We call the estimator $\Lambda = \Lambda(x_1, x_2, \ldots, x_N)$. An appropriate measure for the uncertainty $\delta\lambda$ for estimating λ is given by

$$\delta\lambda := \frac{\Lambda}{\left|\frac{d\langle\Lambda\rangle}{d\lambda}\right|} - \lambda \quad , \tag{1.7}$$

where we the average is understood to be

$$\langle\Lambda\rangle := \int dx_1 \cdots dx_N\ p(x_1|\lambda) \cdots p(x_N|\lambda)\ \Lambda(x_1, \ldots, x_N) \quad . \tag{1.8}$$

Now, we derive a lower bound for the uncertainty in λ.

1.5.1 Fisher information and Cramér-Rao bound

For this purpose, we define

$$\delta\Lambda := \Lambda - \langle\Lambda\rangle \tag{1.9}$$

and, hence, it is true that

$$0 = \int dx_1 \cdots dx_N \; p(x_1|\lambda) \cdots p(x_N|\lambda) \; \delta\Lambda \quad . \tag{1.10}$$

If we take the derivative of this equation with respect to λ, we get

$$\int dx_1 \cdots dx_N \; p(x_1|\lambda) \cdots p(x_N|\lambda) \left(\sum_{n=1}^{N} \frac{1}{p(x_n|\lambda)} \frac{\partial p(x_n|\lambda)}{\partial \lambda} \right) \delta\Lambda - \frac{d\,\langle\Lambda\rangle}{d\lambda} = 0 \quad . \tag{1.11}$$

We can rewrite this as

$$\frac{d\,\langle\Lambda\rangle}{d\lambda} = \int dx_1 \cdots dx_N \; p(x_1|\lambda) \cdots p(x_N|\lambda) \left(\sum_{n=1}^{N} \frac{\partial \ln p(x_n|\lambda)}{\partial \lambda} \right) \delta\Lambda \tag{1.12}$$

$$= \left\langle \left(\sum_{n=1}^{N} \frac{\partial \ln p(x_n|\lambda)}{\partial \lambda} \right) \delta\Lambda \right\rangle = \sum_{n=1}^{N} \left\langle \frac{\partial \ln p(x_n|\lambda)}{\partial \lambda} \delta\Lambda \right\rangle \tag{1.13}$$

Now, if we apply the Cauchy-Schwarz inequality, i.e. $|\langle f, g\rangle|^2 \leq \langle f, f\rangle \, \langle g, g\rangle$ to this equation we get

$$\left| \frac{d\,\langle\Lambda\rangle}{d\lambda} \right|^2 \leq \sum_{n=1}^{N} \left\langle \left(\frac{\partial \ln p(x_n|\lambda)}{\partial \lambda} \right)^2 \right\rangle \left\langle (\delta\Lambda)^2 \right\rangle = N F(\lambda) \left\langle (\delta\Lambda)^2 \right\rangle \tag{1.14}$$

where

$$F(\lambda) := \int dx \; p(x|\lambda) \left(\frac{\partial \ln p(x|\lambda)}{\partial \lambda} \right)^2 = \int dx \; \frac{1}{p(x|\lambda)} \left(\frac{\partial p(x|\lambda)}{\partial \lambda} \right)^2 \tag{1.15}$$

is the Fisher information. We can relate $\langle(\delta\Lambda)^2\rangle$ to the mean square error $\langle(\delta\lambda)^2\rangle$ by

$$\left\langle(\delta\Lambda)^2\right\rangle = \left\langle(\Lambda - \langle\Lambda\rangle)^2\right\rangle = \left\langle\Lambda^2\right\rangle - \langle\Lambda\rangle^2 = \tag{1.16}$$

$$= \left|\frac{d\langle\Lambda\rangle}{d\lambda}\right|^2 \left(\left\langle(\lambda - \delta\lambda)^2\right\rangle - \langle\lambda - \delta\lambda\rangle^2\right) = \tag{1.17}$$

$$= \left|\frac{d\langle\Lambda\rangle}{d\lambda}\right|^2 \left(\left\langle(\delta\lambda)^2\right\rangle - \langle\delta\lambda\rangle^2\right) \tag{1.18}$$

and, eventually, find by using Eq. (1.14)

$$\left\langle(\delta\lambda)^2\right\rangle = \frac{\langle(\delta\Lambda)^2\rangle}{\left|\frac{d\langle\Lambda\rangle}{\lambda}\right|^2} + \langle\delta\lambda\rangle^2 \geq \frac{1}{NF(\lambda)} + \langle\delta\lambda\rangle^2 \geq \frac{1}{NF(\lambda)} \quad . \tag{1.19}$$

The right-hand side of this inequality is called the Cramér-Rao bound for the mean square error $\langle(\delta\lambda)^2\rangle$. If the estimator Λ is unbiased, i.e. $\langle\Lambda\rangle = \Lambda$, then there is no systematic error $\langle\delta\lambda\rangle^2$. From Fisher's theorem [67, 51] we know that for asymptotically large N, a maximum-likelihood estimator is unbiased and achieves the Cramér-Rao bound, i.e. the estimator is *efficient*.

Note, in this subsection, we determined the Cramér-Rao bound for one particular way of measuring the quantum system. If we measure the system in a different basis, then the probabilities are different, and we find another bound. We generalise this bound in the next subsection by deriving a bound that is independent of the measurement.

1.5.2 Quantum Fisher information

First, we introduce the symmetric logarithmic derivative (SLD) L_λ. It is the self-adjoint operator that satisfies the following equation

$$\frac{L_\lambda \rho_\lambda + \rho_\lambda L_\lambda}{2} = \frac{\partial \rho_\lambda}{\partial \lambda} \quad . \tag{1.20}$$

If we write the density operator in its eigenbasis decomposition

$$\rho_\lambda = \sum_n \rho_n \left|\psi_n\right\rangle \left\langle\psi_n\right| \quad , \tag{1.21}$$

then we find that

$$L_\lambda = 2 \sum_{nm} \frac{\left\langle\psi_m\right| \partial_\lambda \rho_\lambda \left|\psi_n\right\rangle}{\rho_n + \rho_m} \left|\psi_m\right\rangle \left\langle\psi_n\right| \quad , \tag{1.22}$$

where the sum only include terms for which $\rho_n + \rho_m \neq 0$. With the SLD, we can also rewrite the Fisher information (1.15)

$$F(\lambda) = \int dx \, \frac{\Re(\mathrm{Tr}[\rho_\lambda \Pi_x L_\lambda])^2}{\mathrm{Tr}[\rho_\lambda \Pi_x]} \quad , \tag{1.23}$$

as $\partial_\lambda p(x|\lambda) = \mathrm{Tr}[\partial_\lambda \rho_\lambda \Pi_x] = \Re(\mathrm{Tr}[\rho_\lambda \Pi_x L_\lambda])$.

By using the Cauchy-Schwarz inequality again, this time in the form $\left|\mathrm{Tr}[A^\dagger B]\right|^2 \leq \mathrm{Tr}[A^\dagger A]\,\mathrm{Tr}[B^\dagger B]$ applied to $A^\dagger = \sqrt{\rho_\lambda}\sqrt{\Pi_x}/\sqrt{\mathrm{Tr}[\rho_\lambda \Pi_x]}$ and $B = \sqrt{\Pi_x} L_\lambda \sqrt{\rho_\lambda}$, we estimate the Fisher information $F(\lambda)$ of any quantum measurement by

$$F(\lambda) \leq \int dx \left| \frac{\mathrm{Tr}[\rho_\lambda \Pi_x L_\lambda]}{\sqrt{\mathrm{Tr}[\rho_\lambda \Pi_x]}} \right|^2 \tag{1.24}$$

$$= \int dx \left| \mathrm{Tr}\left[\frac{\sqrt{\rho_\lambda}\sqrt{\Pi_x}}{\sqrt{\mathrm{Tr}[\rho_\lambda \Pi_x]}} \sqrt{\Pi_x} L_\lambda \sqrt{\rho_\lambda} \right] \right|^2 \tag{1.25}$$

$$\leq \int dx \ \mathrm{Tr}[\Pi_x L_\lambda \rho_\lambda L_\lambda] \tag{1.26}$$

$$= \mathrm{Tr}[L_\lambda \rho_\lambda L_\lambda] \tag{1.27}$$

$$= \mathrm{Tr}[\rho_\lambda L_\lambda^2] \tag{1.28}$$

This inequality can be rewritten as follows

$$F(\lambda) \leq H(\lambda) := \mathrm{Tr}[\rho_\lambda L_\lambda^2] = \mathrm{Tr}[\partial_\lambda \rho_\lambda L_\lambda] \quad , \tag{1.29}$$

where we defined the quantum Fisher information $H(\lambda)$. It can be shown that L_λ represents the optimal POVM to estimate the parameter λ. With Eq. (1.22), we derive the following formula for the quantum Fisher information

$$H(\lambda) = 2 \sum_{nm} \frac{|\langle \psi_m | \, \partial_\lambda \rho_\lambda \, | \psi_n \rangle|^2}{\rho_n + \rho_m} \quad . \tag{1.30}$$

We summarise the result of this subsection in one inequality

$$\left\langle (\delta\lambda)^2 \right\rangle \geq \frac{1}{N H(\lambda)} \quad , \tag{1.31}$$

where the right-hand side is known as the quantum Cramér-Rao bound. This inequality states that even for the best choice of the POVM the mean square error of λ is bounded from below by the quantum Cramér-Rao bound.

Another way of looking at the quantum Fisher information is to interpret it as a measure for the distinguishability of quantum states with respect to their

capabilities for parameter estimation. It can be shown that the proper measure on the manifold of quantum states is proportional to the quantum Fisher information, i.e. $g_{\mu\nu} = \frac{1}{4}\mathbf{H}_{\mu\nu}(\lambda)$. This means that if you slightly change the parameter of a state with a large quantum Fisher information, i.e. a state with optimal estimability, then this state is far away from the original state.

1.5.3 Examples: standard quantum limit and Heisenberg limit

We conclude this brief introduction to parameter estimation by considering two examples. First, we calculate the quantum Fisher information for the case where we are given N qubits each in the state $|+\rangle = \frac{1}{\sqrt{2}}(|0\rangle + |1\rangle)$. Suppose each of these qubits experience a phase shift λ, then each qubits evolves to

$$|\lambda\rangle = \frac{1}{\sqrt{2}}(|0\rangle + e^{i\lambda}|1\rangle) \quad . \tag{1.32}$$

For example, each qubit is probing a magnetic field B that is causing the phase shift λ. As $\rho_\lambda = |\lambda\rangle\langle\lambda|$ possesses the eigenvectors $|\lambda\rangle$ and $|\lambda_2\rangle = \frac{1}{\sqrt{2}}(|0\rangle - e^{i\lambda}|1\rangle)$ with the corresponding eigenvalues 1 and 0, the quantum Fisher information is given by

$$H(\lambda) = 2\left(\frac{\left|\frac{i}{2}\right|^2}{1+0} + \frac{0}{1+1} + \frac{\left|\frac{i}{2}\right|^2}{0+1}\right) = 2\frac{2}{4} = 1 \quad . \tag{1.33}$$

From Eq. (1.31) we infer that the statistical deviation for λ scales as $1/\sqrt{N}$. This scaling behaviour is generally know as the standard quantum limit (SQL) [152].

Now, we compare this to the situation where we entangle the N qubits: The qubits are initially in the state

$$\frac{1}{\sqrt{2}}(|00\ldots0\rangle + |11\ldots1\rangle) \quad . \tag{1.34}$$

If each qubit experience again a phase shift of λ, then the state of the N qubits is

$$|\lambda_N\rangle = \frac{1}{\sqrt{2}}(|00\ldots0\rangle + e^{iN\lambda}\,|11\ldots1\rangle) \quad . \tag{1.35}$$

Note, $\rho_{\lambda_N} = |\lambda_N\rangle\,\langle\lambda_N|$ has only four nonzero terms. For the sum in the formula for the quantum Fisher information we only need the eigenvectors $|\lambda_N\rangle$ and $|\lambda_{N,2}\rangle = \frac{1}{\sqrt{2}}(|00\ldots0\rangle - e^{iN\lambda}\,|11\ldots1\rangle)$ with eigenvalue 1 and 0. We get

$$H(\lambda_N) = 2\left(\frac{\left|\frac{Ni}{2}\right|^2}{1+0} + \frac{0}{1+1} + \frac{\left|\frac{Ni}{2}\right|^2}{0+1}\right) = 2\frac{2}{4}N^2 = N^2 \quad . \tag{1.36}$$

Now, the statistical deviation for λ scales as $1/N$, i.e. it is a factor of $\sqrt{N}$ smaller than in the first situation. This scaling behaviour is called the Heisenberg limit [78, 79].

1.6 Nanostructures

We conclude this introduction with brief reviews of two nanostructures that play an important role in the research chapters below. We begin with the nitrogen-vacancy (NV) centre in diamond.

1.6.1 Nitrogen-vacancy centres

Nitrogen-vacancy centres are colour centres in diamond. Diamond comprises sp^3-bonded carbon atoms that crystallise in a faced centre cubic (fcc) lattice. On each vertex there are two carbon atoms. As diamond is a semiconductor with a band gap of 5.5 eV, it is transparent for visible light. However, the crystal structure is

not perfect, it is interrupted by crystal defects. A special type of these defects is the nitrogen-vacancy centre, NV centres for short. The NV centre consists of a substitutional nitrogen impurity and a nearest-neighbour lattice vacancy. It is a colour centre with trigonal $C_{3\nu}$ symmetry. There a two types of NV centres, one is negatively charged and thus called NV^- centre and the other one is neutral and called NV^0 centre. Usually, an NV centre is considered to be an NV^- centre and we will follow this convention throughout this thesis. The NV centre possesses an associated electron spin, which ground state is a spin triplet $S = 1$ and an optical transition allowing the measurement of a single defect with a confocal optical microscope [83].

The level structure of an NV centre is depicted in Fig. 1.3. The ground states ^3A and the excited states ^3E of the electron are spin triplet states with sub-levels $m_s = 0, \pm 1$. External magnetic fields can lift the degeneracy of the sub-levels. Without an external field the sub-levels $m_s = \pm 1$ are degenerate, even for the excited state, because the defect has a $C_{3\nu}$ symmetry. The ground and the excited spin triplet have a strongly allowed dipole transition, which permits the optical detection of single NV centres. Moreover, the level structure has two important features. First, the $m_s = \pm 1$ (excited state) can decay nonradiatively to the $m_s = 0$ (ground) state, while the $m_s = 0$ (excited state) preserves $m_s = 0$. With this property one can polarise the spin rapidly by optical pumping [92]. Second, the fluorescence strongly depends on the electron spin, hence the spin can be read out by observing the photoluminescence intensity. By using these two properties Jelezko *et al.* demonstrate in Ref. [92] that they are able to coherently manipulate the electron spin.

The coherence properties of the electron spin are extraordinary and therefore interesting for quantum computing. At 1.9 K Harrison *et al.* report a value of $T_1 = 265$ s [87]. Even at room temperature, Gaebel *et al.* show that the

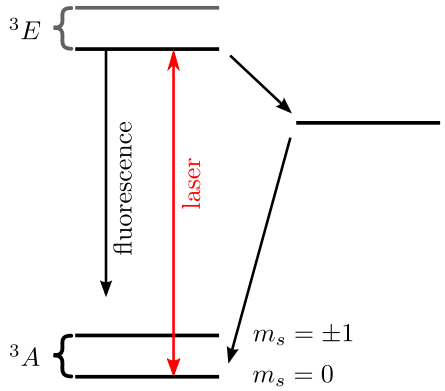

Figure 1.3: Energy level structure of the NV centre in diamond.

$T_2 = 350$ µs [71]. They achieved this high value by eliminating a major source of decoherence, namely the presence of other nitrogen atoms in the diamond [97, 62]. Hence, Gaebel *et al.* used an ultra pure (type IIa) diamond and implanted nitrogen in order to create the NV centre. With this diamond they estimate that 10^4 Rabi flops (transitions between spin states) can be accomplished before the electron spin decoheres [71]. Three years later room temperature coherence times as long as 1.8 ms [13] and 2.4 ms [139] have been measured in ultra-pure diamond.

In addition, it is shown in Ref. [28] that NV centres can be used as a single-photon source. Hence, it is in principle possible to entangle to remote NV centres by performing a path erasure experiment [16]. Barrett and Kok outline in Ref. [16] that NV centres are good candidates to implement the ideas of distributed measurement based quantum computing. Here, it is even possible to use two or three qubits at one location because Gaebel *et al.* demonstrated the coupling of two close NV centres and implemented a two qubit gate [71]. Likewise, the entanglement of the NV centre with surrounding ^{13}C atoms has been demonstrated [141, 118, 142].

However, there are some difficulties with NV centres, too. For example, the readout process is rather complex and there are several possibilities for reading

out the electron spin. At low temperature the readout of the NV centre spin can be done resonantly in one shot [202]. Although one cannot use such resonant measurements at higher temperature, a single shot measurement has been demonstrated at room temperature with the help of a nuclear spin in the vicinity of the NV centre [140]. Neumann *et al.* have transferred the information of the electron spin onto the nearby nuclear spin via a CNOT gate and have performed projective measurements by using a quantum nondemolition scheme. Alternatively, at room temperature, it is possible to utilise a nonresonant technique with many measurement cycles that reveals only little information in one cycle [185]. All these methods have in common that they suffer from the poor detection efficiency in current experiments.

Nevertheless, considering all these facts, the NV centre remains a very valuable nanostructure for QIP and is very advantageous for implementing various ideas in QIP. In this thesis, we are mainly interested in the NV centre's capability of detecting the strength of very small magnetic fields through an induced Zeeman splitting [185, 125, 12, 53, 163] see Chapter 4.

1.6.2 Buckminsterfullerenes

Other nanostructures that are very exciting and that have a big potential for QIP are buckminsterfullerenes, or buckyballs for short. Buckyballs are hollow carbon molecules that form a closed cage. The most prominent buckyball is the molecule C_{60}, which looks like a football, see Fig. 1.4. It consists of 12 pentagonal and 20 hexagonal faces. Other examples of buckyballs are the molecules C_{70}, C_{80} or C_{94}.

The existence of buckyballs was predicted by Ōsawa in Ref. [145] and in the final chapter of Ref. [205]. His prediction was not noticed by a broad audience

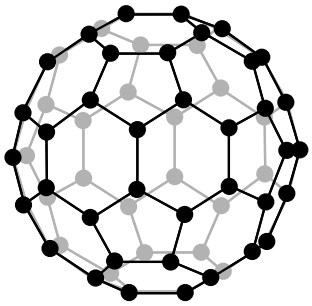

Figure 1.4: Buckyball C_{60}.

because it was written in Japanese; for an English version see [146]. Fifteen years later Kroto *et al.* discovered C_{60} without knowing about its predicted existence, this led to a great increase in the popularity of buckyballs [104]. The molecules were named buckminsterfullerene after the American architect Buckminster Fuller, who popularised the geodesic dome that resembles the buckyball. In the following years, a remarkable amount of research about buckyballs began, aided by the fact that they were simple to produce by a technique developed by Huffman and Krätschmer. This method uses an electric arc between two graphite rods in a helium atmosphere in order to vaporise carbon. Then one dissolves the condensate in organic solvents and gets crystals of C_{60} [105]. For their role in the discovery of buckyballs Kroto, Curl and Smalley were awarded the Nobel Prize in Chemistry in 1996.

At first, the applications for buckyballs where unclear. Now, there are a range of promising applications in different fields. For instance, Ref. [31] lists several applications in biology. For example, it is known that $C_{60}(OH)_n$ is an excellent antioxidant. As radicals are considered to be responsible for ageing, there are anti-ageing cremes that uses antioxidants based on C_{60}. Another exciting application is that it is demonstrated in Ref. [159] that buckyballs inhibit certain allergic responses *in vitro* and anaphylaxis *in vivo*. Although these biologic applications are promising, they are controversial because the toxicology of buckyballs is unclear and requires further investigation [49]. Recent toxicology studies

suggest that buckyballs can enter cells, can alter the functions of cells and can cross the blood-brain barrier; for some references see Ref. [199]. Therefore one cannot state yet that buckyballs are harmless particles. Obviously, their toxicity will have a major influence on their future applications.

Finally, buckyballs are also extraordinary molecules for QIP. A buckyball can be regarded as one of the smallest cages on earth within which atoms, ions and even molecules can be trapped. Such complexes are called *endohedral fullerenes* and the fact that a molecule is encased is typically symbolised with an @ in the chemical formula, as in $N@C_{60}$. In general, one distinguishes nonmetal doped fullerenes from *endohedral metallofullerenes*. Examples of the latter are $La@C_{60}$ and $La@C_{82}$ [44]. Examples of *nonmetal doped fullerenes* are $He@C_{60}$, $Ne@C_{60}$ [160] and $N@C_{60}$ [9]. $N@C_{60}$ is a good example of the possibilities arising from endohedral fullerenes. A nitrogen atom is normally highly reactive, but within the C_{60} cage it can be shielded and analysed in detail. It is an aim to harness these fullerenes in order to implement qubits. For example, Morton showed in his DPhil thesis how one can use electron spins in fullerenes as qubits [133]. A long-term aim is to build a whole quantum register that encapsulates fullerenes in a single-walled nanotube (SWNT) [17]. One calls a nanotube with encapsulated fullerenes a *peapod*. Peapods have been synthesised for example $(Gd@C_{82})_n@SWNT$ or simply $(C_{60})_n@SWNT$ [89], but of course controlling the fullerenes in a peapod separately is still challenging.

1.7 Conclusion

In this introduction, we have seen that a quantum computer is a very powerful device and discussed how it could be realised in principle. Moreover, we saw that on the atomic length scale the environment of a quantum system has a major

influence on the considered system. Hence, it is very demanding to control a nanostructure, like an NV centre or a buckyball. For that reason, building a quantum computer is still extremely difficult. In order to construct such a device, one needs to thoroughly understand single quantum systems in combination with their environment. A first step in this direction is the crucial task of creating and manipulating quantum states in nanostructures.

Chapter 2

Creating nuclear spin entanglement using an optical degree of freedom

Contents

In the pervious chapter, we have seen that molecular nanostructures are promising building blocks for future quantum technologies. However, this requires that methods of harnessing their multiple degrees of freedom (DOFs) can be identified

and implemented. Due to low decoherence rates, nuclear spins are considered ideal candidates for storing quantum information while optical excitations can give rise to fast and controllable interactions for information processing. In this research chapter, which is based on the Refs. [162] and [165], we propose methods for entangling two nuclear spins through their mutual coupling to a transient optically excited electron spin. Our presentation comprises a detailed theoretical framework, showing that these methods are in fact applicable to a wide class of molecular structures.

2.1 Introduction

Employing molecular systems as 'quantum hardware' [182, 17] offers the advantages of high reproducibility, chemically engineered system properties and the potential for self-assembly into more complex functional units. In general, nuclear spins are widely considered to be the most promising quantum bits (qubits) for a quantum memory in solid-state systems, since they have remarkably long coherence times [106]. However, they are also hard to manipulate on a fast time scale, as nuclei are usually only weakly coupled. Hence the key challenge for nuclear spin-spin entanglement is achieving fast and switchable control over the interactions between adjacent qubits.

Several previous publications have proposed the introduction of a mediator spin, whose mutual coupling to the qubit spins provides a route for a controlled entangling operation [184, 18, 20, 11, 77]. In these studies the mediator spin is usually of the same type as the qubit spins and possesses a spin of 1/2, so the system comprises either three electron or three nuclear spins. However, employing a mediator spin of the same kind as the qubit spins often does not allow for operation times that are many orders of magnitude shorter than the coherence

time of the qubits. By contrast, many molecular structures possess transient optically excited triplet states (i.e. states with spin-1 character) that could be used as mediators for nearby nuclear spins [204, 180, 59, 209, 191]. In this chapter we show how fast controlled entangling operations with a high fidelity are possible in suitable structures of this type. This constitutes an instance of a so-called hybrid approach to quantum computing [134], where the advantages of different qubit systems are combined to improve overall performance. In fact, the systems we consider here possess three distinct degrees of freedom: an optical, an electron spin and a nuclear spin one. We believe that a future quantum processor will also likely harness a similar hierarchy of different degrees of freedom, providing additional motivation to probe the interplay between different degrees of freedom beyond the immediate purpose of this work.

A hybrid approach such as the one considered here offers several further advantages besides achieving fast gating times. For example, the presence of the optical excitation in this class of system may facilitate dynamic nuclear polarisation [120, 15]. Further, recent experiments have shown that the principal decoherence mechanism for nuclear spins that are controlled through their interaction with electron spins is caused by that very same interaction [136]. However, for the entangling operations that are the subject of the present chapter, the electron spin is transient and only exists as long as the system is in its optically excited state, which should therefore be beneficial for the nuclear spin coherence time. Finally, the fact that the interaction is controllable implies that we do not rely on dynamic decoupling schemes to switch off the interactions.

This chapter is organised as follows: in Section 2.2 we introduce the most general Hamiltonian for our system and discuss several possible physical implementations. Section 2.3 analyses the Hamiltonian for certain symmetry assumptions and for the general case. The symmetry considerations lead us to simplified

effective Hamiltonians, whose dynamical properties are more easily accessible. We proceed by presenting appropriate protocols for the controlled generation of entanglement for different parameter regimes in Section 2.4. We also benchmark the performance of these protocols with respect to the predominant decoherence mechanisms. Finally, Section 2.5 contains a summary and discussion of our results. Throughout this chapter, we closely relate our general ideas to the recent experiments [162, 66] which have motivated our analysis, but we would like to point out that our results are more widely applicable and not limited to these specific systems.

2.2 Model

For our model we consider a structure comprising three integral components: two nuclear spin qubits, labeled n and n', and a mediator spin system with an optical degree of freedom. We denote the ground state of the mediator as $|0\rangle$ and the first excited state as $|e\rangle$. Further, $|0\rangle$ is assumed to be spin-silent, while $|e\rangle$ possesses an electronic spin-1 character. The spin-1 (quasi)particle is thus created upon optical excitation of the mediator system. Importantly, the two spin qubits do not directly interact with each other, yet both are coupled to the excited state of the mediator with an isotropic Heisenberg interaction as depicted schematically in Fig. 2.1. The Hamiltonian for such a three-particle system in an external magnetic field is then given by

$$H = -\omega_n S_{z,n} - \omega_{n'} S_{z,n'} + |e\rangle \left(\omega_e S_{z,e} + \omega_0\right) \langle e| \\ + |e\rangle \left(A\mathbf{S}_n \cdot \mathbf{S}_e + A'\mathbf{S}_{n'} \cdot \mathbf{S}_e + D S_{z,e}^2\right) \langle e| \quad , \quad (2.1)$$

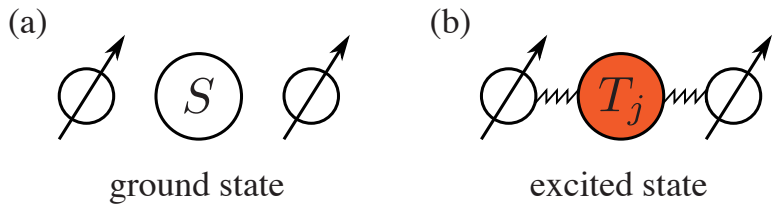

Figure 2.1: (a) There is no coupling between the mediator and the two nuclear spins in the ground (or vacuum) state $|0\rangle$. (b) The excited state of the mediator (e.g. an electron-hole pair) has spin-1 character and couples to both nuclear spins. In general, the mediator state T_j is a mixture of the triplet states T_-, T_0 and T_+.

where $\omega_{n/n'}$ denotes the Zeeman splitting of the two qubits and $\omega_e > 0$ that of the central spin-1 particle; D is the uniaxial zero-field-splitting, A and A' are the isotropic Heisenberg coupling constants and ω_0 denotes the (typically optical) excitation energy of the mediator. Here, $S_{z,n/n'/e}$ and $\mathbf{S}_{n/n'/e}$ are the usual component and total vector Pauli spin operators, respectively.

The Hamiltonian (2.1) can describe many different nanostructures, in particular, a range of optically active molecules, in which case the mediator ground (excited) state corresponds to the absence (presence) of an electron-hole pair. The transition between these two states can be induced by a short laser pulse of frequency ω_0; moreover, the excited state will decay naturally through spontaneous emission. By contrast, an NV^- centre in diamond surrounded by two ^{13}C atoms [141] is an example of a system in which the spin-1 mediator is not susceptible to decay and is ever-present. Many of the results discussed in this chapter are equally valid for this kind of system. However, the following discussion primarily focuses on the example case of the molecular system consisting of a functionalised C_{60} molecule with two functional groups as depicted in Fig. 2.2.

In what follows we will first analyse Hamiltonian (2.1) for two different cases: that of a symmetric and that of an asymmetric system. In order to understand

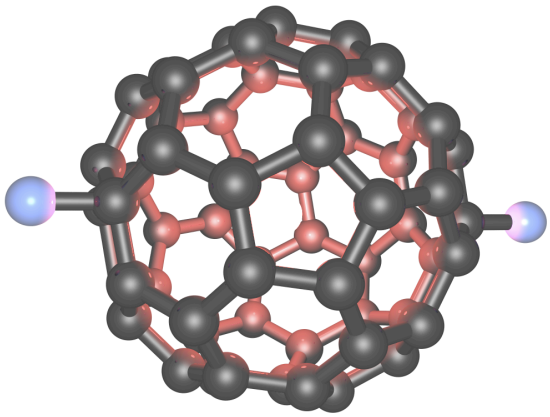

Figure 2.2: A functionalised buckyball with two satellite atoms [far left and far right (blue) spheres]. In reality the functional groups are likely much larger than a single atom, but for simplicity we depict here only the two relevant atoms with a nuclear spin-1/2, for example, ^{13}C, ^{15}N, or ^{31}P. Note that the two satellites (or, rather, functional groups) are not necessarily both the same and that the system may thus be 'asymmetric'.

the system properties and dynamics, we will determine the eigensystem using perturbation theory. We next present suitable protocols for the controlled generation of nuclear spin entanglement for both cases. We conclude this chapter with a brief summary and a discussion of our results.

2.3 Eigenspectrum and effective Hamiltonian

2.3.1 Symmetric system

By definition, the symmetric system consists of two nuclear spins with $\omega_n = \omega_{n'}$ and equal hyperfine coupling constants $A = A'$. In the presence of the electronic excitation, i.e. after the application of a suitable laser pulse, the Hamiltonian

governing the spin dynamics is given by

$$H_{\text{sym}} = \langle e| H |e\rangle = -\omega_n S_{z,n} + \omega_e S_{z,e} - \omega_n S_{z,n'} + A\left(\mathbf{S}_n \cdot \mathbf{S}_e + \mathbf{S}_{n'} \cdot \mathbf{S}_e\right) + D S_{z,e}^2 \quad , \quad (2.2)$$

where we have neglected the term ω_0, which is proportional to the identity and unimportant for the dynamics. Since the electronic Zeeman splitting ω_e is typically the largest energy scale of the system (and, in particular, much larger than ω_n), it is safe to assume that

$$|\omega_n|, |D|, A \ll \omega_e \quad . \quad (2.3)$$

Based on the above assumption, we employ degenerate perturbation theory to determine the eigenspectrum of H_{sym}. We begin by partitioning the Hamiltonian as follows

$$H_{\text{sym}} = H_{0,\text{sym}} + H'_{\text{sym}} \quad , \quad (2.4)$$

where

$$H_{0,\text{sym}} = -\omega_n S_{z,n} + \omega_e S_{z,e} - \omega_n S_{z,n'} + D S_{z,e}^2 \quad (2.5)$$

will be treated exactly, and the perturbation is given by

$$H'_{\text{sym}} = A\left(\mathbf{S}_n \cdot \mathbf{S}_e + \mathbf{S}_{n'} \cdot \mathbf{S}_e\right) \quad . \quad (2.6)$$

As $H_{0,\text{sym}}$ is diagonal in the computational basis (defined as $\{|en_1n_2\rangle \mid e = T_\pm, T_0$ and $n_{1/2} = \uparrow, \downarrow\}$) and $\langle\downarrow\uparrow| H_{0,\text{sym}} |\downarrow\uparrow\rangle = \langle\uparrow\downarrow| H_{0,\text{sym}} |\uparrow\downarrow\rangle$, degenerate perturbation theory is required. However, since $\langle T_j Y| H'_{\text{sym}} |T_l Z\rangle = 0$ for $j, l =$

$-, 0, +$ and $Y, Z = \downarrow\uparrow, \uparrow\downarrow$, the degeneracy is not removed in the first order. To find the correct zeroth-order wave functions, we need to solve the corresponding secular equations to second order [166]. Making use of assumption (2.3) we then get the following second-order eigenenergies,

$$E_{j,1} = E_{j,3} - \epsilon_j \quad , \qquad E_{j,2} = -j\omega_e + |j|\, D \quad , \tag{2.7}$$

$$E_{j,3} = E_{j,2} - \delta_j \quad , \qquad E_{j,4} = E_{j,2} + \epsilon_j \quad , \tag{2.8}$$

with the corresponding eigenvectors up to first order (see Fig. 2.3):

$$|E_{j,1}\rangle = |T_j \downarrow\downarrow\rangle \quad , \qquad |E_{j,2}\rangle = \frac{1}{\sqrt{2}}\Big(-|T_j \downarrow\uparrow\rangle + |T_j \uparrow\downarrow\rangle\Big) \quad , \tag{2.9}$$

$$|E_{j,4}\rangle = |T_j \uparrow\uparrow\rangle \quad , \qquad |E_{j,3}\rangle = \frac{1}{\sqrt{2}}\Big(|T_j \downarrow\uparrow\rangle + |T_j \uparrow\downarrow\rangle\Big) \quad , \tag{2.10}$$

and where we have defined the following quantities for compactness:

$$\epsilon_- = \omega_n - A + 2a_- \quad , \qquad \epsilon_0 = \omega_n + 2a_+ \quad , \qquad \epsilon_+ = \omega_n + A \quad , \tag{2.11}$$

$$\delta_- = -2a_- \quad , \qquad \delta_0 = -2a_0 \quad , \qquad \delta_+ = 2a_+ \quad , \tag{2.12}$$

$$a_\pm = \frac{1}{2}\frac{A^2}{\mp D + \omega_e + \omega_n} \quad , \qquad a_0 = a_+ - a_- \quad . \tag{2.13}$$

As we will see below, a_j $(j = -1, 0, 1)$ can be seen as the effective coupling constant between the two nuclear spins if the excitation is in the state $|T_j\rangle$.

Based on this spectrum, we now approximate H_{sym} in the following way to obtain an effective Hamiltonian:

$$H_{\text{sym}} \approx V^\dagger \text{diag}(E_{-1,1}, \ldots, E_{1,4}) V =: H_{\text{sym, eff}} \quad , \tag{2.14}$$

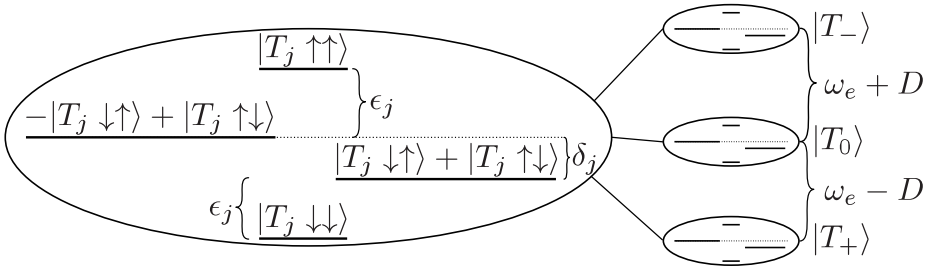

Figure 2.3: Eigenspectrum of a symmetric system up to second order of perturbation theory (eigenvectors not normalised). Our basis states obey the following relations $S_{z,e}\,|T_\pm\rangle = \mp\,|T_\pm\rangle$, $S_{z,e}\,|T_0\rangle = 0$, $S_{z,n}\,|\downarrow\rangle = |\downarrow\rangle$ and $S_{z,n}\,|\uparrow\rangle = -\,|\uparrow\rangle$.

where V is the matrix of the approximate eigenvectors (see Fig. 2.3)

$$V = (|E_{-,1}\rangle\,|E_{-,2}\rangle\cdots|E_{+,4}\rangle) \quad . \tag{2.15}$$

In the computational basis, $H_{\text{sym, eff}}$ consists of three blocks with the following structure:

$$\begin{pmatrix} \times & & & \\ & \times & \times & \\ & \times & \times & \\ & & & \times \end{pmatrix} \quad ; \quad \times \text{ denotes a nonzero entry} \quad , \tag{2.16}$$

where each block belongs to one of the three spin states T_-, T_0, or T_+. Correspondingly, we define the three subspaces $\mathcal{T}_j$ spanned by the vectors $|T_j\downarrow\downarrow\rangle$, $|T_j\downarrow\uparrow\rangle$, $|T_j\uparrow\downarrow\rangle$ and $|T_j\uparrow\uparrow\rangle$ with $j = -, 0, +$. In this chapter, the index j will denote the electronic spin state of the excitation, whereas the letter i always indexes the four nuclear spin states.

In writing Eq. (2.14) we have neglected all matrix elements between the subspace $\mathcal{T}_i$ and the subspace $\mathcal{T}_j$ $(i \neq j)$; the effect of these matrix elements is negligible because the electronic Zeeman splitting ω_e is much larger than the

nuclear Zeeman splittings. The dynamics in each of the $\mathcal{T}_j$ is therefore closed and can be described by an effective 4×4 Hamiltonian of the form given above. We shall now analyse the nuclear spin dynamics arising from each of those effective subspace Hamiltonians. A term in the Hamiltonian that is proportional to the identity has no effect on the dynamics within the subspace, so we can subtract $D + \omega_e + a_-,\ a_0$, and $D - \omega_e - a_+$ from the subspace Hamiltonians for $\mathcal{T}_-,\ \mathcal{T}_0$, and $\mathcal{T}_+$, respectively (thereby neglecting unimportant phases that are common to all states in each block). We can simplify the resulting Hamiltonians $H_{\text{sym, eff, } j}$ further by transforming to a suitably chosen rotating frame through the transformation

$$H'_{\text{sym, eff, } j} = U_j H_{\text{sym, eff, } j} U_j^\dagger + i U_j \frac{dU_j^\dagger}{dt} \quad , \tag{2.17}$$

where

$$U_j(t) = R_{z,n}\big(\phi_j t\big) \otimes R_{z,n'}\big(\phi_j t\big) \tag{2.18}$$

and

$$\phi_\pm = -\omega_n \mp A - a_\pm \quad , \tag{2.19}$$

$$\phi_0 = -\omega_n - a_- - a_+ \quad , \tag{2.20}$$

$$R_{z,i}(\phi) = \exp(-iS_{z,i}\phi) \quad . \tag{2.21}$$

In this rotating frame we obtain the following Hamiltonians

$$H'_{\text{sym, eff, } j} = k(j) 2a_j (S_{x,n}S_{x,n'} + S_{y,n}S_{y,n'}) \quad , \tag{2.22}$$

where $k(j) = 1, 1, -1$ (with $j = -, 0, +$, as it will be throughout the chapter). Each of these effective subspace Hamiltonians therefore induces the dynamics of

a direct XY-coupling of the two nuclear spins, with a time evolution corresponding to Rabi flopping between the nuclear spin states $|{\downarrow\uparrow}\rangle$ and $|{\uparrow\downarrow}\rangle$. The Rabi frequency a_j depends on the spin state j of the optical excitation. According to Eq. (2.13), we expect a_+ to be fairly similar to a_-, whereas, in comparison, a_0 will be much smaller.

We will return to the symmetric case to discuss entanglement generation in Section 2.4.1, but first complete our analysis of the Hamiltonian for nonsymmetric cases.

2.3.2 Asymmetric system

Next we consider an asymmetric system with unequal nuclear Zeeman splittings and/or unequal nuclear-electronic excitation hyperfine coupling. The excited state Hamiltonian is then given by

$$H_{\text{asym}} = \langle e| H |e\rangle = -\omega_n S_{z,n} + \omega_e S_{z,e} - \omega_{n'} S_{z,n'} + A\mathbf{S}_n \cdot \mathbf{S}_e + A'\mathbf{S}_{n'} \cdot \mathbf{S}_e + DS_{z,e}^2 \quad . \tag{2.23}$$

For the purpose of applying perturbation theory, we consider the nuclear-spin-mediator coupling as the perturbation and split the Hamiltonian as follows:

$$H_{0,\text{asym}} = -\omega_n S_{z,n} + \omega_e S_{z,e} - \omega_{n'} S_{z,n'} + DS_{z,e}^2 \quad \text{and} \tag{2.24}$$

$$H'_{\text{asym}} = A\mathbf{S}_n \cdot \mathbf{S}_e + A'\mathbf{S}_{n'} \cdot \mathbf{S}_e \quad . \tag{2.25}$$

For the asymmetric system we shall assume that the parameters A and A' and ω_n and $\omega_{n'}$ differ sufficiently to fulfil the following two inequalities

$$\frac{1}{2}\left|A' - A \pm (\omega_{n'} - \omega_n)\right| \gg \left|a_\pm\right|, \left|a'_\pm\right| \quad , \tag{2.26}$$

$$\frac{1}{2}\left|\omega_{n'} - \omega_n\right| \gg \left|a_0\right|, \left|a'_0\right| \quad , \tag{2.27}$$

where a_j and a'_j are as defined in the previous section, with the latter using $\omega_{n'}$ and A' rather than ω_n and A. Under these assumptions, nondegenerate perturbation theory can be used for calculating the eigensystem. The state corrections to first-order perturbation theory then introduce a small mixing of computational basis states with corrections of magnitude

$$\frac{1}{\sqrt{2}}\frac{A}{D \pm (\omega_e + \omega_n)} \text{ and } \frac{1}{\sqrt{2}}\frac{A'}{D \pm (\omega_e + \omega_{n'})} \quad , \tag{2.28}$$

which are negligible for $A, A' \ll \omega_e$. The eigenstates of H_{asym} thus coincide with those of $H_{0,\text{asym}}$ (which are simply the computational basis states) to a very good approximation.

Analogously to our approach in the symmetric case, we proceed by analysing individual effective Hamiltonians for the subspaces $\mathcal{T}_j$ ($j = -, 0, +$). After adding a suitable constant to each subspace, we obtain three diagonal Hamiltonians

$$H_{\text{asym, eff},j} = \phi'_j S_{z,n'} + \phi_j S_{z,n} \quad , \tag{2.29}$$

where ϕ'_j and ϕ_j are as defined in Eqs. (2.19) and (2.20) and the prime denotes that $\omega_{n'}$ and A' are used for the expression, instead of ω_n and A. All three effective Hamiltonians are local, meaning that there is no direct coupling between the two nuclear spins.

2.3.3 Crossover between a symmetric and an asymmetric system

In a certain region of parameter space neither the symmetric nor the asymmetric analyses are justified. In this section we consider this 'crossover' regime, so that in the later discussion we will be able to interpolate between those two cases.

We start with the approximated symmetric Hamiltonian $H_{\text{sym,eff}}$ and treat the asymmetry as the perturbation H'_{co}, i.e.

$$H_{\text{co}} = H_{\text{sym,eff}} + H'_{\text{co}} \quad , \tag{2.30}$$

$$H'_{\text{co}} = -\Delta_1 \omega_n S_{z,n'} + \Delta_2 A \mathbf{S}_{n'} \cdot \mathbf{S}_e \quad , \tag{2.31}$$

where Δ_1 is the fractional difference between the two nuclear Zeeman splittings, $\Delta_1 = \frac{\omega_{n'} - \omega_n}{\omega_n}$ and Δ_2 is the fractional difference between the two coupling constants, $\Delta_2 = \frac{A' - A}{A}$.

We begin with the vectors $|E_{j,i}\rangle$ and values $E_{j,i}$ $(j = -, 0, +; i = 1, \ldots, 4)$ from Section 2.3.1 as the eigenstates and eigenvalues of Hamiltonian $H_{\text{sym,eff}}$. As in the other two cases, we can still neglect those terms of H_{co} which couple different projections of the excitation spin with strength $\Delta_2 K/\sqrt{2}$ since the relevant states differ in energy by about ω_e, yielding an effective crossover Hamiltonian $H_{\text{co,eff}}$ with the eigenvectors

$$\left|\widetilde{E}_{j,1}\right\rangle = |T_j \downarrow\downarrow\rangle \quad , \quad \left|\widetilde{E}_{j,2}\right\rangle = \frac{1}{\sqrt{2}}\Big(\alpha_{j,2,1}\,|T_j \downarrow\uparrow\rangle + \alpha_{j,2,2}\,|T_j \uparrow\downarrow\rangle\Big) \quad , \tag{2.32}$$

$$\left|\widetilde{E}_{j,4}\right\rangle = |T_j \uparrow\uparrow\rangle \quad , \quad \left|\widetilde{E}_{j,3}\right\rangle = \frac{1}{\sqrt{2}}\Big(\alpha_{j,3,1}\,|T_j \downarrow\uparrow\rangle + \alpha_{j,3,2}\,|T_j \uparrow\downarrow\rangle\Big) \quad , \tag{2.33}$$

where

$$\left|\alpha_{j,2,1/2}\right|^2 = \left|\alpha_{j,3,2/1}\right|^2 = \frac{1}{2}\left(1 \pm \frac{\text{sgn}(a_j) f_j}{\sqrt{a_j^2 + f_j^2}}\right) \tag{2.34}$$

and

$$f_{\pm} = \frac{1}{2}(\Delta_2 A \pm \Delta_1 \omega_n) \quad \text{and} \quad f_0 = -\frac{1}{2}\Delta_1 \omega_n \quad . \tag{2.35}$$

The corresponding eigenvalues are

$$\widetilde{E}_{j,1/4} = E_{j,1/4} \pm k(j) f_j \tag{2.36}$$

$$\widetilde{E}_{j,2/3} = E_{j,2} + k(j)\left(a_j \mp \mathrm{sgn}(a_j)\sqrt{a_j^2 + f_j^2}\right) \quad , \tag{2.37}$$

where $k(j)$ is again 1, 1, -1 for $j = -, 0, +$, respectively.

It is easy to see that the eigenstates reduce to those of the symmetric case for a vanishing perturbation ($f_j = 0$), whereas they tend to the computational basis states for a larger perturbation as required for the asymmetric system ($|f_j| \gg |a_j|$).

2.4 Controlled generation of entanglement

The contrasting analyses presented in the previous section suggest that the dynamics of the system will vary significantly depending on its parameters. Therefore, different approaches for achieving controlled entanglement between the two nuclear spins will be required. In this section, we will show how to do this in each case; we begin with the symmetric system introduced in Section 2.3.1.

2.4.1 Symmetric system: Entangling time evolution

For the symmetric system, we shall exploit the effective XY-coupling between the spin states $|\uparrow\downarrow\rangle$ and $|\downarrow\uparrow\rangle$ for the generation of entanglement. The fact that

the magnitude of this coupling depends on the spin state of the excitation will allow us to control the interaction.

The free time evolution in any of the subspaces $\mathcal{T}_j$ takes suitable initial product states of the nuclear spins to entangled states at certain subsequent points of time. In order to quantify the performance of the desired operation, we consider the entangling power of the unitary operator that describes the time evolution of the system. Here, the entangling power is defined as the mean linear entropy produced by the unitary operator acting on a uniform distribution of all (pure) product states [see Eq. (1.4)] [207]. A maximally entangling two-qubit gate, e.g. the CNOT or the CPHASE gate, possesses an entangling power of 2/9.

For the symmetric system the entangling power of the free time evolution $U_j(t) = \exp(-iH'_{\mathrm{sym,eff},j}\, t)$ is given by the following simple expression for each of the three subspaces $\mathcal{T}_j$:

$$e_j = \frac{1}{9}\big(3 + \cos(2a_j t)\big)\sin^2(a_j t) \quad . \tag{2.38}$$

The entangling power e_j is only a function of the coupling strength a_j between the states $|T_j\downarrow\uparrow\rangle$ and $|T_j\uparrow\downarrow\rangle$, becoming maximally entangling at times that are odd-integer multiples of $t_{\max} = \pi/(2a_j)$. However, the characteristic time scale over which entanglement builds up differs significantly between the subspaces, since $a_\pm/a_0 = \omega_e/(2D)$ to leading order, and this ratio is typically much larger than one. Hence, $e_0(t) \approx 0$ for $t < \pi/(2a_\pm)$ when $|D| \ll \omega_e$ as we have assumed so far. Fig. 2.4 shows the entangling powers e_+ and e_0 for a typical ratio of $a_+/a_0 = 32$.

Based on these observations, we can formulate a protocol for the controlled generation of entanglement. Consider a system that is initially in its ground state (i.e. there is no excitation coupling to the nuclear spins). A laser pulse

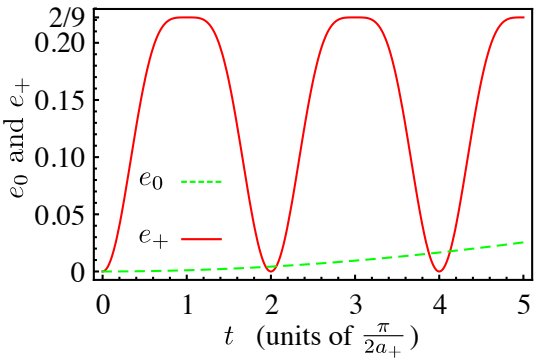

Figure 2.4: Entangling power $e_{+/0}$ of the time evolution operators $U_{+/0}(t)$. Here $a_+ = 32a_0$ (see text).

creates the excitation, which will, in general, be in a mixture of the three spin states $|T_-\rangle, |T_0\rangle$, and $|T_+\rangle$. For the present discussion, we will assume it to be in the state $|T_0\rangle$; the discussion of an mixed initial state will follow later. A short microwave pulse allows us to flip the state of the excitation selectively to either the $|T_+\rangle$ or the $|T_-\rangle$ state since the transition frequencies are split by the zero-field splitting. The entangling dynamics proceeds much faster in these outer subspaces, reaching the first entangling power maximum after a time $t = \frac{\pi}{2a_\pm}$. We can now apply another microwave pulse to flip the excitation back into the $|T_0\rangle$ state, where the further evolution is much slower and entanglement can be preserved.

There are, however, a few subtle points worth pointing out. First, similar to the case of applying the maximally entangling CNOT operation, only suitable initial states will evolve into entangled states. Second, certain particular separable input states can reach maximal entanglement in less time than $\frac{\pi}{2a_\pm}$; for example, the time evolution $U(\frac{\pi}{4a_+})$ takes $|T_+ \downarrow\uparrow\rangle$ to a maximally entangled state.

Finally, the (optical) excitation, whose natural lifetime τ is assumed to be longer than the time it takes to build up the entanglement $\frac{\pi}{2a_\pm} < \tau$, needs to be destroyed quickly enough such that no further (slower) evolution unwinding the achieved entanglement occurs in the $\mathcal{T}_0$ subspace. This can be achieved either

with a coherent optical π pulse, or alternatively by simply waiting for the system to decay back to its ground state if the following hierarchy of time scales exists in the system

$$\frac{\pi}{2a_{\pm}} < \tau \ll \frac{\pi}{2\,|a_0|} \quad . \tag{2.39}$$

However, in contrast to the de-excitation with a coherent laser pulse, it is not immediately obvious that the nuclear spin entanglement can survive the optical decay process; we will therefore now take a small diversion to analyse this decay process in detail.

2.4.1.1 Decoherence due to the optical decay process

In general, the optical decay of the mediator induces decoherence on the nuclear spins. In order to quantify this, we will make use of the quantum optical master equation (for a full derivation see e.g. Ref. [36]):

$$\frac{d}{dt}\tilde{\rho}(t) = \sum_{\omega,\omega'} e^{i(\omega'-\omega)t}\Gamma(\omega)\Big(A(\omega)\tilde{\rho}(t)A(\omega')^{\dagger} - A(\omega')^{\dagger}A(\omega)\tilde{\rho}(t)\Big) + \text{H.c.} \quad , \tag{2.40}$$

where $\tilde{\rho}$ denotes the density matrix in the interaction picture, $\Gamma(\omega')$ is the rate for a transition with frequency ω, and H.c. is the Hermitian conjugate. The sum is taken over all optical transitions of the system with transition operators $A(\omega)$ as defined by

$$A(\omega) = \sum_{E'-E=\omega} \Pi(E)\mathcal{D}\Pi(E') \quad , \tag{2.41}$$

where E and E' are eigenvalues of H that differ by ω and $\Pi(E)$ denotes the projection onto the eigenspace belonging to the eigenvalue E. $\mathcal{D}$ denotes the system's optical dipole operator. The symmetric system features twelve optical transitions $|eT_j \downarrow\downarrow\rangle \rightarrow |0 \downarrow\downarrow\rangle$, $|eT_j\rangle \frac{1}{\sqrt{2}}\big(\mp|\downarrow\uparrow\rangle + |\uparrow\downarrow\rangle\big) \rightarrow |0\rangle \frac{1}{\sqrt{2}}\big(\mp|\downarrow\uparrow\rangle + |\uparrow\downarrow\rangle\big)$, and $|eT_j \uparrow\uparrow\rangle \rightarrow |0 \uparrow\uparrow\rangle$ for $j = -, 0, +$. We make the additional assumption that the optical decay rates are all equal and can thus be characterised by a single optical lifetime τ.

Equation (2.40) can often be simplified by applying an instance of a rotating-wave approximation (RWA), based on the assumption that fast-oscillating terms average out [36], giving this more common form of the quantum optical master equation:

$$\frac{d}{dt}\tilde{\rho}(t) = \sum_{\omega} \Gamma(\omega)\Big(A(\omega)\tilde{\rho}(t)A(\omega)^\dagger - A(\omega)^\dagger A(\omega)\tilde{\rho}(t)\Big) + \text{H.c.} \quad . \tag{2.42}$$

However, the RWA is only justified when $|\omega - \omega'|^{-1}$ is small compared to the relaxation time of the system τ. Under the assumptions of Eq. (2.39) this is fulfilled except for the two transition frequencies $\omega_1 = E_{0,2} + \omega_0$ and $\omega_2 = E_{0,2} + \omega_0 - \delta_0$, which corresponds to the transitions $|eT_0\rangle \frac{1}{\sqrt{2}}\big(\mp|\downarrow\uparrow\rangle + |\uparrow\downarrow\rangle\big) \rightarrow |0\rangle \frac{1}{\sqrt{2}}\big(\mp|\downarrow\uparrow\rangle + |\uparrow\downarrow\rangle\big)$. Therefore, we can safely apply the RWA to all remaining frequencies,

obtaining:

$$\frac{d}{dt}\tilde{\rho}(t) = \sum_{\omega,\omega' \in S} e^{i(\omega'-\omega)t}\Gamma(\omega)\Big(A(\omega)\tilde{\rho}(t)A(\omega')^\dagger - A(\omega')^\dagger A(\omega)\tilde{\rho}(t)\Big) + \sum_{\omega \notin S}\Gamma(\omega)\Big(A(\omega)\tilde{\rho}(t)A(\omega)^\dagger - A(\omega)^\dagger A(\omega)\tilde{\rho}(t)\Big) + \text{H.c.} \tag{2.43}$$

$$= \sum_{\omega}\Gamma(\omega)\Big(A(\omega)\tilde{\rho}(t)A(\omega)^\dagger - A(\omega)^\dagger A(\omega)\tilde{\rho}(t)\Big) + e^{2a_0 it}\frac{1}{2\tau}\Big(2A(\omega_1)\tilde{\rho}(t)A(\omega_2)^\dagger - A(\omega_2)^\dagger A(\omega_1)\tilde{\rho}(t) - \tilde{\rho}(t)A(\omega_2)^\dagger A(\omega_1)\Big) + \text{H.c.} \tag{2.44}$$

where $S = \{\omega_1, \omega_2\}$ and, using phenomenological decay rates,

$$\Gamma(\omega) = \begin{cases} \frac{1}{2\tau} & \text{if } \omega > 0 \\ 0 & \text{if } \omega < 0 \end{cases} \quad . \tag{2.45}$$

This definition of decay rates describes the typical situation of only spontaneous emission occurring, since stimulated emission or absorption of photons is proportional to the negligible power density of thermally activated photons in the environmental modes.

Rather than solving the above master equation for the entire Hilbert space of our system, we are interested here only in the 4×4 density matrix ρ^f of the two nuclear spins after the decay has occurred:

$$\rho^f := \langle 0|\, \tilde{\rho}(t=\infty)\, |0\rangle \quad . \tag{2.46}$$

Limiting the following discussion to this nuclear spin subspace, it is easy to see that only a small number of elements of ρ^f can be populated by the decay process. These nonzero elements are $\rho^f_{a,b}$ with $a = b = \downarrow\downarrow$, $a = b = \uparrow\uparrow$, and $a, b \in \{\downarrow\uparrow, \uparrow\downarrow\}$.

The final nuclear spin state after the optical decay can be compactly written as

$$\rho^f_{a,b} = \langle eT_0 a| \tilde{\rho}_0 |eT_0 b\rangle + \frac{1}{2}\sum_{j=\pm}\left(\langle eT_j a| \tilde{\rho}_0 |eT_j b\rangle + \langle eT_j \bar{a}| \tilde{\rho}_0 \left|eT_j \bar{b}\right\rangle\right) \quad , \tag{2.47}$$

where $\tilde{\rho}_0 = \tilde{\rho}(0)$ is the full system's density matrix in the interaction picture before the decay process and the bar on top of the nuclear spin states denotes that these are flipped, i.e. $\overline{\downarrow} = \uparrow$ and $\overline{\uparrow} = \downarrow$. Hence the coherences between $|eT_\pm \downarrow\uparrow\rangle$ and $|eT_\pm \uparrow\downarrow\rangle$ do not necessarily survive, but all the coherences between $|eT_0 \downarrow\uparrow\rangle$ and $|eT_0 \uparrow\downarrow\rangle$ survive the optical decay, reflecting the fact that no RWA approximation has been made for the transitions $|eT_0\rangle\left(\pm|\downarrow\uparrow\rangle + |\uparrow\downarrow\rangle\right) \rightarrow |0\rangle\left(\pm|\downarrow\uparrow\rangle + |\uparrow\downarrow\rangle\right)$. Physically, this means that these two transitions produce indistinguishable photons due to overlapping emission spectra. In the absence of other decoherence processes, the spectra are simply given by lifetime broadened Lorentzians [122]:

$$L(\omega) = \frac{1/\tau}{(\omega-\omega_i)^2 + (1/\tau)^2} \quad \text{for } i = 1, 2 \quad . \tag{2.48}$$

The photons emitted in all other ten transitions can, in principle, be distinguished, so that we are effectively dealing with eleven distinct, incoherent decay channels. It is worth noting that there are three decay channels which populate the $|0\rangle\left(\pm|\downarrow\uparrow\rangle + |\uparrow\downarrow\rangle\right)$ states, one each for the excitation spin projections $T_{0,\pm}$, but only the decays from the $\mathcal{T}_0$ subspace preserve coherence.

In Fig. 2.5 we plot the purity $\mathrm{Tr}(\rho(t)^2) = \mathrm{Tr}(\tilde{\rho}(t)^2)$ to illustrate the decoherence induced by the optical decay for three different initial density matrices $\rho_i(0) = |\psi_i\rangle\langle\psi_i|$ with

$$\begin{aligned} |\psi_1\rangle &= |eT_+ \uparrow\downarrow\rangle \quad , \qquad |\psi_2\rangle = |eT_0 \uparrow\downarrow\rangle \quad , \quad \text{and} \\ |\psi_3\rangle &= \frac{1}{2}|eT_0\rangle\left(|\downarrow\downarrow\rangle + |\downarrow\uparrow\rangle + |\uparrow\downarrow\rangle + |\uparrow\uparrow\rangle\right) \quad . \end{aligned} \tag{2.49}$$

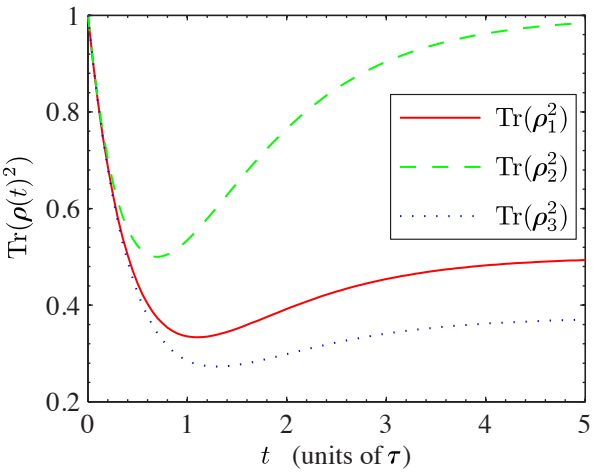

Figure 2.5: Evolution of the purity $\mathrm{Tr}(\rho(t)^2)$ of a system initialised in an excited state during the optical decay process. The three different initial states shown are defined in (2.49), and $\tau\delta_0 = 0.05 \ll \pi$.

Solving the master equation (2.43) analytically, we then obtain the following final density matrices of the nuclear spins after the decay:

$$\rho_1^f = \frac{1}{2}\big(|{\downarrow\uparrow}\rangle\langle{\downarrow\uparrow}| + |{\uparrow\downarrow}\rangle\langle{\uparrow\downarrow}|\big) \quad , \tag{2.50}$$

$$\begin{aligned}\rho_2^f = \frac{1}{2+2\delta_0^2\tau^2}\Big(&\delta_0^2\tau^2\,|{\downarrow\uparrow}\rangle\langle{\downarrow\uparrow}| + i\delta_0\tau\,|{\downarrow\uparrow}\rangle\langle{\uparrow\downarrow}| \\ &- i\delta_0\tau\,|{\uparrow\downarrow}\rangle\langle{\downarrow\uparrow}| + (2+\delta_0^2\tau^2)\,|{\uparrow\downarrow}\rangle\langle{\uparrow\downarrow}|\Big) \quad ,\end{aligned} \tag{2.51}$$

$$\rho_3^f = \frac{1}{4}\Big(\mathbf{1} + |{\downarrow\uparrow}\rangle\langle{\uparrow\downarrow}| + |{\uparrow\downarrow}\rangle\langle{\downarrow\uparrow}|\Big) \quad , \tag{2.52}$$

with the corresponding purities

$$\mathrm{Tr}(\rho_1^f)^2 = 1/2 \quad \text{and} \quad \mathrm{Tr}(\rho_3^f)^2 = 3/8 \quad , \tag{2.53}$$

$$\mathrm{Tr}(\rho_2^f)^2 = \frac{2+\delta_0^2\tau^2}{2+2\delta_0^2\tau^2} \overset{(2.39)}{\approx} 1 - \frac{\delta_0^2\tau^2}{2} \quad . \tag{2.54}$$

At first it may seem surprising that an initial state $|eT_+\rangle\,|{\uparrow\downarrow}\rangle$ can end up in a complete mixture of $|0\rangle\,|{\downarrow\uparrow}\rangle$ and $|0\rangle\,|{\uparrow\downarrow}\rangle$. This is due to the assumption (2.39), which underpins the optical master equation (2.43). This means that we

have implicitly included the fast Rabi oscillations between $|\downarrow\uparrow\rangle$ and $|\uparrow\downarrow\rangle$ in the $\mathcal{T}_+$ subspace while the system is waiting for the decay. In contrast, in the $\mathcal{T}_0$ subspace the inherent dynamics is much slower so that the final result depends on the relative magnitudes of δ_0 and τ.

Perhaps surprisingly, decay due to the spontaneous emission of a photon does not act as a source of decoherence if two conditions are met: (i) the system decays from the subspace spanned by the two states $|T_0\downarrow\uparrow\rangle$; and $|T_0\uparrow\downarrow\rangle$, and (ii) $\tau\delta_0 \ll \pi$, i.e. the energetic splitting of these two states is small compared to the inverse natural lifetime. This property can be turned into a powerful feature for suitable molecular systems, which we shall exploit in the following.

2.4.1.2 Dealing with a mixed electronic excitation

So far, we have assumed that the creation process yields a completely polarised excitation, enabling the simple protocol for the generation of entanglement described in a previous section. Motivated by recent experimental data from a promising candidate molecule [162], we now analyse the implications of having an initial mixture of the states $|T_0\rangle$ and $|T_\pm\rangle$. Experiments on a ^{13}C-labeled methano-carbon of the diethyl malonate mono-adduct (DEMF) reveal that the population of the electronic excitation in a sample oriented along the z axis are equally distributed between $|T_+\rangle$ and $|T_-\rangle$. In this case the lifetime of the excitation also depends on the state of the excitation, being much shorter for the $|T_0\rangle$ state compared to $|T_\pm\rangle$.

In the following we shall demonstrate how the generic protocol presented earlier can be adapted to accommodate for the properties of the specific system presented in Ref. [162]. After a short laser pulse for the optical excitation, the subspaces $\mathcal{T}_{0,\pm}$ were found to be populated as follows $p_- = 0.49, p_0 = 0.02$, and $p_+ = 0.49$

with associated lifetimes $\tau_- = 0.57$ ms, $\tau_0 = 0.02$ ms, and $\tau_+ = 0.57$ ms. We shall assume that the nuclear spins are initialised in the state $|{\downarrow\uparrow}\rangle$.

The basic idea of putting the system into the $|T_\pm\rangle$ states to let the free time evolution generate entanglement, followed by (mostly) switching off the interaction in the $\mathcal{T}_0$ subspace, remains unchanged. As before, switching between different electronic states is accomplished using microwave pulses that are fast on the time scale of the nuclear spin evolution. The adapted protocol proceeds in two stages following the optical excitation. First, we let the desired entanglement build up in the $\mathcal{T}_+$ subspace by waiting for the time $t = \frac{\pi}{4a_+}$. We then swap the populations of $|T_0\rangle$ and $|T_+\rangle$ and wait until the entangled populations have decayed. The difference in decay rates $1/\tau_0 \gg 1/\tau_\pm$ means that the population of $|T_-\rangle$ largely survives once the majority of $|T_0\rangle$ has decayed to the ground state. Second, population in the $\mathcal{T}_-$ subspace is maximally entangled at times that are odd-integer multiples of $\frac{\pi}{4a_-}$. We pick the first such point of time after the $|T_0\rangle$ has emptied out and apply another microwave π pulse to swap the populations of $|T_0\rangle$ and $|T_-\rangle$. Once more, $|T_0\rangle$ will quickly drain into the ground state, meaning there is now no more excited population left. Ideally, we are left with an almost fully entangled nuclear spin state.

However, the success of the above-described protocol is predicated on the coupling strength A of the nuclear spins to the excitation. In particular, for a very small coupling strength A it takes a long time to entangle the nuclear spins $t \approx \frac{\pi\omega_e}{4A^2}$, so that there may be a substantial probability of the optical decay having occurred before the nuclear spins can become properly entangled. In this case the left-hand inequality of Eq. (2.39) is violated. On the other hand, if the coupling strength A assumes very large values, then the right-hand side of the inequality (2.39) is violated. In the latter case the photons resulting from the transitions $|eT_0\rangle \frac{1}{\sqrt{2}}\big(\mp|{\downarrow\uparrow}\rangle + |{\uparrow\downarrow}\rangle\big) \rightarrow |0\rangle \frac{1}{\sqrt{2}}\big(\mp|{\downarrow\uparrow}\rangle + |{\uparrow\downarrow}\rangle\big)$ become distinguish-

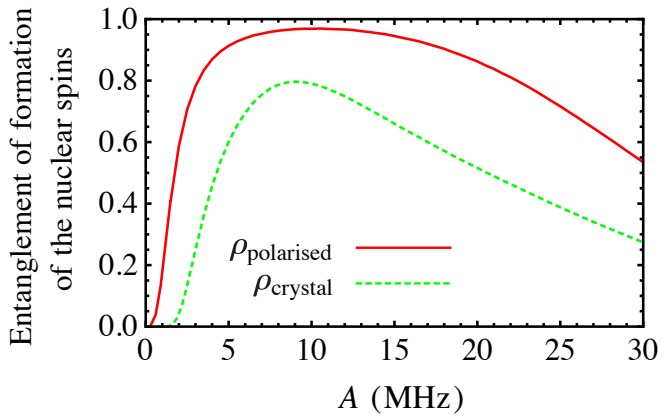

Figure 2.6: Entanglement of formation of the nuclear spins after applying our protocols as described in the text for different initial polarisations of the excitation: $\rho_{\text{polarised}} = |T_0\rangle\langle T_0|$ (solid line) and $\rho_{\text{crystal}} = 0.49\,|T_-\rangle\langle T_-| + 0.02\,|T_0\rangle\langle T_0| + 0.49\,|T_+\rangle\langle T_+|$ (dashed line). For the first case we used the simple protocol described first in this section; the switching time used is $\frac{\pi}{4a_+}$. In the second case we use the enhanced protocol described at the end of this section; switching times here are $\frac{\pi}{4a_+}$ and $\frac{3\pi}{4a_-}$. The nuclear spins for both curves are assumed to be initially in the state $|{\downarrow\uparrow}\rangle$; for the parameters we use the values found in a recent characterisation experiment [162]: $D = -296$ MHz, $\omega_e = 9.6$ GHz, $\omega_n = 3.7$ MHz, $\tau_- = 0.57$ ms, $\tau_0 = 0.02$ ms, and $\tau_+ = 0.57$ ms.

able and the decay is hence no longer coherence preserving. In Fig. 2.6 we regard the hyperfine coupling A as a tuneable parameter and plot the entanglement of formation [200] of the final state of the two nuclear spins. We consider two different initial states for the mediator spin: a completely polarised state and the mixed state reported in Ref. [162].

2.4.1.3 Robustness to imperfections in the symmetry of the system

The previously described protocol for the controlled generation of entanglement assumes a perfectly symmetric system. In the following we will analyse the degree of imperfection in the symmetry that may be tolerated. We already know that the crossover between the symmetric and the asymmetric case is not entirely abrupt. In Section 2.3.3 we have found expressions for the eigenstates and eigenvalues that can fully interpolate between the symmetric and the asymmetric case. In

this crossover case, the effective Hamiltonian still consists of three distinct blocks each corresponding to the spin state of the excitation $|T_j\rangle$ ($j = -, 0, +$), and matrix elements connecting the blocks are negligible due to the large energy difference $\omega_e \gg |\omega_n|$. This allows us to assign a separate entangling power $\widetilde{e}_j$ to the effective Hamiltonians describing each of the blocks.

We now give an easily provable lemma which will enable us to write the relevant analytic expressions of the entangling powers $\widetilde{e}_j$ for all three subspaces:

Lemma. *Let H be the time-independent Hamiltonian of two spin-1/2 particles with the following two properties:*

1. $|E_1\rangle = |{\downarrow\downarrow}\rangle\,, |E_2\rangle = -a\,|{\downarrow\uparrow}\rangle + b\,|{\uparrow\downarrow}\rangle\,, |E_3\rangle = b\,|{\downarrow\uparrow}\rangle + a\,|{\uparrow\downarrow}\rangle\,,$ *and* $|E_4\rangle = |{\uparrow\uparrow}\rangle$, *with* $|a|^2 + |b|^2 = 1$, *and* $a, b \in \mathbb{R}$ *are eigenvectors of* H.
2. *The eigenenergies of* H *satisfy* $E_1 - E_2 - E_3 + E_4 = 0$.

Then the entangling power of $U(t) = \exp(-iHt)$ *is given by*

$$e(b,\beta) = \frac{16}{9}(b^2 - b^4)\sin^2\left(\tfrac{\beta}{2}\right) - \frac{32}{9}(b^2 - b^4)^2\sin^4\left(\tfrac{\beta}{2}\right) \quad , \tag{2.55}$$

where $\beta = |E_3 - E_2|\,t$. *In addition we have* $e(a,\beta) = e(b,\beta)$.

Applying the above lemma to our effective Hamiltonians for the crossover case gives three expressions $\widetilde{e}_j = e(c_j, \beta_j)$, with

$$\beta_j = 2t\sqrt{a_j^2 + f_j^2} \quad \text{and} \quad c_j^2 = \frac{1}{2}\left(1 + \frac{f_j}{\sqrt{a_j^2 + f_j^2}}\right) \quad . \tag{2.56}$$

It is easy to see that the parameter a_j now directly competes with the strength of the perturbation f_j in the expression for the entangling power. With the

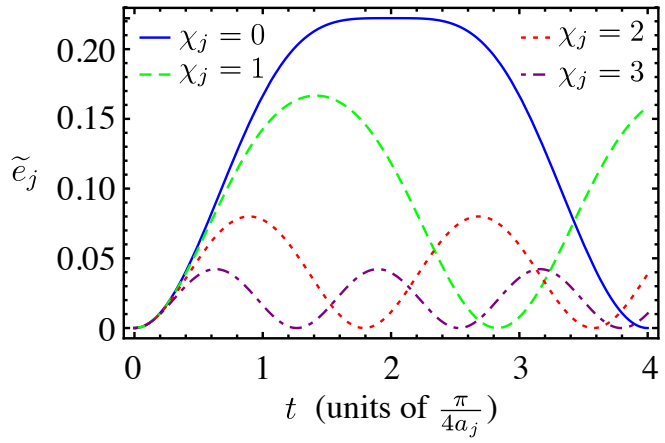

Figure 2.7: Entangling power $\widetilde{e}_j$ of the free time evolution for an asymmetric system, when the excitation is in the state $|T_j\rangle$ for different strengths of the asymmetry χ_j.

following measure for the asymmetry

$$\chi_j = \left|\frac{f_j}{a_j}\right| \tag{2.57}$$

we can write the entangling power compactly as

$$\widetilde{e}_j = \frac{\left(3 + 4\chi_j^2 + \cos\left(2a_j t\sqrt{1+\chi_j^2}\right)\right)\sin\left(a_j t\sqrt{1+\chi_j^2}\right)^2}{9\left(1+\chi_j^2\right)^2} \quad . \tag{2.58}$$

We plot $\widetilde{e}_j$ for different asymmetries χ in Fig. 2.7. Not surprisingly, the entangling power decreases with increasing asymmetry χ_j. The maximum of the entangling power, which is achieved for $\beta_j = k\pi$, where k is an odd integer, is given by

$$m_j = \frac{16}{9}(c_j^2 - c_j^4) - \frac{32}{9}(c_j^2 - c_j^4)^2 = \frac{2}{9}\frac{1+2\chi_j^2}{(1+\chi_j^2)^2} \quad ; \tag{2.59}$$

this expression is plotted in Fig. 2.8. There is no significant reduction in the achievable entanglement power as long as $\chi_j < 1/2$, but the maximum drops quickly outside this regime. We note that for equal hyperfine couplings ($\Delta_2 = 0$)

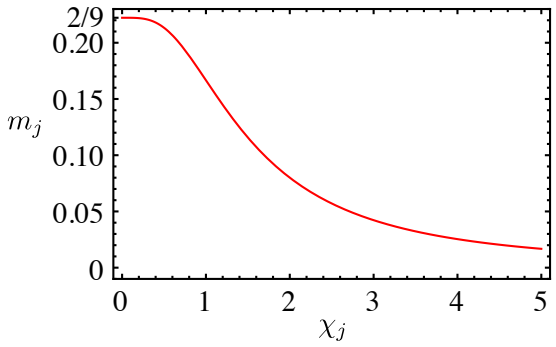

Figure 2.8: Maximally attainable entangling power m_j of the free time evolution, when the excitation is in the state $|T_j\rangle$ with respect to the strength of the asymmetry χ_j.

but unequal nuclear gyromagnetic ratios

$$\frac{\chi_0}{\chi_\pm} = \frac{a_\pm}{|a_0|} \approx \frac{\omega_e}{2\,|D|} \gg 1 \quad , \tag{2.60}$$

meaning that the $\mathcal{T}_0$ subspace's entangling power $\widetilde{e}_0$ is much more affected by the asymmetry than $\widetilde{e}_\pm$. Fortunately, the dynamics in this subspace is also the slowest, so that it can still conveniently serve as a shelf for entangled states generated in $\mathcal{T}_+$ or $\mathcal{T}_-$ until the optical excitation has been de-excited or decayed. Importantly, Eq. (2.59) implies that our scheme is robust against the small deviations from a perfectly symmetrical system which one might expect in real-world experiments. Further, intentionally introduced small differences between the frequencies ω_n and $\omega_{n'}$ (e.g. a chemical shift caused by different surrounding environments) may actually be useful for individual control and tomography of the nuclear spins, while a high-fidelity entangling operation is still possible.

So far we have discussed the behaviour of the entangling power in terms of the parameter χ_j. While the dependence of m_j on χ_j is universal across the three subspaces $\mathcal{T}_j$, we obtain qualitatively different results when considering plots that are based directly on the $\Delta_{1/2}$ asymmetry parameters. Fig. 2.9 shows the entangling power as a function of Δ_1 and Δ_2. We see that the behaviour

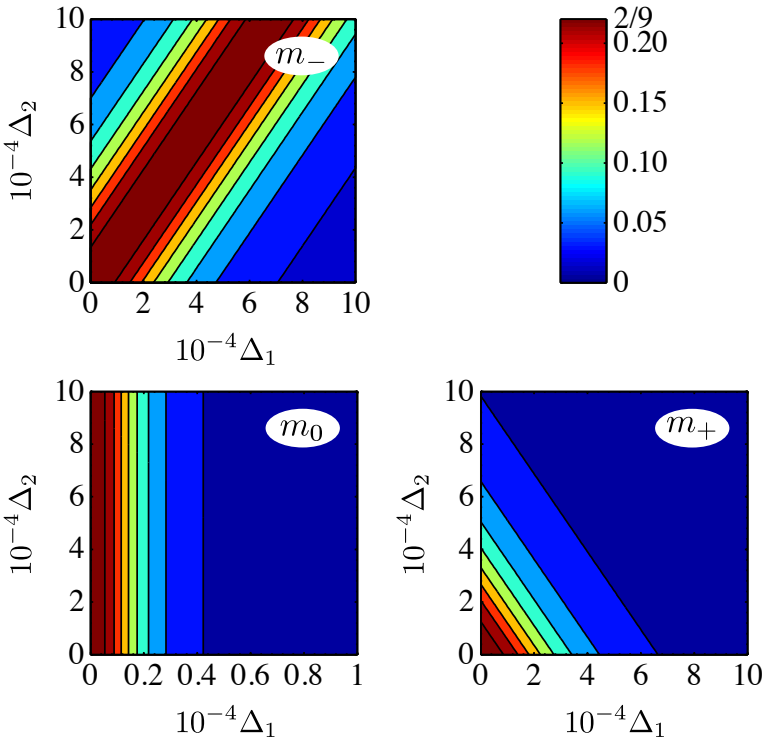

Figure 2.9: Maximal attainable entangling power m_-, m_0, and m_+ as a function of the asymmetry in the Zeeman splitting $\Delta_1 = \frac{\omega_{n'} - \omega_n}{\omega_n}$ and hyperfine coupling asymmetry $\Delta_2 = \frac{A' - A}{A}$. Other parameters are: $A = 2.5$ MHz, $\omega_n = 3.7$ MHz, $D = -296$ MHz and $\omega_e = 9.6$ GHz. The entangling power m_j only reaches its maximum limit of $2/9$ for certain values of Δ_1 and Δ_2. See the text for a more detailed discussion.

is indeed quite different in each of the three subspaces: In the $\mathcal{T}_-$ subspace we obtain a ridge along which an asymmetry between the nuclear Zeeman splittings and the hyperfine coupling constants completely cancels out, meaning that a perfect operation is possible even for a system that is quite far removed from being symmetric. In contrast, the asymmetries add up in the $\mathcal{T}_+$ subspace, so that the error tolerance is much reduced in this case. Finally, the $\mathcal{T}_0$ subspace is only sensitive to Δ_1, i.e. the difference in the nuclear Zeeman splittings without any dependence on the hyperfine constants [see Eq. (2.35)].

The entangling power vanishes completely in the limit of an entirely asymmetric system (which we take to be defined by the inequalities (2.26) and (2.27)). In this

case $\chi_j \gg 1$, and the eigenstates consequently coincide with the computational basis states, and the eigenvalues are such that the free time evolution no longer generates any entanglement (this result can be obtained by applying the above lemma). We shall analyse this situation in the following section.

2.4.2 Control methods for the asymmetric system

For an asymmetric system we cannot rely on the system's free time evolution for the generation of entanglement; this is a direct consequence of the Hamiltonian being decomposable into local Hamiltonians [see Eq. (2.29)]. Therefore, we need to apply a suitable sequence of radio-frequency and microwave control pulses to accomplish our aim of creating an entangled nuclear spin state. Hence, we proceed by analysing the dipole-allowed transitions of the asymmetric system (see Fig. 2.10).

The asymmetric system possesses six (different) nuclear spin transitions on the radio-frequency scale, one per nuclear spin for each of the three spin states of the excitation. Referring to Section 2.3.2 we obtain these from the second-order eigenenergies:

$$\omega_{\mathrm{rf},j} = \left|-jA - \omega_n - a_-(\delta_{j,-} + \delta_{j,0}) - a_+(\delta_{j,0} + \delta_{j,+})\right| \quad , \tag{2.61}$$

$$\omega'_{\mathrm{rf},j} = \left|-jA' - \omega_{n'} - a'_-(\delta_{j,-} + \delta_{j,0}) - a'_+(\delta_{j,0} + \delta_{j,+})\right| \quad , \tag{2.62}$$

where $\delta_{k,l}$ is the Kronecker delta, and as before, j indexes the spin state of the excitation $|T_j\rangle$. Further, $\omega_{\mathrm{rf},j}$ denotes the transition frequency of the first nuclear spin, and $\omega'_{\mathrm{rf},j}$ the transition frequency of the second nuclear spin. In general, all six of these frequencies may be distinct.

Conversely, the spin state of the electronic excitation can be flipped conditional

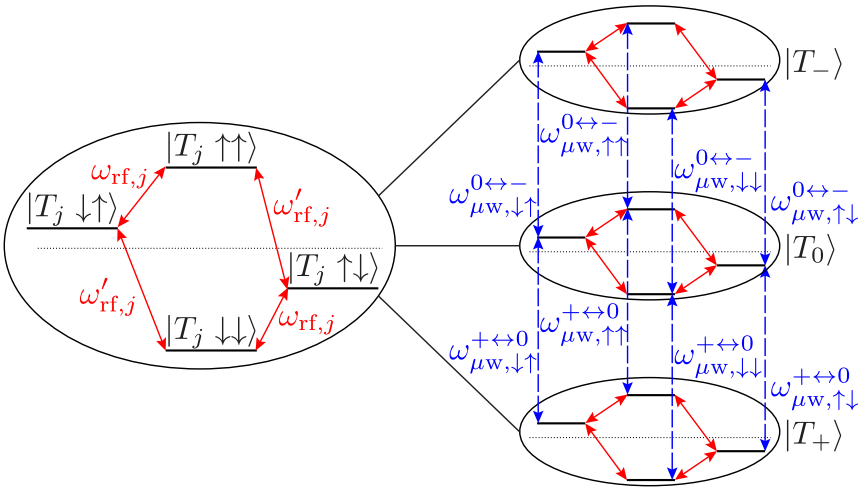

Figure 2.10: Microwave (dashed line) and radio-frequency transitions (solid line) of the asymmetric system. The computational basis states are eigenstates of the system Hamiltonian (assuming that Eqs. (2.26) and (2.27) are fulfilled).

on the nuclear spin state using a suitable microwave pulse. With four nuclear spin states and two excitation spin transitions, this gives a total of eight microwave frequencies taking the excitation from $|T_j\rangle$ to $|T_{j'}\rangle$ with $(j, j') = (+, 0)$ or $(j, j') = (0, -)$ or *vice versa*. These are:

$$\omega^{j\leftrightarrow j'}_{\mu\mathrm{w},\downarrow\downarrow/\uparrow\uparrow} = \omega_e + (-1)^j D \pm \frac{1}{2}(A + A') \quad , \tag{2.63}$$

$$\omega^{j\leftrightarrow j'}_{\mu\mathrm{w},\downarrow\uparrow/\uparrow\downarrow} = \omega_e + (-1)^j D \pm \frac{1}{2}(A - A') \quad . \tag{2.64}$$

Here we have neglected second-order perturbation theory shifts proportional to a_j and a'_j, as these are typically very small when compared to A and D.

Several possibilities exist for exploiting this rich transition spectrum in order to realize an entangling operation. In the following we shall discuss three methods in more detail: a single microwave 2π pulse, a pulse sequence of radio and microwave pulses, and, finally, an adiabatic following method.

2.4.2.1 CPHASE gate through a selective 2π pulse

Simply applying a selective 2π pulse with the frequency of any of the microwave transitions given in Eqs. (2.63) and (2.64) naturally implements a CPHASE gate by imparting a phase of $e^{i\pi} = -1$ to only one of the four nuclear spin states [143].

If the lifetime of the transition were infinite (and in the absence of other spin dephasing mechanisms), the 2π pulse could be made perfectly selective, achieved by a pulse that is long in the time domain and, accordingly, spectrally narrow in the frequency domain [27]. However, in practice, the optical lifetime will be finite and this may limit the selectivity and thus the amount of entanglement that can be achieved. The challenge is to find the right balance between a fast pulse that is only partially selective and a slow pulse during which the system suffers from the decoherence induced by the decay. We proceed by analysing the trade-off that arises from these constraints in the following.

Suppose we are given an initial state that is an equal superposition of the computational basis states and a fully polarised state of the excitation,

$$|\psi_{\text{initial}}\rangle = \frac{1}{2}\,|T_0\rangle\,(|{\downarrow\downarrow}\rangle + |{\downarrow\uparrow}\rangle + |{\uparrow\downarrow}\rangle + |{\uparrow\uparrow}\rangle) \quad , \tag{2.65}$$

and then apply a 2π microwave pulse with power Ω_0 and with a frequency ω_D corresponding to the energy difference between the levels $|T_+\uparrow\uparrow\rangle$ and $|T_0\uparrow\uparrow\rangle$. To describe the dynamics of the excited system we use either the effective asymmetric or the more general effective crossover Hamiltonian, whichever is more appropriate for the precise combination of system parameters in question. In particular, $H_{\text{asym,eff},j}$ is adequate whenever the eigenvectors closely coincide with the computational basis states, whereas $H_{\text{co,eff},j}$ is used otherwise. We apply the

following criterion for discriminating between the two cases:

$$H_{\mathrm{eff},j} = \begin{cases} H_{\mathrm{asym,eff},j} & |\alpha_{j,2,1}|^2 \leq 0.001 \text{ or } |\alpha_{j,2,1}|^2 \geq 0.999 \quad , \\ H_{\mathrm{co,eff},j} & 0.001 < |\alpha_{j,2,1}|^2 < 0.999 \quad , \end{cases} \tag{2.66}$$

with $\alpha_{j,2,1}$ as defined in Eq. (2.34). In addition to the effective system Hamiltonian H_{eff}, we also need to model the microwave pulse (in the usual RWA), so that the total Hamiltonian during the pulse is given by

$$\begin{aligned} H_{\mu\mathrm{w}} = |0\rangle \left(-\omega_n S_{z,n} - \omega_{n'} S_{z,n'}\right) \langle 0| + |e\rangle H_{\mathrm{eff}} \langle e| \\ + |e\rangle \left(\Omega_0 S_{x,e} - \omega_D S_{z,e}\right) \langle e| \quad . \end{aligned} \tag{2.67}$$

As this Hamiltonian is time independent, we can use a quantum optical master equation like the one defined in Eq. (2.43) to model the decay of the excitation in the interaction picture. The transition operators $A(\omega)$ are as defined by Eq. (2.41), with appropriate projectors onto the eigenspaces of $H_{\mu\mathrm{w}}$. In our calculations we perform the RWA in the master equation (remember that this RWA is different and independent from the RWA for the driving) whenever the difference of two frequencies differs by more than $30\tau^{-1}$, where τ denotes the lifetime of the excitation.

While optical decay during the application of the pulse may preserve some coherence between the nuclear spin states for specific parameter combinations, this is no longer the case once the pulse has finished: the decay to the ground state for an asymmetric system in the absence of microwave driving invariably destroys the nuclear coherences. Therefore, we must use a different approach for taking the system back to its ground state. The first possibility is de-excitation using a resonant optical π pulse. Another option would be to significantly 'speed up' the decay process, e.g. by exciting the system into a different metastable excited

state which is known to quickly decay to the ground state. Provided the lifetime of this metastable state is short enough, the wave function of the emitted photon does not carry information about the nuclear spin state, so that the nuclear spin coherence will be preserved. We shall assume that such a coherence-preserving de-excitation can be accomplished.

As mentioned above, the system is susceptible to potentially harmful decay events during the application of the 2π pulse, such that the final nuclear spin state ρ_{nuc} is a mixture of a population that has spontaneously decayed and the remaining population to which the control sequence has been fully applied. Since we are now dealing with mixed states ρ_{nuc}, the entangling power is no longer a suitable measure for the quality of our operation, and as before we employ the entanglement of formation [200] as an alternative benchmark.

Assuming a simple top-hat pulse profile in the time domain, the pulse duration for a 2π pulse is $t = \frac{2\pi}{\sqrt{2}\Omega_0}$, where Ω_0 is the applied microwave power. For optimal performance the right balance must be found between pulse selectivity and duration for each combination of system parameters and lifetime τ. We thus maximise the achievable entanglement of formation by varying Ω_0 to obtain

$$E_F^* = \max_{\Omega_0} E_F(\rho_{\mathrm{nuc}}) \quad . \tag{2.68}$$

As an example we choose $\tau = 10$ µs to plot the quantity E_F^* in Fig. 2.11 as a function of A and A'. Larger hyperfine coupling constants allow a faster selective pulse, and the optimised entanglement of formation of ρ_{nuc} hence increases with A and A'. Remarkably, even for a lifetime as short as 10 µs, a high entanglement of formation can be obtained with only moderate hyperfine coupling strengths.

Finally, we note that the currently presented protocol also works for the symmetric system, where the entanglement operation then only takes a time $t =$

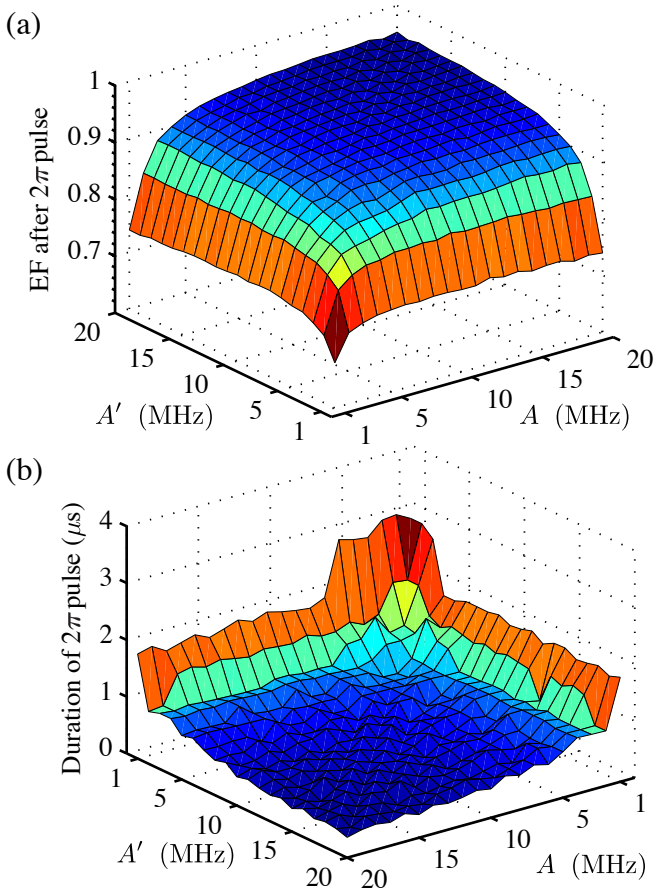

Figure 2.11: (a) Maximised entanglement of formation of he nuclear spins after the 2π pulse with respect to the two hyperfine coupling strengths A and A'. (b) Optimal duration $t^* = \frac{2\pi}{\sqrt{2}\Omega_0^*}$ of the microwave 2π pulse with respect to the two hyperfine coupling strengths A and A'. We use the illustrative lifetime $\tau = 10\,\mu\text{s}$ while the other parameters used in this plot are motivated by Ref. [66]: $D = -320$ MHz, $\omega_e = 9.7$ GHz, $\omega_n = 5.97$ MHz, $\omega_{n'} = 14.74$ MHz.

$\frac{\pi}{2a_\pm} \approx \frac{\pi\omega_e}{A^2}$, which is much faster than our protocol discussed in Section 2.4.1. For a short optical lifetime this approach may thus be advantageous, assuming that a spectrally narrow highly selective 2π pulse can be implemented.

2.4.2.2 Combined microwave and radio-frequency pulse sequence

In the previous section we have discussed a simple implementation of the CPHASE gate that is maximally entangling for suitable system parameters. However, other methods for creating maximally entangled states also exist, and these may be

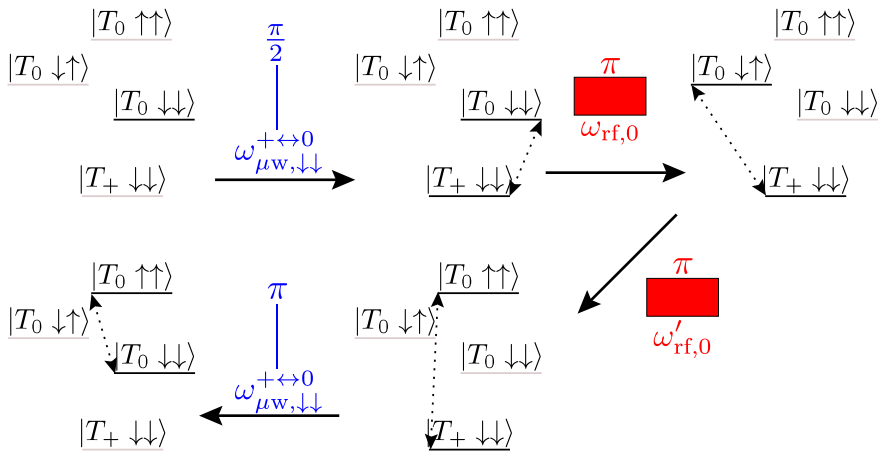

Figure 2.12: Pulse sequence for the creation of the Bell state $\frac{1}{\sqrt{2}}\big(|T_0\downarrow\downarrow\rangle + |T_0\uparrow\uparrow\rangle\big)$. Black energy levels are populated and gray levels are empty. Dotted arrows denote a coherence between the adjacent energy levels. Only relevant spin levels are shown.

more advantageous if a particular final state is required. Here we shall briefly discuss an alternative control method that employs a sequence of microwave and radio frequency pulses instead of a single microwave pulse. Let us assume that we have the initial spin state $|T_0\downarrow\downarrow\rangle$ and would like to create the entangled Bell state $\frac{1}{\sqrt{2}}\big(|T_0\downarrow\downarrow\rangle + |T_0\uparrow\uparrow\rangle\big)$. It is impossible to perform this operation with only radio-frequency pulses. However, we can achieve our aim by 'shelving' parts of the population in one of the other electronic spin states. An example of how this approach works in detail is depicted in Fig. 2.12.

Of course, the microwave and radio-frequency pulses also need to be sufficiently selective for this approach, which imposes a minimal overall pulse sequence duration. Once more, we refrain from discussing sophisticated pulse shaping techniques [27], instead considering Rabi's instructive formula for the transition probability of a driven two-level system,

$$\mathcal{P}_{1\to 2}(t) = \frac{\Omega^2}{\Omega^2+\Delta^2}\sin^2(\sqrt{\Omega^2+\Delta^2}t) \quad , \tag{2.69}$$

where Ω denotes the strength of the pulse, and Δ the detuning. We apply this to

the closest neighbouring transitions of the (resonantly driven) target transition and demand that $\Omega^2/(\Omega^2 + \Delta^2) \ll 1$ for all neighbouring transitions, allowing a rough estimation of the duration required for each pulse in the sequence.

We take the example of a recent characterisation experiment on an asymmetric system (phosphine oxide fullerene; DMFPH) [66], where the two nuclear spins of interest are provided by a hydrogen and a phosphorus atom in the functional group attached to the fullerene. The hyperfine coupling and the zero-field splitting were measured as

$$A \approx 6 \text{ MHz}, \quad A' \approx 11 \text{ MHz} \quad \text{and} \quad D \approx -320 \text{ MHz} \tag{2.70}$$

at an external magnetic field of $B = 0.346$ T. Setting an upper bound of 0.01 for the unwanted transition probabilities, the four required pulses can all be applied in less than a 1 µs for typical nuclear gyromagnetic ratios. The duration of the pulse sequence is thus short compared to the expected optical lifetimes in candidate molecules, so that a high-fidelity entangling operation using this protocol should be feasible. However, we refrain from performing a more detailed analysis as in the previous section, since the results are similar and little additional insight is gained.

2.4.2.3 Implementation of a CPHASE operation with adiabatic following

The last method discussed in this chapter for creating entanglement in our system relies on the adiabatic following of system eigenstates, similar to the protocol described in Refs. [77, 75]. Here, it is implemented by slowly modulating the intensity of a microwave pulse that is close to resonance with one or several of the microwave transitions of the excitation spin. Prior to the application of the pulse, the (asymmetric) system is prepared to be in a superposition of

computational basis states as follows:

$$|\psi_{\text{initial}}\rangle = |T_0\rangle \left(a_1 |{\downarrow\downarrow}\rangle + a_2 |{\downarrow\uparrow}\rangle + a_3 |{\uparrow\downarrow}\rangle + a_4 |{\uparrow\uparrow}\rangle\right) \quad , \tag{2.71}$$

with normalisation $\sum_{i=1}^{4} |a_i|^2 = 1$. Starting from this state, the microwave power is then varied such that adiabatic following of instantaneous eigenstates occurs. Once the power is decreased again, all populations return to the computational basis. During the pulse, the eigenstates are energetically shifted and thus pick up a dynamic phase. However, the precise shifts of the states differ due to the the hyperfine coupling, so that, in general, each of the four states acquires a different dynamic phase. This gives rise to an overall combination that can be nontrivial and entangling [75].

Consider applying a microwave field with frequency ω_D whose power envelope is changed gradually following a Gaussian function $\Omega(t) = \Omega_0 \exp[-(t/\sigma)^2]$. We apply this Gaussian microwave pulse from an initial time $t = -3\sigma$ to $t = 3\sigma$ and choose the frequency ω_D in such a way that the pulse is off-resonant with all microwave transitions in the system. The diagonal form of the system Hamiltonian $H_{\text{asym,eff}}$ permits a description of the dynamics of each state in the superposition of Eq. (2.71) with a Hamiltonian connecting all three excitation states of the form

$$\mathcal{H}_i(t) = \langle i| \mathcal{H} |i\rangle = \begin{pmatrix} \Delta_{i,1} & \frac{\Omega(t)}{\sqrt{2}} & 0 \\ \frac{\Omega(t)}{\sqrt{2}} & 0 & \frac{\Omega(t)}{\sqrt{2}} \\ 0 & \frac{\Omega(t)}{\sqrt{2}} & \Delta_{i,2} \end{pmatrix} \tag{2.72}$$

written in the basis $\{|T_- i\rangle, |T_0 i\rangle, |T_+ i\rangle\}$ for $i = \{{\downarrow\downarrow}, {\downarrow\uparrow}, {\uparrow\downarrow}, {\uparrow\uparrow}\}$ with detunings $\Delta_{i,1} = \omega_{\mu\text{w},i}^{0\leftrightarrow -} - \omega_D$ and $\Delta_{i,2} = \omega_{\mu\text{w},i}^{+\leftrightarrow 0} - \omega_D$. Note that the usual RWA has been

performed. Choosing ω_D such that, for each i,

$$\frac{\Omega(t)}{\sqrt{2}} \ll \Delta_{2,i} \tag{2.73}$$

then enables us to write an approximate Hamiltonian for each of the nuclear spin states (valid to first order in perturbation theory) as

$$\mathcal{H}_{i,\mathrm{app}}(t) = \begin{pmatrix} \Delta_{i,1} & \frac{\Omega(t)}{\sqrt{2}} & 0 \\ \frac{\Omega(t)}{\sqrt{2}} & 0 & 0 \\ 0 & 0 & \Delta_{i,2} \end{pmatrix} \quad . \tag{2.74}$$

To achieve adiabatic following, the eigenenergies need to be varied slowly to suppress Landau Zener transitions between different eigenstates. Following Ref. [77, 74], this can be accomplished under the following conditions:

$$\frac{\Omega_0}{\Delta_{1,i}^2} \ll \sigma \quad \text{for } i = \{\downarrow\downarrow, \downarrow\uparrow, \uparrow\downarrow, \uparrow\uparrow\} \quad . \tag{2.75}$$

As we have mentioned above, the net effect achieved by the adiabatic pulse is the acquisition of a phase θ_i for each of the nuclear spin states. The 'right' combination of control parameters σ, Ω_0, and $\Delta_{1,i}$ gives rise to an operation that is locally equivalent to a CPHASE gate if the following condition is met [77]:

$$\pi = \theta_1 - \theta_2 - \theta_3 + \theta_4 \quad . \tag{2.76}$$

In terms of the evolution of the nuclear spins, the state $|\psi_{\mathrm{initial}}\rangle$ has then evolved to

$$|T_0\rangle \left(a_1 e^{i\theta_1} |\downarrow\downarrow\rangle + a_2 e^{i\theta_2} |\downarrow\uparrow\rangle + a_3 e^{i\theta_3} |\uparrow\downarrow\rangle + a_4 e^{i\theta_4} |\uparrow\uparrow\rangle\right) \quad , \tag{2.77}$$

corresponding to a local phase on each nuclear spin in addition to the application

of a CPHASE gate.

We shall now address the question of how the optimal combination of control parameters may be found. The dynamical phase that is acquired by a state during the pulse is directly determined by the eigenenergy of the state $|T_0 i\rangle$, yielding

$$\theta_i = -\int_{-3\sigma}^{3\sigma} \frac{1}{2}\left(\Delta_{i,1} - \sqrt{\Delta_{i,1}^2 + 2\Omega(t)^2}\right) dt \tag{2.78}$$

$$= \frac{\Omega_0 \sigma}{2} \int_{-3}^{3} \sqrt{\left(\frac{\Delta_{i,1}}{\Omega_0}\right)^2 + 2\exp(-2x^2)} dx \quad . \tag{2.79}$$

Imposing the condition (2.76) and solving for $\sigma = \sigma(\omega_D, \Omega_0)$ yields

$$\sigma = \frac{2\pi}{\Omega_0}\left(\int_{-3}^{3} \sum_i \sqrt{\left(\frac{\Delta_{i,1}}{\Omega_0}\right)^2 + 2\exp(-2x^2)} dx\right)^{-1} \quad , \tag{2.80}$$

where the sum is taken over the four nuclear spin eigenstates. To mitigate the effect of decoherence caused by the decay of the excitation we minimise the duration of the pulse under the constraint that the conditions in Eqs. (2.73), (2.75) and (2.76) are fulfilled, thus obtaining an optimal σ^*.

We incorporate the decoherence caused by the optical decay by modelling the time evolution with the following Schrödinger picture master equation

$$\frac{d}{dt}\rho(t) = -i[\mathcal{H}_{\text{app}}(\sigma^*), \rho(t)] + \sum_\omega \Gamma(\omega)\Big(2A(\omega)\rho(t)A(\omega)^\dagger - \{A(\omega)^\dagger A(\omega), \tilde{\rho}(t)\}\Big) \tag{2.81}$$

in Lindblad form [36]. $\Gamma(\omega)$ is as defined by Eq. (2.45) and the Lindblad operators $A(\omega)$ are determined by (2.41), where the projectors project onto the eigenspaces of $H_{\text{asym,eff}}$ instead of $\mathcal{H}_{\text{app}}$. This simplification gives twelve (constant) incoherent decay channels, rather than considering time-dependent Lindblad operators and

re-evaluating the validity of the RWA at every instance in time (as would be required for the time-dependent Hamiltonian). Effectively, our approach then overestimates the destructiveness of the optical decay, thus giving a lower bound for the entanglement of formation of the nuclear spins.

Fig. 2.13 shows the results of a simulation that applies such an optimised Gaussian pulse with a pulse duration σ^*. For weak coupling strengths A and A', this approach achieves a somewhat lower value of the entanglement of formation than the dynamic 2π pulse discussed earlier. However, a similarly high-fidelity entangling operation is possible for stronger hyperfine coupling. The term 'adiabatic following' can invoke the impression that the desired operation will be much slower than a dynamical implementation. It is therefore astounding that our adiabatic pulse takes only about twice as along as the dynamic 2π pulse. Finally, we note that the adiabatic method (where the pulse is applied off-resonantly rather than having to hit a specific resonance) is inherently robust against pulse imperfections. This could be a significant advantage for experiments with ensembles of identical molecules. In this case, static and driving field inhomogeneities will inevitably lead to an over- or under-rotation of some of the ensemble spins when a dynamical pulse is applied (leaving the wrong excitation subspace populated), whereas the adiabatic approach ensures that all populations end up back in the correct spin levels.

2.5 Summary and discussion

In this chapter, we have given a detailed analysis showing how a transient optically excited state can be harnessed for the controlled generation of entanglement between two remote nuclear spins. We have identified control methods applicable over a wide range of system parameters and studied their performance with

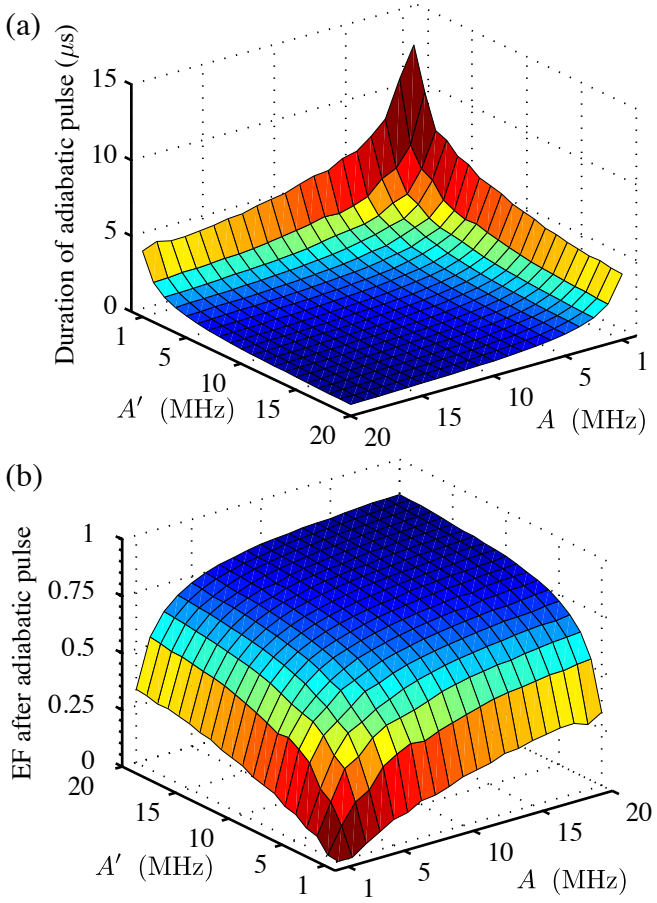

Figure 2.13: (a) Optimal duration of the adiabatic pulse $6\sigma^*$ optimised over ω_D and Ω_0. (b) Entanglement of formation after applying a Gaussian pulse whose duration is characterised by σ^*. As in Fig. 2.11, other parameters are: $\tau = 10\ \mu\text{s}, D = -320$ MHz, $\omega_e = 9.7$ GHz, $\omega_n = 5.97$ MHz and $\omega_{n'} = 14.74$ MHz.

regard to the predominant decoherence mechanism. For the symmetric system consisting of two identical nuclear spins as qubits, the free time evolution is naturally entangling, but the characteristic time scale of the dynamics depends on the state of the excitation and can vary over several orders of magnitude, opening up the possibility of effectively switching the interaction on and off. For an asymmetric system, a different route needs to be taken and we have presented one adiabatic and two dynamic methods for creating entanglement in this case. We have also included a discussion of the crossover regime between the asymmetric and symmetric system to establish the robustness of the symmetric operation.

We have shown that the symmetric control method can be remarkably robust against uncertainty or fluctuations in the coupling constants and nuclear Zeeman splittings. As another advantage of the symmetric system, the system can decay back to the ground state without destroying the nuclear spin coherence. Conversely, for the asymmetric system additional control is required for the de-excitation step, yet it is easier to address the nuclear spins individually for single qubit operations, initialisation and readout.

Interestingly, the active control methods proposed for the asymmetric system are much faster than waiting for the free time evolution in the symmetric case, and they can also be applied to the symmetric system if a short optical lifetime makes this approach advantageous. Finally, we note that the adiabatic control method is intrinsically more robust against control pulse and static field inhomogeneities, making it uniquely suitable for experiments with ensembles of identical systems. Astonishingly, the time required for such an adiabatic operation is only about twice as long as for its dynamical counterpart. At the moment of writing, experiments are performed with asymmetric molecules, and preliminary results suggest that the dynamic approach (CPHASE gate through a selective 2π pulse) gives rise to promising results [66]. In future experiments it will be exciting to see how these results compare to the adiabatic method proposed in this chapter.

Chapter 3

Quantum entanglement distribution using a magnetic field sensor

Contents

In the previous chapter, we have presented methods for the creation of entanglement between remote nuclear spins. In this research chapter, which is based on Ref. [161], we present another scheme for creating entanglement but this time for electronic spins. This method involves a very sensitive magnetic-field sensor. As we will see in Chapter 4, sensors based on crystal defects, especially nitrogen-vacancy (NV) centres in nanodiamond, can achieve detection of single magnetic moments. Here, we show that this exquisite control can be utilised to entangle remote electronic spins for applications in quantum computing; the mobile sensor provides a 'flying' qubit while the act of sensing the local field constitutes a two-qubit projective measurement. Thus, the tip mediates entanglement between

an array of well-separated (and thus well controlled) qubits. Our calculations establish that such a device would be remarkably robust against realistic issues such as dephasing, inaccurate timing and both positioning errors and multimodal vibrations in the sensor tip. Interestingly, the fact that this form of flying qubit is readily measurable allows one to convert certain classes unknown errors into heralded failures, which are relatively easy to deal with using established QIP techniques. We also provide calculations establishing the feasibility of performing a demonstrator experiment with a fixed sensor in the immediate future.

3.1 Introduction

One possible architecture for a quantum computer is based on the idea of distributed quantum information processing [48]. Individual qubits (or small groups of qubits) are physically well separated from one another, thus affording ease of control. The challenge is then to accomplish entanglement; it is known that suitable optically active qubits can be entangled by measurements on emitted photons [16, 114, 19]. In this chapter, however, we show how one can use the dipole-dipole interaction between electronic spins in conjunction with optical detected magnetic resonance (ODMR) to create entanglement between remote spin qubits that need not be optically active. The NV centre defects in diamond are very suitable for ODMR and QIP as these possess a long-lived spin triplet electronic ground state with the levels $|0\rangle$ and $|\pm 1\rangle$ that can be easily initialised with a laser, manipulated with microwave pulses and readout optically [203, 92]. This exquisite control enables observation of their coupling to adjacent nuclear spins [71, 60] and the measurement of a nearby nuclear spin [140]. A very promising application of NV centres is their capability to detect the strength of very small magnetic fields through an induced Zeeman splitting [185, 125, 12, 53, 163]. We

will show how this sensitivity can be used to entangle remote electronic spins in a remarkably robust fashion. Indeed because of the measurement-based nature of the operation, certain classes of experimental imperfection including finite decoherence time in the NV centre and both timing and positioning errors, can be probabilistically mapped to a far higher fidelity operation (with the other outcome being a *heralded* outright failure). Since it is established that QIP is possible with very high heralded error rates exceeding 90% [113], this is therefore a very powerful approach.

Ultimately, our proposal is to move an NV centre sensor between remote spins to entangle them. We begin by outlining a simpler experimental scenario, which could be tested in the immediate future. Suppose we are given two electronic spin qubits and we can measure the field of these two spins by using a crystal defect in a nanodiamond, which is placed in the middle of the two qubits [see Fig. 3.1(a)]. If each qubit produces a field of strength b_z at the site of the NV centre, then the NV centre experiences either $-2b_z, 0$ or $2b_z$ depending on the spin orientation of the qubits: the field is 0 if the two spins are in the state $|\uparrow\downarrow\rangle$ or $|\downarrow\uparrow\rangle$ and $\pm 2b_z$ if the two spins are in the state $|\downarrow\downarrow\rangle$ or $|\uparrow\uparrow\rangle$. Given a sufficiently large external magnetic field, we can prepare the NV centre in the state $|+\rangle_{\rm NV} = 1/\sqrt{2}\big(|0\rangle + |1\rangle\big)$. Over time t, this state collects either a phase of $\pm 2b_z\mu_{\rm NV}t/\hbar \equiv \omega_{\pm}t$ or 0 depending on the qubits, where $\mu_{\rm NV}$ denotes the magnetic moment of the NV centre. Measuring this phase will implement a projective two-qubit measurement. For example, suppose the two qubits are each prepared in the state $|+\rangle_{1/2} = 1/\sqrt{2}\big(|\downarrow\rangle + |\uparrow\rangle\big)$ and we let the NV centre precess for the time $\tau = \pi/\omega_+$, before measuring it in basis $|\pm\rangle_{\rm NV} = 1/\sqrt{2}\big(|0\rangle \pm |1\rangle\big)$. If the measurement results in $|+\rangle_{\rm NV}$, then the two qubits will be in the Bell state $1/\sqrt{2}\big(|\downarrow\uparrow\rangle + |\uparrow\downarrow\rangle\big)$. Similarly, the outcome $|-\rangle_{\rm NV}$ leaves us with $1/\sqrt{2}\big(|\downarrow\downarrow\rangle + |\uparrow\uparrow\rangle\big)$. Thus, a deterministic parity projection is realised, which is very robust to errors

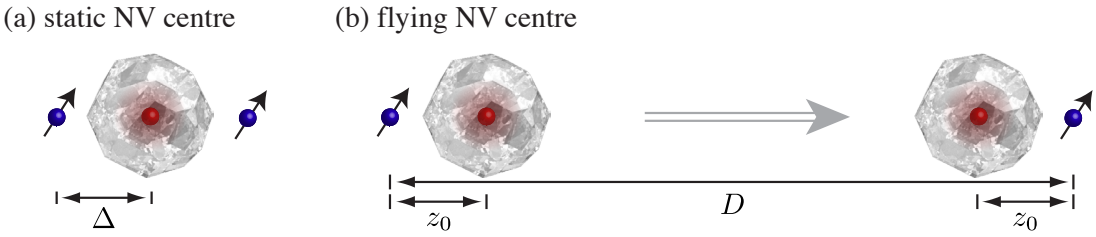

Figure 3.1: (a) An NV centre in a nanocrystal is placed in between two adjacent electronic spins qubits. (b) An NV centre is initially close to one qubit and then it is physically moved over to a second qubit that is remote from the former. In both cases the dipole-dipole interaction allows us to perform a projective two-qubit measurement.

as we will show in this chapter. Moreover, we will show that for other times τ the procedure still achieves a probabilistic parity projection, known to be sufficient to implement the entanglement needed for full QIP [16].

3.2 Basic scheme

We now show how robust this general idea is with respect to the translations and vibrations of the NV centre. First, we look at a configuration where the two qubits are located at the origin and at $z = 2\Delta$ while the NV centre, which is oriented along the z-direction, is placed in the middle of the two qubits [see Fig. 3.1(a)]. The interaction between the three particles is given by the dipole-dipole coupling:

$$H_{\mathrm{D},ij} = C_{i,j} d_{i,j}^{-3} \big(3(\hat{\mathbf{x}}_{i,j} \cdot \mathbf{S}_i)(\hat{\mathbf{x}}_{i,j} \cdot \mathbf{S}_j) - \mathbf{S}_i \cdot \mathbf{S}_j\big) \quad ; \tag{3.1}$$

where $\mathbf{S}_i$ is the spin-operator of the particle i, $\hat{\mathbf{x}}_{i,j}$ is a unit vector pointing from spin i to spin j, $d_{i,j}$ is the distance between the spins i and j and $C_{i,j} = -\frac{\mu_0}{4\pi}\mu_i\mu_j = C$ is a constant [112]. Here, μ_0 is the magnetic constant, $\mu_{1/2/\mathrm{NV}} = 2\mu_\mathrm{B}$ are the magnetic moments of the spins, and μ_B denotes the Bohr magneton. In an

external magnetic field B in z-direction, the whole system can be described by the following Hamiltonian:

$$H_{\text{static}} = H_0 + H_{\text{DIP}} \quad \text{with} \tag{3.2}$$

$$H_0 = -\mu_{\text{NV}} B S_{\text{z,NV}} + D_{\text{NV}} S_{\text{z,NV}}^2 - \mu_1 B S_{\text{z},1} - \mu_2 B S_{\text{z},2} \tag{3.3}$$

$$H_{\text{DIP}} = H_{\text{D,NV1}} + H_{\text{D,NV2}} + H_{\text{D},12} \quad , \tag{3.4}$$

here, $D_{\text{NV}} = 2.87$ GHz is the zero-field splitting (ZFS). We transform this Hamiltonian to a rotating frame with respect to $\exp(iH_0 t)$ and neglect fast oscillating terms originating from a sufficiently large external field and the ZFS (rotating wave approximation). This gives us:

$$\tilde{H}_{\text{static,RWA}} = H_{\text{D,app,NV1}} + H_{\text{D,app,NV2}} + H_{\text{D},12} \quad , \text{with} \tag{3.5}$$

$$H_{\text{D,app},ij} = 2C d_{i,j}^{-3} S_{\text{z},i} S_{\text{z},j} \quad . \tag{3.6}$$

Using a standard master equation [36] as follows we now evaluate the effect of dephasing upon our basic proposal:

$$\rho'(t) = -i[\tilde{H}_{\text{static,RWA}}, \rho(t)] + \sum_{j=1,2,\text{NV}} \frac{2}{T_{2,j}} \left(S_{j,\text{z}} \rho(t) S_{j,\text{z}}^\dagger - \frac{1}{2} \{ \rho(t), S_{j,\text{z}}^\dagger S_{j,\text{z}} \} \right) \quad . \tag{3.7}$$

We assume the three particles to be initially in the state

$$|\psi_{\text{i}}\rangle = |\psi(0)\rangle = |+\rangle_1 |+\rangle_{\text{NV}} |+\rangle_2 \quad . \tag{3.8}$$

After time t, we measure the NV centre in the $|\pm\rangle_{\text{NV}}$-basis. The readout can be implemented in several ways. At low temperature the readout of the NV centre spin can be done resonantly in one shot [202]. Although one cannot use such res-

onant measurements at higher temperature, a single shot measurement has been demonstrated at room temperature with the help of a nuclear spin in diamond [140]. This experiment involved transfer of information from the electron onto the nuclear spin via a CNOT-gate and employed projective measurements by using a quantum nondemolition scheme. Alternatively, at room temperature, it is possible to utilize a nonresonant technique. Here, due to the limited detection efficiency in the current technology, a single shot measurement is not possible, and therefore the entangling operation needs to be repeated many times [185]. The statistics of the repetitive entangling operations will eventually determine which parity between the static qubits is present. Fortunately, the nature of the operation we seek to perform, i.e. a parity projection, is such that an arbitrary number of repetitions will not change the state after the first application. Regardless of the implementation of the measurement, the qubits are after the measurement then, depending on the outcome, either in the state ρ_+ or ρ_-. This holds for both with the probability

$$p_\pm = \Big(1 \pm \exp(-t/T_{2,\mathrm{NV}}) \cos^2(\alpha t/2)\Big)/2 \quad , \tag{3.9}$$

where $\alpha = 2C\Delta^{-3}$. Within the limits of infinite dephasing times, $\rho_\pm = |\psi_\pm\rangle \langle\psi_\pm|$ are pure, where

$$|\psi_+\rangle = n_+\Big(e^{-i\alpha t} |\downarrow\downarrow\rangle + |\uparrow\uparrow\rangle + \frac{2e^{i\frac{3\alpha}{32}t}}{1+e^{i\alpha t}}(|\downarrow\uparrow\rangle + |\uparrow\downarrow\rangle)\Big) \tag{3.10}$$

$$|\psi_-\rangle = 1/\sqrt{2}(-e^{-i\alpha t} |\downarrow\downarrow\rangle + |\uparrow\uparrow\rangle) \tag{3.11}$$

and where n_+ is a normalisation factor. We find that the entanglement of formation [200] is given by

$$E_\mathrm{F}(\rho_-) = 1 \qquad \text{and} \qquad E_\mathrm{F}(\rho_+) = H\left(\frac{1}{2} + \frac{1}{2}\sqrt{1-\eta}\right) \quad , \tag{3.12}$$

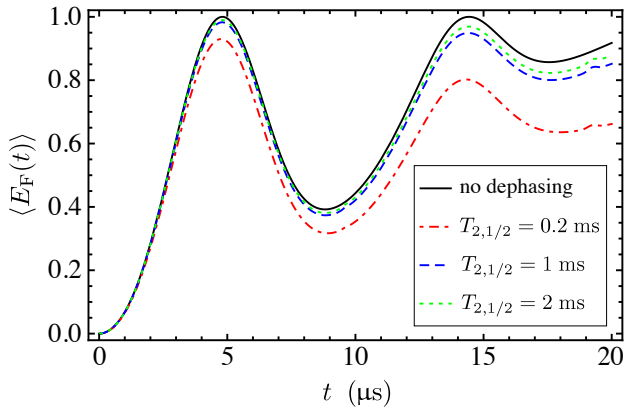

Figure 3.2: Static NV centre: mean EF with respect to the measurement time. For the nonsolid curves: $T_{2,\mathrm{NV}} = 2$ ms. The distance between the NV centre and the qubits is $\Delta = 10$ nm.

where

$$\eta = \frac{5 - 4\cos(\frac{3}{16}\alpha t)(1+\cos(\alpha t)) + \cos(\alpha t)(2+\cos(\alpha t))}{(3+\cos(\alpha t))^2} \quad . \tag{3.13}$$

Hence, whenever we measure the outcome $|-\rangle$, the qubits are maximally entangled. Note, for QIP, we could simply discard ρ_+ retaining ρ_- which represents a perfect parity projection if we know t.

In order to quantify the amount of entanglement between the qubits that we obtain after measuring the NV centre at time t, we calculate the mean EF, i.e.

$$\langle E_{\rm F}(t)\rangle := p_-\, E_{\rm F}(\rho_-) + p_+\, E_{\rm F}(\rho_+) \quad , \tag{3.14}$$

which we then plot with respect to the time of the measurement in Fig. 3.2. This figure displays the expected oscillatory behaviour due to the phase that the NV centre collects. In addition, one can show that the distortion of the oscillation is a result of the qubit-qubit coupling in Eq. (3.5) and as these terms are relatively small, they have negligible effect on the first maximum of the mean EF. Finally, we conclude that the effect of dephasing for the first maximum of the mean EF is

also small given large coherence times. At room temperature, in bulk diamond, coherence times of about 2 ms have been demonstrated [13, 139]. However, currently, due to impurities in and on the surface of nanodiamonds, these values are degraded to the order of microseconds [125, 186] and further investigations need to be carried out to improve these values. In this context decoupling techniques like in [139, 64] are very valuable, and these can be analogously applied on our spins. Another possibility of improving these values is to employ an amplified NV centre sensor scheme [163]. Here, an amplifier spin is attached on the surface of the nanodiamond so that the NV centre can be effectively brought closer to the static qubits. Thus, the NV centre can be placed in a larger nanocrystal, which can increase the coherence time of the NV centre.

3.3 Tolerating poor NV decoherence times

In addition, for short dephasing times of the NV centre, we can simply repeat the entangling operation in order to increase the amount of entanglement. Since we need to obtain measurement results of the same parity at each entangling operation, such repetitions tend to decrease the success probability. However, such repetitions drastically increase the fidelity of the entanglement under the effect of the dephasing of the NV centre. We quantify this idea by considering two qubits with infinite dephasing times and an NV centre with a short dephasing time. We repetitively apply our entangling operation, where each operation lasts for the time $t = \pi/|\alpha|$. If we measure the NV centre k times and consecutively obtain the outcome $|-\rangle$, then we call the state of the two qubits $\rho_{-,k}$. The success probability for such an event to happen also depends on the dephasing time of the NV centre. In Fig. 3.3, we plot the entanglement of formation for this state $\rho_{-,k}$ and the success probability with respect to the dephasing time of

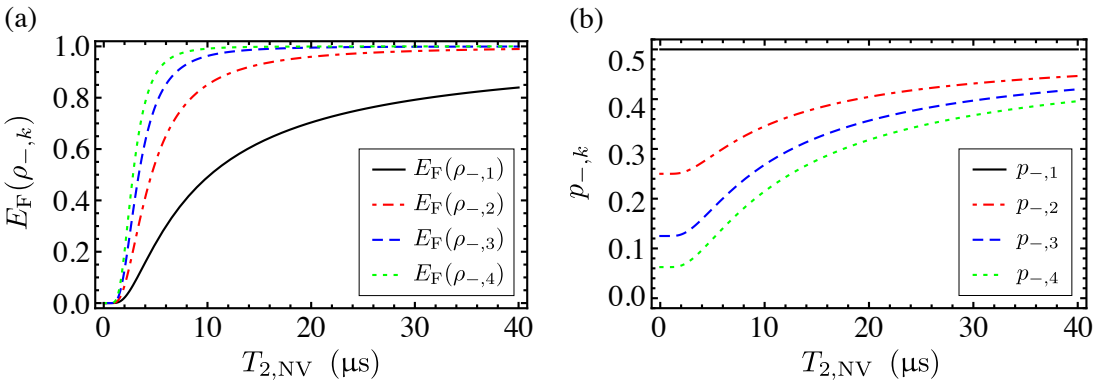

Figure 3.3: (a) Entanglement of formation of the two qubit state that we obtain after the entangling operation is performed k times in a row and each time the NV centre is found to be in the state $|-\rangle$. We plot the EF of the two qubits with respect to the dephasing time of the NV centre. (b) The success probability for such an event to happen is $p_{-,k}$, which we plot with respect to the dephasing time of the NV centre. In both plots we choose each entangling operations to last for the time $t = \pi/|\alpha|$ and set $\Delta = 10$ nm.

the NV centre. We see that the repetitions substantially increase the amount of entanglement.

The static qubits can be embodied by various sorts of spins. Mainly, these need to be stable under the optical illumination while the NV centre spin is readout. For this reason, $Sc@C_{82}$ that has an unpaired electron spin with a coherence time of 200 μs [132, 37] or the electron spins bound to donors in silicon are suitable. For the latter, coherence times of several seconds have recently been demonstrated at low temperatures [190]. It is remarkable that the NV centre spin can also be used to initialise and readout the qubits acting analogously to the read and write head in a classical Turing machine.

3.4 Implications of tip vibration

In a complete QIP system, the nanocrystal bearing our NV sensor would be mounted on an AFM-tip thus enabling it to move between various sites with

atomic resolution [88]. This mobility comes at the price of limited controllable vibrational modes of the AFM-tip, with typical frequencies varying between 50 kHz and 500 kHz [206] and amplitudes up to 1.5 nm [88]. To characterise the consequences of these vibrations for our entangling operation, we consider first the effect of the NV centre oscillating between the two qubits in a single mode, i.e. $d_{\mathrm{NV},1/2}(t) = \Delta \pm \delta \cos(\omega t + \phi)$; where δ denotes the amplitude, ω the frequency and ϕ the phase of the oscillation[1]. As above, we derive a rotating wave approximation Hamiltonian and end up with the time-dependent Hamiltonian

$$\tilde{H}_{\mathrm{vib,RWA}}(t) = H_{\mathrm{D,app,NV1}}(t) + H_{\mathrm{D,app,NV2}}(t) + H_{\mathrm{D,12}} \quad . \tag{3.15}$$

We can consider this vibrational scenario as a perturbed static case and thus we expect a maximum of the mean EF at around $\pi/|\alpha|$ (similar to Fig. 3.2). Note, for larger times the qubit-qubit coupling and the dephasing become relevant. For this reason we define the maximal achievable mean EF M to be

$$M = M(\delta, \omega, \phi) = \max_{0 \leq t \leq 2\pi/|\alpha|} \langle E_{\mathrm{F}}(t) \rangle \quad . \tag{3.16}$$

We are interested in how the introduction of many modes with various parameters (δ, ω, ϕ) affect this maximal achievable mean EF, and, in particular, for which parameter regime M is close to 1. For this purpose, we analyse the effect of many modes that share the common parameter p on M and define

$$\overline{\rho}^{p}(t) = \int_{-\infty}^{\infty} \mathcal{D}(p) \, |\psi(t,p)\rangle \, \langle \psi(t,p)| \, dp \tag{3.17}$$

[1] For a given amplitude δ, vibrations perpendicular to the axis connecting the qubits would change $d_{\mathrm{NV},1/2}(t)$ less dramatically than the on-axis vibrations. Taking all vibrations to lie along the axis connecting the qubits is therefore adequate to capture the worst case; moreover this assumption then admits analytic treatment.

as the mean density matrix with respect to the distribution $\mathcal{D}(p)$ of the parameter p; where $|\psi(t,p)\rangle$ is the solution of the Schrödinger equation for $\tilde{H}_{\text{vib,RWA}}(t)$. We find an analytic approximation of this solution as follows. First, we neglect the qubit-qubit coupling in $\tilde{H}_{\text{vib,RWA}}(t)$

$$\tilde{H}_{\text{vib,RWA,app}}(t) = H_{\text{D,app,NV1}}(t) + H_{\text{D,app,NV2}}(t) \quad . \tag{3.18}$$

We then transform this Hamiltonian to an interaction picture and expand it in a power series with respect to $\delta(t) = \delta\cos(\omega t + \phi)$. This gives:

$$\begin{aligned} H_{\text{I}}(t) &= \exp(i\tilde{H}_{\text{static,RWA}}t)\tilde{H}_{\text{vib,RWA,app}}\exp(-i\tilde{H}_{\text{static,RWA}}t) \\ &= \sum_{j=1,2}\frac{2C}{\Delta^3}\left((-1)^j 3\frac{\delta(t)}{\Delta} + 6\frac{\delta(t)^2}{\Delta^2} + \mathcal{O}(\delta(t)^3)\right) S_{\text{z,NV}}S_{\text{z},j} \quad . \end{aligned} \tag{3.19}$$

Finally, we apply time-dependent perturbation theory:

$$\begin{aligned} \rho_{\text{I}}(t) = \rho_{\text{I}}(0) &- i\int_0^t [H_{\text{I}}(t'), \rho_{\text{I}}(0)]dt' \\ &+ (-i)^2\int_0^t\int_0^{t'} [H_{\text{I}}(t'), [H_{\text{I}}(t''), \rho_{\text{I}}(0)]]dt''dt' \quad , \end{aligned} \tag{3.20}$$

where $\rho_{\text{I}}(0) = |\psi_{\text{i}}\rangle\langle\psi_{\text{i}}|$ and get an analytic approximation of the solution of the Schrödinger equation for Eq. (3.15). The first order approximation in δ reads:

$$\begin{aligned} \rho_{\text{I}}(t) = \rho_{\text{I}}(0) + i\frac{6C}{\Delta^4}\delta\frac{\sin(\omega t+\phi)-\sin(\phi)}{\omega} \\ \times [S_{\text{z,NV}}S_{\text{z},1} - S_{\text{z,NV}}S_{\text{z},2}, \rho_{\text{I}}(0)] \quad . \end{aligned} \tag{3.21}$$

This approximation allows us to understand the effect of many modes. First, we analyse the effect of many vibrational modes with different frequencies. In Fig. 3.4(a), we compare our approximation with the exact solution for (3.15) by plotting the maximal achievable mean EF for $\overline{\rho}^{\omega}$ (in both cases) with respect

to the vibration frequency ω for different amplitudes and for a particular phase. For the average $\overline{\rho}^{\omega}$ in Eq. (3.17), we use a truncated normal distribution on $[0,\infty)$ with mean ω and standard deviation $\sigma = 0.01\omega$. In the static case, we have seen that the mean EF is maximal when we wait about time $\pi/|\alpha|$ before we measure the NV centre. First, assume the NV centre is initially in the middle of the two qubits ($\phi = \pi/2$). If the NV centre oscillates for $1/2 + k$ periods (k periods) before it is measured, where k is a non-negative integer, then the asymmetry in the system is maximal (minimal) and we get a low (high) mean EF. Obviously for a large k, this effect is less pronounced. The minus sign in the commutator in Eq. (3.21) describes exactly this asymmetry which decreases for large frequencies and thus the perturbative solution (3.21) explains the characteristics of Fig. 3.4(a). We note that analogous plots where we increase and decrease the width of the frequency distribution are not very sensitive to the width of the distribution which is in agreement with the rate in Eq. (3.21).

Second, we can repeat this analysis by averaging over the amplitude instead of the frequency, i.e. by considering $\overline{\rho}^{\delta}$. Again we see from Eq. (3.17) that averaging over a reasonably narrow truncated normal distribution on $[0,\infty)$ has little effect, and hence, we get the same plot as in the analysis before.

Third, we analyse the effect of many vibrational modes with different phases. Thus, we assume a uniform distribution of phases on $[0, 2\pi]$. With Eq. (3.20), we obtain in second order in δ the following density matrix

$$\begin{aligned}\overline{\rho}_{\mathrm{I}}^{\phi}(t) = \rho_{\mathrm{I}}(0) - i6\frac{C}{\Delta^5}\delta^2 t[S_{\mathrm{z,NV}}S_{\mathrm{z},1} + S_{\mathrm{z,NV}}S_{\mathrm{z},2}, \rho_{\mathrm{I}}(0)] \\ - 18\frac{C^2}{\Delta^8}\delta^2\frac{1-\cos(\omega t)}{\omega^2} \\ \times [S_{\mathrm{z,NV}}S_{\mathrm{z},1} - S_{\mathrm{z,NV}}S_{\mathrm{z},2}, [S_{\mathrm{z,NV}}S_{\mathrm{z},1} - S_{\mathrm{z,NV}}S_{\mathrm{z},2}, \rho_{\mathrm{I}}(0)]] \quad .\end{aligned} \tag{3.22}$$

Again we compare this approximation with the exact solution for (3.15) by plot-

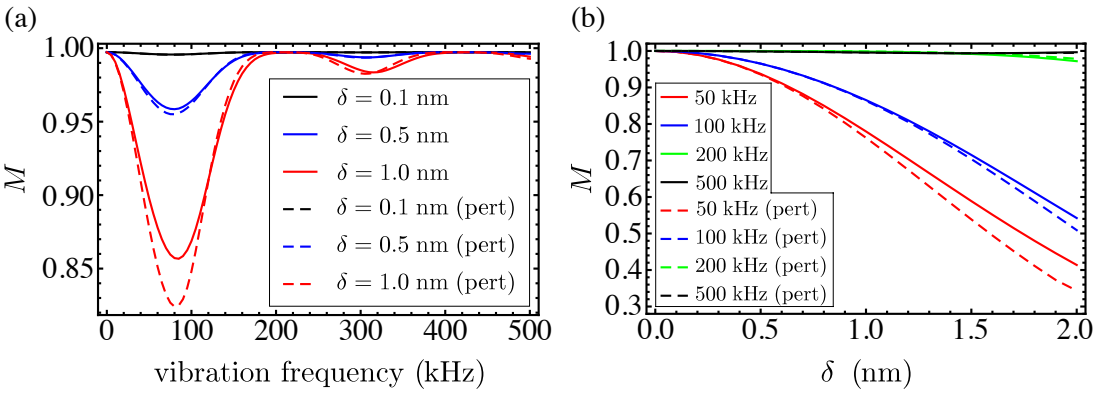

Figure 3.4: (a) Maximal achievable mean EF for vibration modes where the vibration frequencies (amplitudes) are distributed according to a truncated normal distribution on $[0, \infty)$; with mean ω (δ) and standard deviation 0.01ω (0.01δ), i.e. $\overline{\rho}^{\omega}$ ($\overline{\rho}^{\delta}$) with respect to the mean (common) vibration frequency $\omega/2\pi$ for different common (mean) vibration amplitudes δ and $\phi = \pi/2$. (b) Maximal achievable mean EF for vibration modes where the phase is uniformly distributed, i.e. $\overline{\rho}^{\phi}$ with respect to their common vibration amplitude δ for different common vibration frequencies. In both plots the solid lines are calculated from the numerical solution of the von Neumann equation for $\tilde{H}_{\text{vib,RWA}}(t)$ and the dashed lines are calculated by using the approximations discussed in the text. Here $\Delta = 10$ nm.

ting in Fig. 3.4(b) the maximal achievable mean EF with respect to the vibration amplitude for different frequencies and find a good agreement between the two solutions, especially for small amplitudes. We see that the last term in Eq. (3.22) can be seen as a (time-dependent) decoherence rate and explains why higher frequencies and smaller amplitudes are less disturbing to our entangling operation.

In summary, we conclude that oscillations of the NV centre do not cause a substantial adverse effect for our entangling operation provided that they are relatively fast and of low amplitude.

3.5 Moving NV centre between remote locations

Having established that the measurement of a static NV centre can entangle two nearby spins, and having further determined that the realistic issues of dephasing

and oscillation do not present fundamental difficulties, we can now characterise our full protocol with two *remote* spins and a moving, or 'flying', NV centre. Therefore, we consider a distance $D \gg \Delta$ between the two qubits and propose that the NV centre should now fly from one qubit to the other, i.e. from $z = z_0$ to $z = D - z_0$ with velocity v. Hence, the NV centre interacts first with qubit 1 and then with qubit 2 before it is measured at $t_{\mathrm{M}} = (D - 2z_0)/v$ [see Fig. 3.1(b)].

As above we derive with the time-dependent distances $d_{\mathrm{NV},1}(t) = tv + z_0$ and $d_{\mathrm{NV},2}(t) = D - tv - z_0$ the following rotating frame approximation Hamiltonian

$$\tilde{H}_{\mathrm{flying,RWA}}(t) = H_{\mathrm{D,app,NV1}}(t) + H_{\mathrm{D,app,NV2}}(t) \quad , \tag{3.23}$$

where we neglect the qubit-qubit coupling due to the large distance between the qubits.

Again, we initialise the three spins in the state $|\Psi_{\mathrm{i}}\rangle = |\psi_{\mathrm{i}}\rangle$ [see Eq. (3.8)]. The Schrödinger equation determines the state $|\Psi(t_{\mathrm{M}})\rangle$ when the NV centre travelled from one qubit to the other. The measurement of the NV centre in the $|\pm\rangle_{\mathrm{NV}}$-basis projects the qubits to one of the states

$$|\Psi_-\rangle = (-e^{i\beta}\,|{\downarrow\downarrow}\rangle + |{\uparrow\uparrow}\rangle)/\sqrt{2} \quad \text{or} \tag{3.24}$$

$$|\Psi_+\rangle = N_+\Big(e^{i\beta}\,|{\downarrow\downarrow}\rangle + |{\uparrow\uparrow}\rangle + \frac{2e^{i\beta}}{1+e^{i\beta}}(|{\downarrow\uparrow}\rangle + |{\uparrow\downarrow}\rangle)\Big) \tag{3.25}$$

with the probability:

$$p_{\mathrm{fly},-} = \sin^2(\beta/2)/2 \;\text{ and }\; p_{\mathrm{fly},+} = (3 + \cos(\beta))/4 \quad , \tag{3.26}$$

where $\beta = C\left((D - z_0)^{-2} - z_0^{-2}\right)/v$ and N_+ is a normalisation factor. The EF of the first state is 1 and that of the second state is given by the binary entropy

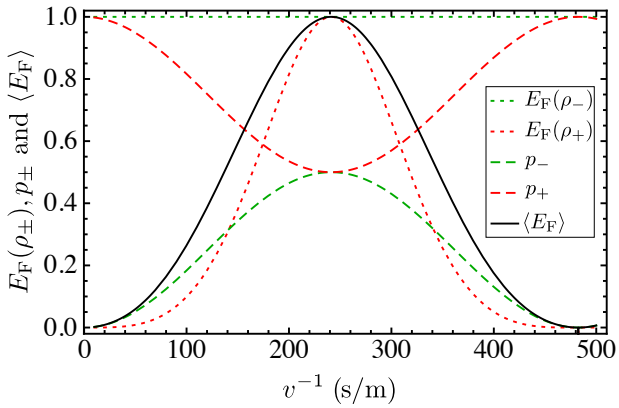

Figure 3.5: Flying NV centre: EFs, mean EF and success probabilities as a function of the inverse velocity v^{-1} when the NV centre has moved from one qubit to the other. Parameters: $D = 100$ nm, $z_0 = 5$ nm.

function H

$$E_F(\rho_+) = H\left(\frac{1}{2} + \frac{1}{2}\sqrt{1-\xi^2}\right) \text{ with } \xi = \frac{1-\cos(\beta)}{3+\cos(\beta)} \quad . \tag{3.27}$$

Hence, whenever $\beta = \pi \bmod 2\pi$, the entangling operation is maximally entangling. Again, for very fast velocities, we could discard ρ_+ retaining ρ_- and still achieve a (probabilistic) maximally-entangling parity projection. In Fig. 3.5, we plot the EFs and probabilities around the velocity for which $\beta(v) = \pi$.

3.6 Robustness – imperfections in the phase acquisition

We conclude this chapter by discussing a very remarkable robustness property, originating from the fact that we measure the NV centre. For this analysis, we consider the special case in which we aim to implement a parity projection that is deterministic, i.e. $t = \pi/(2|\alpha|)$ in the static case and $\beta = \pi \bmod 2\pi$ for the flying NV centre scenario. The interaction part of the entangling operation can effectively be described by two unitaries acting on the system. These unitaries

are

$$U_{1/2} = \exp\left(-i\frac{\pi}{2}(1+\delta_{1/2})S_{\mathrm{NV,z}}S_{1/2,\mathrm{z}}\right) \quad , \tag{3.28}$$

where $\delta_{1/2}$ denotes the (relative) imperfection in the phase acquisition. A typical example of an error, for which then $\delta_{1/2} \neq 0$, is given by timing errors due to imprecise knowledge of the physical distances in the system. Another example is an uncertainty in the speed of the flying NV centre.

As we have seen before, the measurement of the NV centre implements a parity projection on the qubits. It is determined by the general measurement operators

$$M_{\pm}(\delta_1,\delta_2) = \langle \pm|_{\mathrm{NV}}\, U_2 U_1\, |+\rangle_{\mathrm{NV}} \quad . \tag{3.29}$$

In the computational basis of the qubits, these operators have the following representation

$$M_{\pm} = \frac{1}{2}\begin{pmatrix} \pm 1 - e^{-\frac{1}{2}i\pi(\delta_1+\delta_2)} & 0 & 0 & 0 \\ 0 & \pm 1 + e^{-\frac{1}{2}i\pi(\delta_1-\delta_2)} & 0 & 0 \\ 0 & 0 & \pm 1 + e^{\frac{1}{2}i\pi(\delta_1-\delta_2)} & 0 \\ 0 & 0 & 0 & \pm 1 - e^{\frac{1}{2}i\pi(\delta_1+\delta_2)} \end{pmatrix} \quad . \tag{3.30}$$

Again, we assume that the two qubits are initially in the $|+\rangle\,|+\rangle$ state, and the measurement of the NV centre yields the two qubit state $\rho_{\pm}$. In Fig. 3.6(a), we plot the entanglement of formation of the state ρ_{-} with respect to the relative errors $\delta_{1/2}$. We see that even for errors of several percent, the resulting state posses an entanglement of formation that is greater than 0.99, and therefore our method is very robust with respect to errors.

Even more worthy of attention is that, in case the errors are systematic (i.e. the same in consecutive applications of the entangling operation), a simple repetition of the entangling operation significantly increases the entanglement of formation

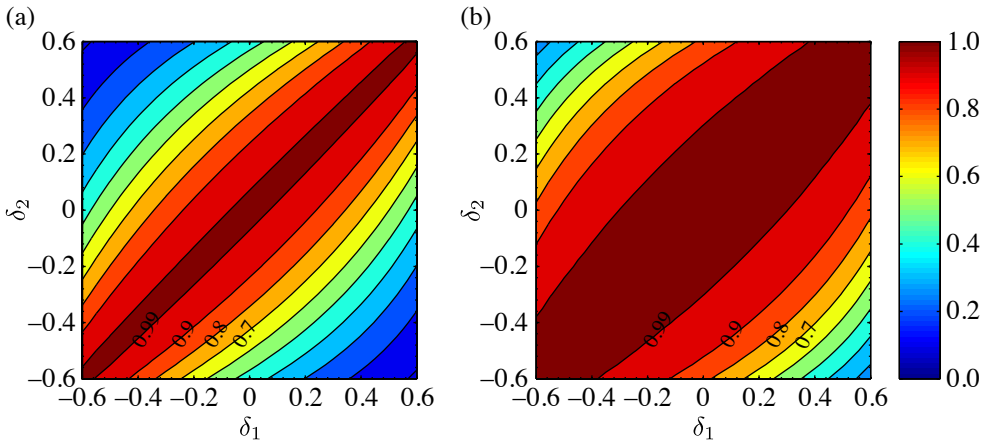

Figure 3.6: (a) Entanglement of formation of the two qubits, after the entanglement operation described in the text projected the NV centre onto the $|-\rangle$ state, with respect to the relative errors $\delta_{1/2}$ in phase acquisition. (b) Entanglement of formation of the two qubits, after two successive applications of the entanglement operation described in the text projected the NV centre each time onto the $|-\rangle$ state, with respect to the relative errors $\delta_{1/2}$ in phase acquisition.

if the measurement outcome of the second round is the same as in the first round. Note that the probability to measure $|\pm\rangle$ in the first round is about 1/2 and the probability to measure $|\pm\rangle$ again in the second round is close to unity as long as the dephasing of the NV centre is negligible. In Fig. 3.6(b), we consider the case, where the outcomes of two successive measurements is $\{|-\rangle, |-\rangle\}$, and we plot the entanglement of formation of the resulting state $\rho_{-,2}$ with respect to the two relative errors $\delta_{1/2}$. We see that the second measurement drastically increases the robustness of our scheme, and therefore, it easily tolerates errors of more than 10 percent.

3.7 Summary and discussion

In summary, for this chapter we present an entanglement operation that is based on sensing small magnetic fields. Our calculations establish that this opera-

tion can be performed within the coherence time of the qubits. Repetitions of the entangling operation compensate the effect of dephasing of the NV centre. Moreover, imperfections in the scheme caused by vibrations of the NV centre are tiny for high frequencies and low amplitudes. A particular strength of the scheme is its enormous robustness with respect to timing errors. Especially, repetitions of the entangling operation mitigate the effect of systematic errors. Eventually, remote qubits can be entangled by physically moving the NV centre mounted, for example, on an AFM-tip between the two qubits – making the entangling operation of high value for a distributed quantum computer architecture.

To implement our proposal, several experimental challenges need to be overcome. The first task is to synthesise a small nanocrystal (a diameter of 20 nm is enough) that embeds a single NV centre with a long enough dephasing time. As we have shown in this chapter, over the course of several microseconds a large amount of entanglement can be obtained. For an NV centre in a nanocrystal with diameter of 7 nm a dephasing time of 1.4 µs has been measured [186]. The small dephasing time is related to the small size of the nanocrystal as for NV centres in bulk diamond dephasing times of milliseconds have been measured [13, 139]. Hence, for a bigger nanocrystal that we require in our scheme a larger dephasing time can be expected.

Another challenge that QIP with NV centres faces is the loss of photons while the NV centre is readout. A perfect measurement could be performed in about 20 ns [186]. However, severe photon loss in current experiments increases this time significantly and would harm the success of our entanglement operation. There are several approaches for increasing the detection efficiency, for example by using a tapered fibre or a plasmonic waveguide [45]. A successful implementation of these ideas for NV centres in nanodiamonds would be highly beneficial for more or less all technologies based on nanodiamonds with NV centres including

magnetic-field sensors that we discuss in the next chapter. Therefore, we can expect much experimental progress in this respect.

Chapter 4

Spin amplification for magnetic sensors employing crystal defects

Contents

As outlined in the introduction of this thesis, quantum computing is not the only application of QIP. For example, in the previous chapter, we came across a very sensitive magnetic-field sensor based on crystal defects in diamond. In this chapter, which is based on Ref. [163], we propose an augmented sensor consisting of an NV centre for readout and an 'amplifier' spin system in order to map the magnetic properties of a surface at the single (nuclear) spin level. This proposal brings the sensor 'effectively' closer to the sample, as the sensing is done with the amplifier spin and the detection with the NV centre. Our calculations show that this hybrid structure has the potential to detect magnetic moments with a

sensitivity and spatial resolution far beyond that of a simple NV centre.

4.1 Introduction

A key objective for future sensor technologies is the detection of weak magnetic fields at molecular length scales. There are numerous potential applications in materials science, medical science and biology. An ambitious goal would be to detect the field due to single nuclear spins, in order to gain direct information about the structure of a molecular complex deposited on the surface. This would require unprecedented combination of sensitivity and spatial resolution.

Among the most sensitive magnetic field sensing devices are Hall sensors [155], SQUID sensors [90], force sensors [154], and potentially NV centres in diamond [125, 185, 12, 53, 208]. Experimental work has progressed rapidly, enabling, e.g., real-time imaging via frequency locking [167] and nanoscale electric field detection [58]. The sensitivity of NV-centre-based magnetometers is steadily improving [119], and a field-gradient allows spatial resolution almost approaching the nanometer scale for proximal spins [80]. Very recently, the detection of spins evidently on the nanocrystal surface has been reported [81].

In this chapter, we propose a significant improvement of the NV centre sensor by coupling it to an amplifying spin system (see Fig. 4.1). We show that the improvement in magnetic moment sensitivity can be expected to be of about three orders of magnitude; indeed the augmented NV centre may have the highest in-principle performance of any such device.

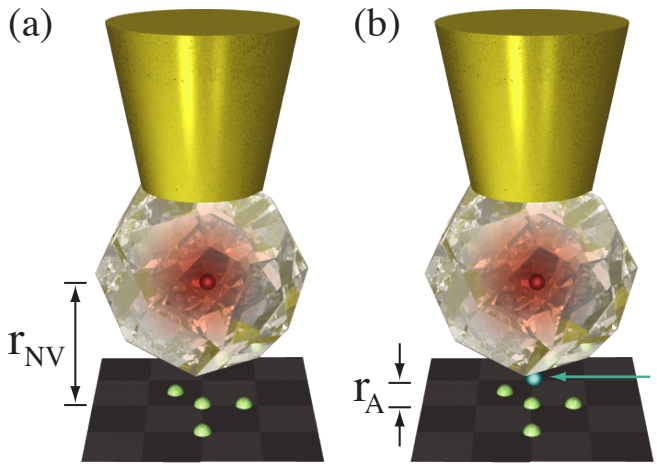

Figure 4.1: (a) Conventional sensor structures: an NV centre (red sphere) is embedded in the middle of a diamond nanocrystal that is attached to an AFM-tip (yellow cone). The strength of the magnetic field generated by local spins (green spheres) can be inferred by measuring the NV centre through optical means and manipulating it with microwaves. (b) Amplified NV centre sensor: the surface of the nanodiamond is decorated with an another spin system (blue sphere) that couples to the NV centre inside the diamond. This additional spin system has an amplifying effect and enormously increases the magnetic field sensitivity of the sensor and its spatial resolution.

4.2 Magnetic moment sensitivity of a single spin

We begin with a general discussion of measuring an unknown magnetic field using two energy levels of a probe spin s system ($2s \in \mathbb{N}$), the underlying principle of the NV centre sensor. Let the probe spin be governed by the Zeeman Hamiltonian $H = -\mu_{\mathrm{Prb}}(B_0 + B)S_z$, where μ_{Prb} is the magnetic moment of the probe spin, S_z is the usual spin operator, B_0 is a known external field applied in the z-direction, and B corresponds to the magnetic field (also in the z-direction) that we wish to estimate. Consider two eigenstates $|0\rangle$ and $|1\rangle$ of H whose z-projections differ by an integer m. The field estimation then proceeds as follows: we start by creating the superposition $|+\rangle$ [here $|\pm\rangle = 1/\sqrt{2}(|0\rangle \pm |1\rangle)$], for example, by using a suitable microwave or radio-frequency pulse sequence. This state evolves in time to $|\psi(t)\rangle = 1/\sqrt{2}(|0\rangle + \exp(im\mu_{\mathrm{Prb}}(B_0 + B)t/\hbar)\,|1\rangle)$, and therefore, by successive measurements of the spin, we can infer the strength of the magnetic field. In

any real-world experiment the state $|\psi(t)\rangle$ will also be affected by decoherence processes, typically dephasing is predominant [171]. In this case, the coherence between $|0\rangle$ and $|1\rangle$ decays as $\exp(-\gamma(t))$ for a positive nondecreasing function $\gamma(t)$. The time evolution of the two level system's density matrix $\rho(t)$ is then fully described by

$$\rho(t) = \frac{1}{2}\begin{pmatrix} 1 & e^{i\phi t-\gamma(t)} \\ e^{-i\phi t-\gamma(t)} & 1 \end{pmatrix} \quad \text{with} \quad \phi = m\mu_{\text{Prb}}(B_0+B)/\hbar \quad . \tag{4.1}$$

The uncertainty of estimating B is limited from below by the quantum Cramér-Rao bound (CRB), i.e. even for an ideal system and perfect measurements the uncertainty in δB cannot become smaller than b_{CR} [see Eq. (1.31)]. The CRB is given by the inverse square root of the quantum Fisher information F with respect to B [34, 149], yielding the following inequality

$$\delta B \geq b_{\text{CR}} = \frac{1}{\sqrt{F}} = \frac{e^{\gamma(\tau)}\hbar}{m\tau\,|\mu_{\text{Prb}}|} \quad , \tag{4.2}$$

where τ is the duration for which the spin has experienced the magnetic field. Repeating the measurement many times gives a further reduction in the uncertainty of the unknown field. Assuming the preparation of the $|+\rangle$ state takes the time t_p, the lower bound for the uncertainty δB after $N = T/(\tau + t_p)$ repetitions within a total time T is given by

$$b_{\text{CR}} = \frac{1}{\sqrt{NF}} = \frac{e^{\gamma(\tau)}\hbar\sqrt{\tau+t_p}}{\sqrt{T}m\tau\,|\mu_{\text{Prb}}|} \quad . \tag{4.3}$$

As an example, we set $\gamma(t) = \frac{t}{T_2}$. Minimising the CRB with respect to τ yields the optimal sensing time for each run of the protocol:

$$\tau^* = \frac{1}{4}\left(T_2 - 2t_p + \sqrt{T_2^2 + 4t_p\,(3T_2+t_p)}\right) \quad . \tag{4.4}$$

It is easily seen that $\tau^* \approx \frac{1}{2}T_2$ in the limit of weak dephasing ($T_2 \gg t_p$), in contrast to $\tau^* \approx T_2$ when the dephasing time is comparatively short, $T_2 \ll t_p$.

Since a magnetic field smaller than b_{CR} cannot be resolved, the CRB provides a natural limit of the sensitivity of a magnetic field sensor. Interestingly, this limit does not depend on the actual value of B. However, a naïve intuition is that the proximity of the probe spin and the sample will be an important characteristic of a practicable sensor, since it determines the strength of the measured magnetic field as well as the sensor's spatial resolution. To quantify this intuition, one can ask the question: how long does it take until the sensor spin detects the magnetic moment associated with an electron or a nuclear spin? In the following, we introduce a magnetic moment sensitivity (in units of $\mathrm{T}/\sqrt{\mathrm{Hz}}$) as a suitable figure of merit for this question: the magnetic moment sensitivity S of a sensor is given by the number of proton magnetons that can be resolved within the time window $\sqrt{T}$ for a distance r between the probe spin and the sample. The dipole field originating from a proton with magnetic moment μ_p at the position of the probe spin is of order $b = \frac{\mu_0}{4\pi}\frac{2\mu_p}{r^3}$ (where μ_0 is the vacuum permeability), so we obtain

$$S = \frac{\min_\tau(b_{\mathrm{CR}})\sqrt{T}}{b} \quad . \tag{4.5}$$

For example, once again assuming $\gamma(t) = \frac{t}{T_2}$ and employing Eq. (4.4) gives the following magnetic moment sensitivity

$$S = \frac{2\pi\hbar}{\mu_0\mu_p}\frac{e^{\frac{\tau^*}{T_2}}\sqrt{\tau^* + t_p}r^3}{m\tau^*\left|\mu_{\mathrm{Prb}}\right|} \quad . \tag{4.6}$$

We briefly introduce the NV centre as a system for field sensing before describing the inherent limitations of this approach and presenting our proposal for improving the characteristics of this class of device. An NV centre in dia-

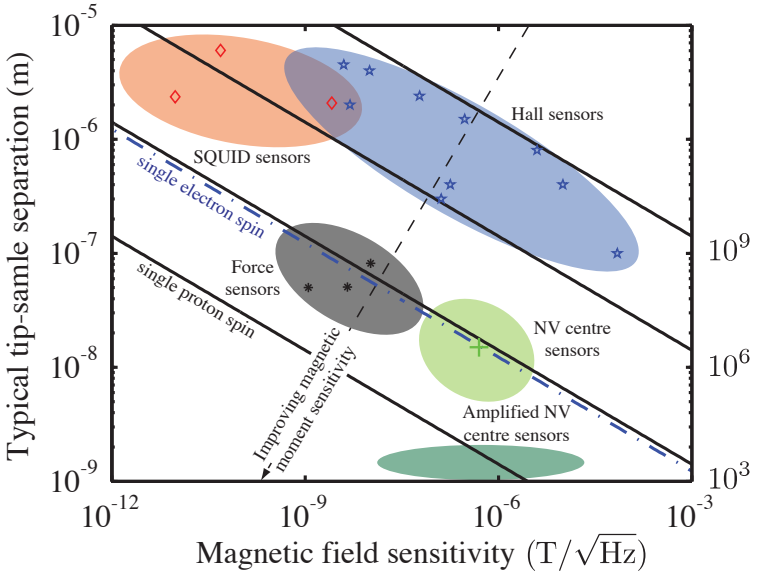

Figure 4.2: Performance of various state-of-the-art and proposed magnetic field sensors (figure adapted from Ref. [52]). The plot shows magnetic sensitivity (per $\sqrt{\text{Hz}}$) (horizontal) versus a typical tip-sample separation. The data points are reported sensitivities from experiments: force sensors [158, 54, 121], Hall sensors [30], SQUID sensors [98, 73, 90], and NV centre sensors [125]. The diagonal lines sketch the boundaries for the magnetic moment sensitivity [see Eq. (4.5)] required to detect $1, 10^3, 10^6$, or 10^9 protons (solid black) and a Bohr magneton (blue dash dotted) within one second. The potential of our proposed preamplified NV centre is illustrated by the dark green ellipse.

mond possesses spin-1 with the three levels $|0\rangle$ and $|\pm1\rangle$. The levels $|\pm1\rangle$ are degenerate in the absence of an external field and shifted from $|0\rangle$ by a zero-field splitting (ZFS) of about 2.87 GHz. For the purpose of sensing the magnetic field, various two level manifolds can be used, for example, $\{|0\rangle, |\pm1\rangle\}$ or $\{1/\sqrt{2}(|1\rangle+|-1\rangle), (1/\sqrt{2}(|1\rangle-|-1\rangle)\}$ [185]. In the first case the energy levels are split by $D \mp \frac{1}{2}g\mu_B B$ and in the second case by $g\mu_B B$ (for $g \approx 2$). Under the assumption of equal dephasing rates, this implies that the sensitivity of the second pair of levels is twice as large as the sensitivity of the first pair [see Eq. (4.3)].

4.3 Sensitivity of the amplified NV centre sensor

Figure 4.2 shows the magnetic moment sensitivity of various classes of sensors. Clearly, NV centres hold the promise of a high field sensitivity combined with a fairly small probe to sample separation. However, in order to further improve the spatial resolution and obtain an even better magnetic moment sensitivity (according to the definition in Eq. (4.5)) the NV centre must be brought even closer to the sample. Due to the cubic dependence of S on r even a modest reduction in the separation leads to a large gain, and for this reason NV centres have been embedded in smaller and smaller nanocrystals [12, 125]. However, the size of the diamond crystal surrounding the NV centre cannot become arbitrarily small without severely affecting the remarkable coherence time (and thus the sensitivity) of the NV centre. In ^{12}C isotopically enriched bulk diamond the room temperature coherence time can be as long as 1.8 ms [13], increasing up to 2.4 ms with dynamic decoupling [139]. On the other hand, the best reported coherence time for a nanodiamond with a diameter of 7 nm is reduced to 1.4 µs [186]. Smaller crystals with a diameter of only 5 nm have been studied in Ref. [33], however, the properties of enclosed NV centres are even further degraded in this case. A miniaturisation of the crystal hence leads to a reduced field sensitivity in exchange for a smaller separation between the probe and the sample.

We propose to overcome this trade-off situation by bringing the NV centre 'effectively' closer to the sample without reducing the size of the nanocrystal. This is achieved by attaching an additional spin system on the surface of a nanocrystal, which relays the sample magnetic field to the NV centre through the dipole coupling (see Fig. 4.1). In the simplest implementation, a single electron spin serves as the amplifier. There is a large set of stable $S = 1/2$ organic radicals with coherence times up to 200 µs, which could be attached to the nanocrystal

surface [93, 115, 195, 37]. Further improvements may be possible by using higher spin systems such as N@C_{60} (which has $T_2 = 80$ µs at room temperature) [135] or a molecular magnet [123, 47]. It may even be possible to make use of more sensitive entangled states with suitably engineered molecular systems [94, 164].

For simplicity, we consider an $S = 1/2$ electron spin as the amplifier in the following. The NV centre and the amplifier spin are dipole coupled, and we assume the vector connecting the two spins is aligned with the z-axis. Both spins experience a (known) homogeneous external magnetic field $\mathbf{B}_0 = (0, 0, B_0)$ and a small magnetic field whose z component B at the position of the amplifier is to be measured. In comparison to the amplifier spin the NV centre experiences a weaker sample field cB where the factor $c < 1$ depends on the relative separations. The Hamiltonian thus reads:

$$H = -\mu_{\mathrm{NV}}(B_0 + cB)S_{\mathrm{NV},z} + D_{\mathrm{NV}}S_{\mathrm{NV},z}^2 - \mu_A(B_0 + B)S_{A,z} \\ - d(2S_{\mathrm{NV},z}S_{A,z} - S_{\mathrm{NV},x}S_{A,x} - S_{\mathrm{NV},y}S_{A,y}) \quad , \quad (4.7)$$

where $d = \frac{\mu_0}{4\pi}\frac{\gamma_{\mathrm{NV}}\gamma_A\hbar}{\Delta^3}$ is the dipolar coupling constant; γ_{NV} and γ_A are the gyromagnetic ratios of the spins, Δ is the distance between the NV centre and the amplifier spin, and D_{NV} denotes the NV centre's ZFS constant. Our protocol assumes that the influence of cB on the NV centre is much smaller than its coupling to the amplifier spin; this will certainly be justified if the amplifier is an electron spin and the sample field is due to nuclear spins. In addition, we assume that flip-flops between the spins are heavily suppressed and can be neglected, for example, because D_{NV} represents the largest energy in the system, yielding the following effective Hamiltonian

$$H \approx -\mu_{\mathrm{NV}}B_0S_{\mathrm{NV},z} + D_{\mathrm{NV}}S_{\mathrm{NV},z}^2 - \mu_A(B_0 + B)S_{A,z} - 2dS_{\mathrm{NV},z}S_{A,z} \quad , \quad (4.8)$$

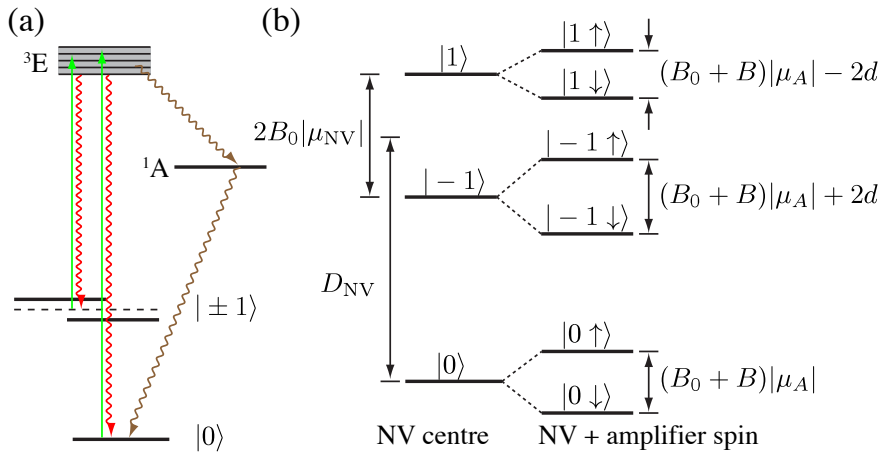

Figure 4.3: (a) Level structure of an NV centre. The ground state is a spin triplet with zero field splitting and the excited state has a manifold of levels. Following excitation with green light the dominant decay is spin preserving. However, spin is not always conserved due to an additional decay path to $|0\rangle$ via a metastable state, so that continuous excitation eventually results in a polarised state. (b) Eigenspectrum of H for an amplifier spin-$\frac{1}{2}$ system. In this diagram we used the convention: $S_{{\rm NV},z}\,|i\rangle = i\,|i\rangle$, $S_{A,z}\,|\uparrow\rangle = |\uparrow\rangle$ and $S_{A,z}\,|\downarrow\rangle = -\,|\downarrow\rangle$

whose level structure is schematically depicted in Fig. 4.3.

The field sensing protocol now proceeds as follows. Initially, the system starts in a completely mixed spin state, $\frac{1}{6}\mathbf{1}_6$, so that it needs to be polarised with laser and microwave pulses. As a first step we polarise the NV centre by illuminating it with green light, after about 1 µs the NV centre will have relaxed to the state $|0\rangle$ with high probability [185], leaving the combined system in the state $|0\rangle\langle 0| \otimes \frac{1}{2}\mathbf{1}_2$. Next, we apply a selective microwave π pulse on the transition $|0\rangle\,|\downarrow\rangle \leftrightarrow |1\rangle\,|\downarrow\rangle$. For a distance $\Delta = 10$ nm between the NV centre and the amplifier, this transition is split from the neighbouring $|0\rangle\,|\uparrow\rangle \leftrightarrow |1\rangle\,|\uparrow\rangle$ transition by $2d = 2\frac{\mu_0 g_{\rm NV} g_A \mu_B^2}{4\pi\Delta^3\hbar} \approx 0.65$ Mrad/s (i.e. 104 kHz). A highly selective π pulse is beneficial for the presently discussed protocol. For this reason we now establish the conditions under which imperfections in the pulse selectivity can be considered negligible. Assuming Lorentzian line broadening of both transitions with a FWHM of $2/T_{2,{\rm NV}}$ ($T_{2,{\rm NV}}$ is the coherence time of the NV centre), a detailed

analysis[1] shows that a linewidth overlap of up to 10% of the common area under the two lines meets this requirement and translates into $T_{2,\mathrm{NV}} > 10\ \mu\mathrm{s}$. The product of pulse duration and frequency passband $T \times \Delta\omega$ is typically between 2 and 5 [27]. Taking $T = 4/\Delta\omega$ and allowing the passband to overlap with the area of unwanted transition's Lorentzian by at most 5% (allowing us to neglect imperfect pulse selectivity), we thus obtain $\tau_\pi = \frac{4}{2(2d - \cot(0.05\pi)/T_{2,\mathrm{NV}})}$ for the duration of the desired selective π pulse (reducing to $\tau_\pi \approx 1/d$ in the limit of long $T_{2,\mathrm{NV}}$).

Finally, the state of the NV centre is measured. There are several ways of performing this measurement. At low temperature, the $|0\rangle$ state can be resonantly excited, and hence a single-shot readout is possible [202]. However, at room temperature the excitation with a laser can only be done nonresonantly, and therefore, the entire triplet ground state is always excited at once. In this case, the NV centre exhibits spin-dependent photoluminescence, before ultimately being pumped into the $|0\rangle$ state. For the foreseeable future, experiments will only detect a tiny fraction of the emitted photons [185]. Therefore many repetitions may be necessary for conclusive measurements. As each readout cycle pumps the NV centre spin into the $|0\rangle$ state, we either continuously reiterate the selective π pulse described above after each measurement or employ a nearby nuclear spin analogously to Ref. [140]. For now, we consider the case, where the NV centre is read out nonresonantly and the selective π pulse is repeatedly applied after each measurement cycle, and refer to the appendix of the this chapter for the other two ways of reading out the NV centre spin. As it turns out, all three ways of reading out the NV centre spin show a similar performance. Independently of

[1] In general, a reduced π pulse selectivity gives rise to two types of error: firstly, a mixed initial state, resulting in a correction factor of $(1+p)/(1-p)$ for the sensitivity S_A, where p describes the proportion of the population flipped in the unwanted transition. Secondly, a degradation of the Fisher information entailing an additional correction factor of $\sqrt{(1+p)/(1-p)}$. Both factors are very close to 1 as long as the pulse remains highly selective.

the measurement, the system is left in one of the well-defined states $|0\rangle|\downarrow\rangle$ or $|0\rangle|\uparrow\rangle$.

Without loss of generality we assume the system is in the state $|0\rangle|\downarrow\rangle$, ready for the magnetic field estimation through several repetitions of the following sensing cycle: A microwave $\frac{\pi}{2}$ pulse creates the superposition $1/\sqrt{2}(|0\downarrow\rangle + |0\uparrow\rangle)$. It is safe to assume that the amplifier spin can be rotated fast and with high fidelity as long as the unknown field corresponds to the smallest energy scale of the system, as can be accomplished with a modest external field. After a sensing time τ, the amplifier spin acquires a relative phase proportional to B. The phase is first mapped onto a population difference between $|0\downarrow\rangle$ and $|0\uparrow\rangle$ with another $\frac{\pi}{2}$ pulse, and then entangled with the NV centre spin state with a selective π pulse in the same way as in the initialisation process. The NV centre spin state is now read out (also initialising it for the next sensing cycle).

4.4 Benchmark of the amplified NV centre sensor

Having described the protocol, we now benchmark the sensitivity improvement of the amplified system over a conventional single NV centre sensor. Obviously, the performance of both sensors depends on the decoherence model, which we assume to be fully characterised by $\gamma(t)$. Different forms of $\gamma(t)$ occur corresponding to different predominant dephasing mechanisms, however, typically $\gamma(t)$ can be written as $(t/T_2)^n$ for $n = 1, 2$ or 3 [186, 185].

For our comparison, we consider the levels $|0\rangle$ and $|1\rangle$ of an NV centre in the middle of a nanocrystal with radius 10 nm and a control and measurement duration of $t_{p,\mathrm{NV}} \approx 1$ µs per cycle. For the traditional NV centre sensing scheme, the fact that the vast majority of photons emitted is lost in typical experimental settings implies that we need to repeat the measurement many times to detect a

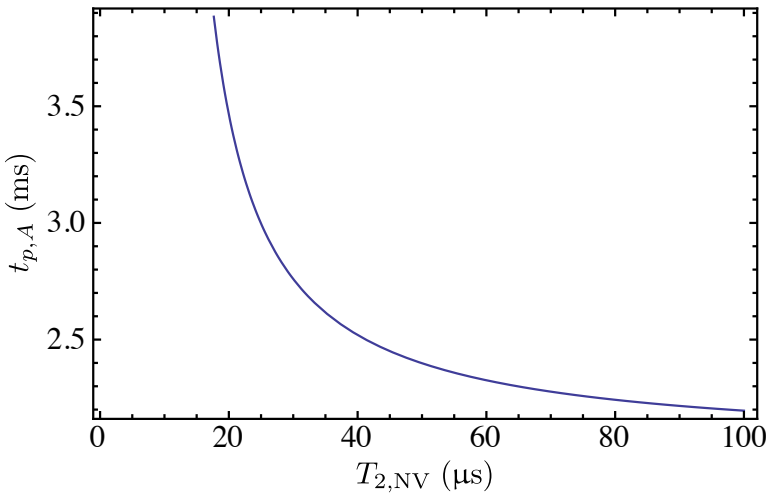

Figure 4.4: Preparation time necessary for the amplifier spin NV centre sensor with respect to the dephasing time of the NV centre $T_{2,\mathrm{NV}}$. Parameters: $t_{p,\mathrm{NV}} = 1\ \mu\mathrm{s}$, $R = 0.2$, $\eta = 0.05$ and $\Delta = 10$ nm.

sufficient number of photons to allow any inferences about the spin state of the NV centre. We can account for this photon shot noise limitation by modifying the magnetic moment sensitivity given in Eq. (4.5) as $S_{\mathrm{off}} = S/(R\sqrt{\eta})$, where R is the measurement contrast and η is the detection efficiency [3, 2]. Recent experiments with single NV centres found values of $R \approx 0.2$ and $\eta \approx 0.001$ [13, 12, 125]. However, with a tapered fibre or a plasmonic waveguide the detector efficiency could be improved to about $\eta = 0.05$ [45]. In contrast, using the electron spin on the surface of the augmented sensor entails an additional control overhead of about τ_π in each measurement cycle, i.e. $t_{p,A} \approx N(t_{p,\mathrm{NV}} + \tau_\pi)$, where N is the number of cycles: $N = \frac{1}{R^2\eta}$. Here, we have assumed that the T_1 time of the amplifier spin is much longer than $t_{p,\mathrm{A}}$. In Fig. 4.4 we plot $t_{p,\mathrm{A}}$ as a function of the dephasing time $T_{2,\mathrm{NV}}$ of the NV centre.

For the ratio of the magnetic moment sensitivity of both methods we obtain

$$\frac{S_{\mathrm{NV}}}{S_A} = \frac{1}{R\sqrt{\eta}} \frac{\exp(\gamma_{\mathrm{NV}}(\tau^*_{\mathrm{NV}}))\sqrt{\tau^*_{\mathrm{NV}} + t_{p,\mathrm{NV}}}\tau^*_A}{\exp(\gamma_A(\tau^*_A))\sqrt{\tau^*_A + t_{p,A}}\tau^*_{\mathrm{NV}}} \frac{r^3_{\mathrm{NV}}}{r^3_A} \quad . \tag{4.9}$$

In order to fairly compare both methods, we assume the same dephasing mech-

anism for the NV centre and the amplifier spin. We consider the three cases $\gamma_i(t) = \left(\frac{t}{T_2}\right)^i$ for $i = 1, 2, 3$. By assuming that $t_{p,A} \gg T_{2,A}$ and $t_{p,\mathrm{NV}} \ll T_{2,\mathrm{NV}}$, we find that the optimal sensing times in Eq. (4.9) are given by $\tau^*_{A,1} = T_{2,A}$, $\tau^*_{A,2} = \frac{1}{\sqrt{2}} T_{2,A}$ and $\tau^*_{A,3} = 3^{-1/3} T_{2,A}$ and $\tau^*_{\mathrm{NV},1} = \frac{1}{2} T_{2,\mathrm{NV}}$, $\tau^*_{\mathrm{NV},2} = \frac{1}{2} T_{2,\mathrm{NV}}$ and $\tau^*_{\mathrm{NV},3} = 6^{-1/3} T_{2,\mathrm{NV}}$, where the index $i = 1, 2, 3$ labels which of the γ_i is used as the dephasing model. Under these assumptions, we can derive an approximation for the ratio in Eq. (4.9)

$$\frac{S_{\mathrm{NV}}}{S_A} \approx C_i \frac{T_{2,A}}{\sqrt{T_{2,\mathrm{NV}}}\sqrt{t_{p,\mathrm{NV}} + \tau_\pi}} \frac{r^3_{\mathrm{NV}}}{r^3_A} \quad , \tag{4.10}$$

where only the prefactor depends on the choice of the dephasing model as follows: $C_1 = \sqrt{2/e}$, $C_2 = e^{-1/4}$ and $C_3 = \left(\frac{2}{3e}\right)^{1/6}$. Interestingly, this ratio does not depend on the measurement contrast R nor the detector efficiency η. This means that both strategies are affected by the imperfect measurement in the same way.

Figure 4.5 shows the (exact) ratio S_{NV}/S_A with respect to the amplifier coherence time $T_{2,\mathrm{A}}$ for several illustrative values of $T_{2,\mathrm{NV}}$. The red regions of the inset show the parameter space for which our protocol is not necessarily advantageous, either due to excessive line-broadening preventing a highly selective π pulse on the transition $|0\rangle|{\downarrow}\rangle \leftrightarrow |1\rangle|{\downarrow}\rangle$, or because $T_{2,\mathrm{NV}}$ is so much larger than $T_{2,\mathrm{A}}$ that it more than compensates the benefit of the amplifier spin. Figure 4.5 impressively demonstrates that the magnetic moment sensitivity can be enhanced by up to three orders of magnitude for $T_{2,\mathrm{NV}} \approx T_{2,\mathrm{A}}$ with realistic parameters. Further improvements may be feasible by substituting the electron spin amplifier with a high spin system or molecular magnet.

We now turn to another important consideration: Given a sensor that can resolve magnetic fields at the level of the single Bohr or even nuclear magneton, its spatial resolution is vitally important for many applications such as mapping the

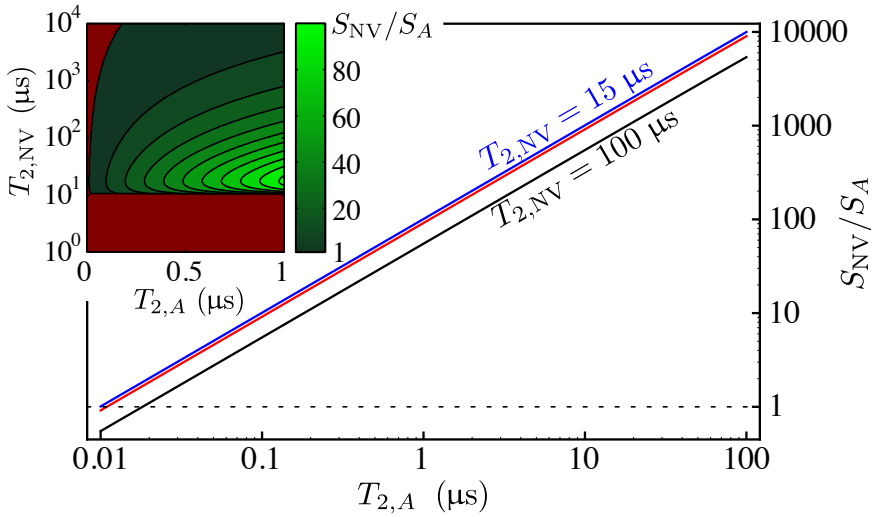

Figure 4.5: Ratio S_{NV}/S_A as a function of the amplifier spin coherence time $T_{2,\mathrm{A}}$ for $T_{2,\mathrm{NV}} = 100$ μs (black), 30 μs (red) and 15 μs (blue). This ratio gives the factor by which the amplified sensor outperforms a conventional NV centre sensor. Here, $\gamma(t) = t/T_2$, but we note that the curves for $\gamma(t) = (t/T_2)^{2,3}$ differ approximately only by a prefactor, see Eq. (4.10). Other parameters: $r_A = 1$ nm, $r_{\mathrm{NV}} = 11$ nm, $\Delta = 10$ nm, $t_{p,\mathrm{NV}} = 1$ μs, $t_{p,\mathrm{A}} = 1/(R^2\eta)(t_{p,\mathrm{NV}} + \tau_\pi)$, $R = 0.2$, $\eta = 0.05$. Inset: excessive line-broadening or a significant mismatch in the coherence times prevent a sensitivity enhancement in the red region (see text).

constituent molecules and nuclei of complex organic molecules. Unsurprisingly, it is highly beneficial to be able to move very close to the sample in order to reliably distinguish individual magnetic moments. Figure 4.6 shows the z component (i.e. the measured component) of the magnetic field for a regular array of protons at two different heights above the surface. If the probe sample separation is of order the distance between individual dipoles, the nuclear spins can be unambiguously resolved (given the required field sensitivity). On the other hand, the field is almost indistinguishable from that of a single stronger dipole if the sensor is scanning at $z = 10$ nm, even with the ability to sense small magnetic fields of order 1 nT.

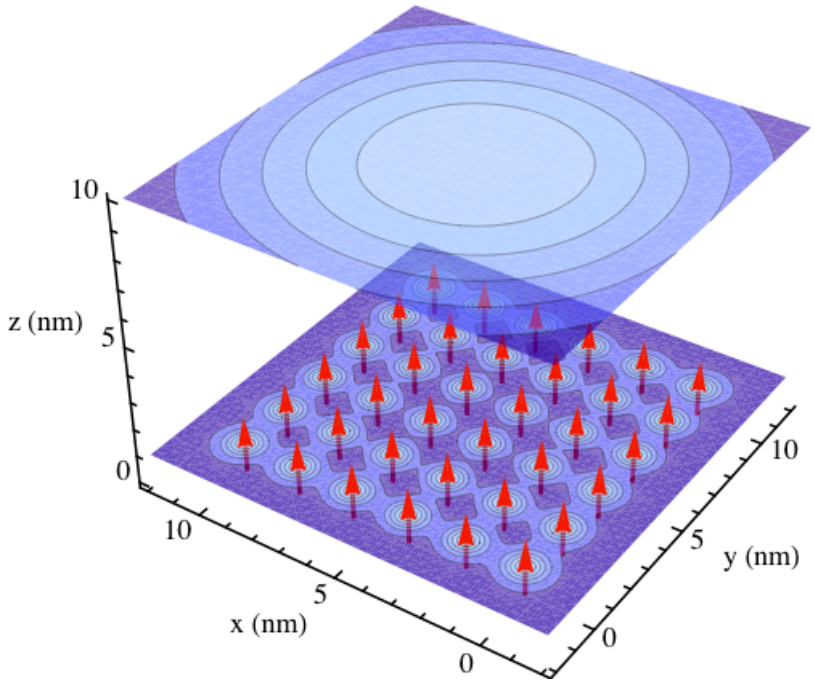

Figure 4.6: The z component of the magnetic field of a regular array of protons calculated in two planes $z = 1$ nm and $z = 10$ nm. The 36 dipoles with the magnetic moment of a proton are placed in the $z = 0$ plane, pointing into the z-direction as indicated by the red arrows. The field range of the contour plots spans 43.2 nT in the $z = 10$ nm plane and 2.61 μT for $z = 1$ nm. Individual dipoles are easily resolved at $z = 1$ nm, but at a distance of 10 nm their field looks similar to that of a single stronger magnetic moment. Spatially resolving individual spins at this distance requires a sensitivity that goes far beyond the amount of detail reflected in this plot.

4.5 Summary and discussion

In summary, we have proposed a practical way of enhancing NV centre based magnetic field sensor with a preamplifier system. Such an augmented sensor possesses a magnetic moment sensitivity that is capable of resolving individual protons, both in terms of their field strength as well as spatially on an atomic scale. The sensor consists of two essential parts: the NV centre for optical readout coupled to an entirely spin-based system for the magnetic field detection in close proximity to the sample. Despite this partitioning of tasks, the fundamental complexity of this improved sensor design is similar to that of existing proposals

and implementations.

The experimental state of the art is that for the first time it has been demonstrated in Ref. [81] that it is possible to detect spins that are outside the nanocrystal (here the conventional sensor is used), and there is evidence that these spins are located on the surface of the nanocrystal. The challenges to implement our amplified sensor scheme are first, that a nanodiamond with an embedded NV centre of long enough coherence time needs to be synthesised. For this purpose, it is necessary to understand the reason for the short dephasing times currently observed in non-bulk diamond. A more technical challenge will be to gain good control of the amplifier spin with microwave pulses.

Appendix 4.A Other measurement strategies

4.A.1 Resonant readout of the NV centre spin

At low temperatures the $|0\rangle$ state can be excited resonantly (selectively) enabling single-shot readout. The resonant excitation takes about 5 ms [202], which of course implies that the T_1 time of the NV centre spin needs to be longer than this time. We plot the ratio for this case, which is

$$\frac{S_{\mathrm{NV}}}{S_A} = \frac{\exp(\gamma_{\mathrm{NV}}(\tau^*_{\mathrm{NV}}))\sqrt{\tau^*_{\mathrm{NV}} + t_{p,\mathrm{NV}}}\tau^*_A}{\exp(\gamma_A(\tau^*_A))\sqrt{\tau^*_A + t_{p,A}}\tau^*_{\mathrm{NV}}} \frac{r^3_{\mathrm{NV}}}{r^3_A} \tag{4.11}$$

in Fig. 4.7.

Again, we can find an approximation for the ratio in Eq. (4.11). As $t_{p,\mathrm{NV}} \approx$

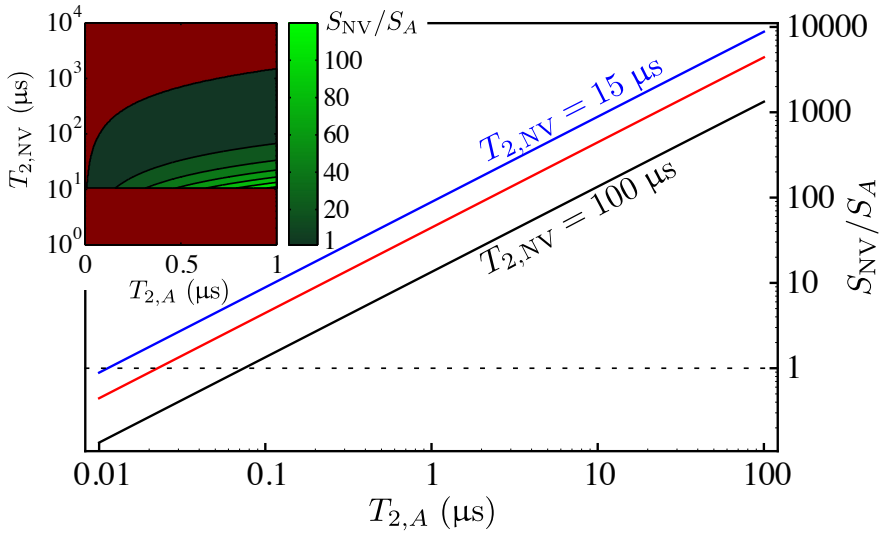

Figure 4.7: Resonant readout of the NV centre spin. Main plot: the ratio S_{NV}/S_A as a function of the amplifier spin coherence time $T_{2,\mathrm{A}}$ for $T_{2,\mathrm{NV}} = 100$ µs (black), 30 µs (red) and 15 µs (blue). This ratio gives the factor by which the amplified sensor outperforms a conventional NV centre sensor. Here, $\gamma(t) = t/T_2$, but we note that the curves for $\gamma(t) = (t/T_2)^{2,3}$ look almost identical. Parameters: $t_{p,\mathrm{NV}} = 5\,\mathrm{ms}, t_{p,\mathrm{A}} = t_{p,\mathrm{NV}} + \tau_\pi$ $r_A = 1\,\mathrm{nm}, r_{\mathrm{NV}} = 11\,\mathrm{nm}, \Delta = 10\,\mathrm{nm}$. Inset: excessive line-broadening or a significant mismatch in the coherence times prevent a sensitivity enhancement in the red region (see text).

5 ms, it holds that $t_{p,\mathrm{NV}/A} \gg T_{2,\mathrm{NV}/A}$, yielding

$$\frac{S_{\mathrm{NV}}}{S_A} \approx \frac{T_{2,A}}{T_{2,\mathrm{NV}}} \frac{r_{\mathrm{NV}}^3}{r_A^3} \sqrt{\frac{t_{p,\mathrm{NV}}}{t_{p,A}}} = \frac{T_{2,A}}{T_{2,\mathrm{NV}}} \frac{r_{\mathrm{NV}}^3}{r_A^3} \sqrt{\frac{t_{p,\mathrm{NV}}}{t_{p,\mathrm{NV}} + \tau_\pi}} \quad , \tag{4.12}$$

which is entirely independent of the choice of $\gamma_i(t)$.

4.A.2 Readout using a local memory

A third way of reading out the electron spin of the NV centre is given by employing a nuclear spin (with a long T_1 time) in the immediate vicinity of the NV centre as a temporary memory. The amplifier spin state is here transfered to this nuclear spin, e.g. via the NV centre electron spin. This can also be accomplished at room temperature. A projective measurement is now possible using a

quantum nondemolition scheme in the way described by Ref. [140]. Like in the previous section $t_{p,\mathrm{NV}} \approx 5$ ms and we thus obtain similar results.

Chapter 5

Quantum metrology with molecular ensembles

Contents

In this last research chapter, which is based on Ref. [164], we investigate the measurement of the magnetic-field strength using an ensemble of spins, whereas in the previous chapter we only considered an individual spin system. As multiple spins are utilised for sensing, a measurement device can be built that is fundamentally superior to conventional technologies. Specifically, when quantum entanglement is harnessed the precision achieved is supposed to scale more favourably with the resources employed, such as system size and the time required. In the following analysis, we will see that for an ensemble of spins another essential resource needs to be considered: the change in ensemble polarisation (entropy increase) during the metrology experiment. Accounting for this resource enables a fair comparison of the two standard strategies in quantum metrology: a classical strategy

where spins are used individually and a quantum strategy where an entanglement operation is performed on the spins. In this comparison, we incorporate the special nature of the measurement of spin ensembles. We shall find that the performance for sensing of both strategies depends crucially on the decoherence present in the system. In particular, we identify the parameter regime, where the quantum strategy can beat the classical strategy.

5.1 Introduction

Quantum metrology deals with the physical limits to measurement. Typically, one prepares a probe system of size K in a suitable initial state; this system acquires information about the quantity of interest, and then the probe system is measured. The process may be repeated either with a series of probes over time or, as in the present analysis, with multiple probe systems simultaneously. In Section 1.5.3, we have seen that the way in which the probe is prepared is closely related to the uncertainty of the parameter estimation: if prepared in a non-entangled state then the minimal uncertainty achievable scales with $1/\sqrt{K}$ [152], the standard quantum limit. However, this limit can be beaten if we allow arbitrary states for the preparation of the probe system (i.e. if we include entangled states), as demonstrated in recent experiments [109, 138, 151, 5]. In idealised cases, the minimal uncertainty achievable scales with $1/K$ – the Heisenberg limit [78, 79] – which can be achieved by making use of special entangled states such as Greenberger-Horne-Zeilinger (GHZ) states or maximally path-entangled $\frac{1}{\sqrt{2}}(|N,0\rangle + |0,N\rangle)$ (NOON) states [108].

In optical quantum metrology, the probe system is a particular state of K photons, for example, a NOON state, which is a superposition of 'all K photons in channel A' with 'all photons in channel B'. When an optical element indu-

cing an unknown phase shift is placed in channel A, then the probe acquires an internal phase K times as great as that which would be acquired by a single photon, and information about this phase is measured through an interference effect. In the present analysis, we consider an analogous experiment involving K atomic spins in a large molecule, which probes the strength of an external magnetic field. An essential difference is that we consider a large ensemble of probe molecules, which are necessarily prepared, exposed to the field, and ultimately measured *collectively* [94, 178] – that is, addressing of individual probe molecules is impossible.

The dynamics of an ensemble is typically observed by measuring the free-induction decay (FID) spin signal. Monitoring the FID can be seen as a continuous and simultaneous measurement of two non-commuting observables [63]. Here, the observed system is barely altered by the measurement, as the number of spins in a typical sample is usually so large. This type of measurement has not yet been analysed in the context of quantum metrology. Rather, recent studies have looked at the effect of temperature on the Fisher information of three types of states [128] and waveform estimation and its implications for quantum sensing [187].

5.2 Magnetic field sensing

In this chapter, we compare two strategies for measuring a small shift δB of a probe magnetic field from a reference field in a spin ensemble setting [94, 178]. This problem is equivalent to measuring the Larmor frequency $\delta = \frac{\delta B}{\gamma}$ of a precessing spin in the probe field, where γ is the gyromagnetic ratio. In the *quantum* strategy, we consider a macroscopic ensemble of N sensor molecules each consisting of K spins where each molecule is prepared in a very sensitive entangled

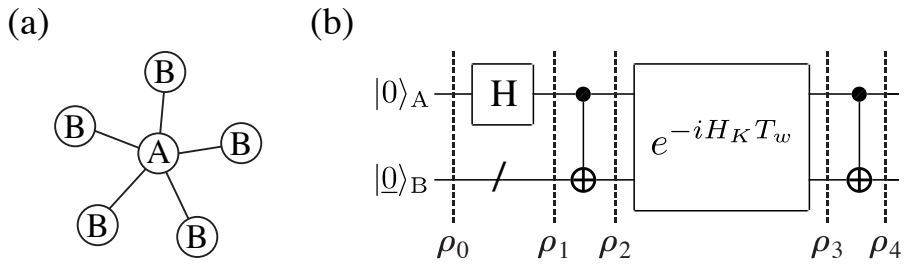

Figure 5.1: (a) Schematic of a sensor molecule with five satellites. (b) Quantum circuit employed in the quantum strategy.

state (see Fig. 5.1). This state senses the field for a wait time T_w by acquiring a phase $K\delta T_w$. We then map the phase onto one spin of the molecule from which it can be read out by observing the FID. As a performance benchmark, we compare this to the *classical* or *standard* strategy, where we determine the Larmor frequency by observing the FID of the same number of uncoupled spins. We will focus on the resources consumed by the two strategies and on the impact of decoherence.

The role of decoherence is very non-trivial. In the absence of decoherence and for a perfect projective measurement, the lowest achievable uncertainty in estimating δ scales with $1/K\sqrt{N}$ for the quantum strategy and $1/\sqrt{KN}$ for the classical strategy [78, 79]. Hence, the discrepancy in the precision of the two strategies increases with the size of the entangled state K. However, the spins will be subject to decoherence in any real-world experiment, and the sensitive entangled states will decohere faster than separable states when K becomes larger [171, 91]. This increased effective decoherence rate competes with the enhanced precision, making it difficult to predict the performance of the quantum strategy.

In the following, we shall determine lower bounds for the uncertainty of the parameter estimation from a measured FID for both strategies. First, we must generate a suitable entangled state to obtain enhanced sensitivity with the quantum strategy, meaning we require some amount of quantum control over the mo-

lecules. The details of how this is accomplished are unimportant, and we will in following, consider the example shown in Fig. 5.1; molecules with this star topology have been employed in recent experiments [94, 178]. Each molecule consists of one central spin A and $K-1$ non-interacting satellites of type B. The satellites interact with the central spin through an Ising type interaction, leading to the following Hamiltonian in an external magnetic field (in natural units, i.e. $\hbar = 1$):

$$H_K = \gamma\delta\sigma_z^A + \delta\sum_{j=1}^{K-1}\sigma_z^{B_j} + J\sum_{j=1}^{K-1}\sigma_z^A \otimes \sigma_z^{B_j} \quad , \tag{5.1}$$

where σ_z denotes the usual Pauli matrix with eigenvalues $\pm\frac{1}{2}$. δ denotes the Zeeman splitting of the B spins and $\gamma = \frac{\gamma_A}{\gamma_B}$ denotes the ratio of the gyromagnetic numbers of A and B, and we assume $\gamma \approx 1$. J describes the Ising interaction strength and is only necessary for implementing the multi-qubit gates in the quantum strategy, not for the sensing process. δ is the parameter to be estimated.

We focus on the fundamental comparison between classical and quantum strategy given a fully polarised initial state of the sample:

$$\rho_0 = |0\rangle_A \langle 0|_A \otimes |0\ldots0\rangle_B \langle 0\ldots0|_B = |0\underline{0}\rangle \langle 0\underline{0}| \quad , \tag{5.2}$$

where the underscore denotes the state of the $K-1$ satellite spin register. For the example molecule shown in Fig. 5.1(a), the entangled state can be constructed from this initial state by applying the pulse sequence shown in Fig. 5.1(b), i.e. first a Hadamard gate on the central spin and then a CNOT gate (control qubit = central spin, target qubits = satellites). The resulting GHZ state $\frac{1}{\sqrt{2}}\big(|0\underline{0}\rangle + |1\underline{1}\rangle\big)$ freely evolves for a time T_w, acquiring phase K times faster than a single spin [1]. However, at the same time, it is also more vulnerable to decoherence. In

[1] Strictly, this is only a GHZ state for $K > 2$ and a Bell state for $K = 2$. In Ref. [94], this

practice, the dephasing rate of an individual spin $\alpha = \frac{1}{T_2^*} > 0$ is limited by inhomogeneous broadening [112], thus, we can neglect spin flip processes. Of course, the dephasing rate of the GHZ state $\beta > 0$ is related to α, and we will discuss this dependence later. The state of the system, after the wait time T_w is then:

$$\rho_3 = \frac{1}{2}\Big(|0\underline{0}\rangle\langle 0\underline{0}| + |1\underline{1}\rangle\langle 1\underline{1}| + e^{-K\delta T_w i-\beta T_w}|0\underline{0}\rangle\langle 1\underline{1}| + e^{K\delta T_w i-\beta T_w}|1\underline{1}\rangle\langle 0\underline{0}|\Big) \quad . \tag{5.3}$$

To measure the acquired phase $K\delta T_w$, we map the GHZ state onto the central spins by applying a CNOT gate. These spins are then measured by observing the decay of the transverse magnetisation at $M \in \mathbb{N}$ discrete points in time, separated by the sampling time t_s. The observed signal x_m at time mt_s $(m = 0, \ldots, M-1)$ can be modelled as a sum of Gaussian distributed noise b_m and the ideal signal $\hat{x}_m = \langle X + iY\rangle(mt_s)$ [43]

$$x_m = \hat{x}_m + b_m = ce^{K\delta T_w i-\beta T_w}e^{\delta mt_s-\alpha mt_s} + b_m \quad , \tag{5.4}$$

where c is a proportionality factor that depends on the number of molecules in the sample. A simulation of the FID is shown in Fig. 5.2.

A suitable metric for the precision of the measurement is the Cramér-Rao bound (CRB) [43], which essentially offers a lower bound on the uncertainty (standard deviation) σ_{p_ℓ} of an estimated parameter p_ℓ $(\ell = 1, \ldots, P)$:

$$\sigma_{p_\ell} \geq \mathrm{CRB}_{p_\ell} = \sqrt{(F^{-1})_{\ell\ell}} \quad . \tag{5.5}$$

Here, F denotes the Fisher information [192] given by the real part of a complex-

state is referred to as a NOON state because it describes a superposition of N spins up and N spins down.

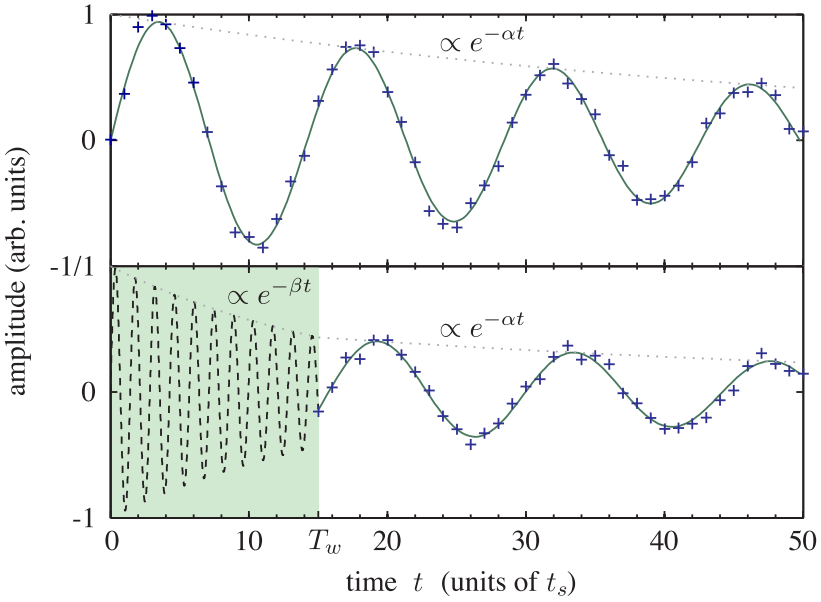

Figure 5.2: Simulation of the free induction decay (FID) of the classical (upper) and quantum strategy (lower); see Eqs. (5.9) and (5.4). The simulated measurement points (crosses) were chosen randomly from a Gaussian distribution with a standard deviation of 0.05. In the classical strategy, we observe uncoupled precessing spins, and the strength of the probe field is given by the oscillation frequency. In the quantum strategy, a GHZ state senses the field for a time T_w without producing a signal, but acquiring phase K times faster than a single spin and dephasing at a rate β. The acquired phase is mapped onto the central spin, and the FID is measured. The strength of the magnetic field can be now estimated from the phase and the oscillation frequency.

valued matrix product

$$F = \frac{1}{\sigma^2}\Re(D^\dagger D) \quad , \tag{5.6}$$

where $D_{ij} = \frac{\partial \hat{x}_i}{\partial p_j}$, and the partial derivatives are evaluated at the parameters that we are going to estimate. In our case, the parameters are c, α and δ. $\sigma = \sigma_r = \sigma_i$ denotes the standard deviation of the real (imaginary) part of the noise. Inverting the 3x3 Fisher information matrix, we obtain:

$$\mathrm{CRB}_{\delta,\mathrm{GHZ}} = \frac{e^{\beta T_w}}{\sqrt{\sum_{m=0}^{M-1}\left(KT_w + mt_s\right)^2 \exp(-2\alpha m t_s)}}\frac{\sigma}{c} \quad . \tag{5.7}$$

Next, we determine the CRB for the classical strategy. Here, we are given $N \cdot K$ identical and uncoupled spins. We obtain the relevant signal by rotating the initial state ρ_0 into the xy-plane with a global Hadamard gate followed by measuring the transverse magnetisation. The resulting density matrix evolves as

$$\rho(t) = \frac{1}{2}\begin{pmatrix} 1 & e^{i\delta t-\alpha t} \\ e^{-i\delta t-\alpha t} & 1 \end{pmatrix} \quad , \tag{5.8}$$

giving rise to a measured signal of the following form

$$x'_m = c' e^{\delta m t_s i - \alpha m t_s} + b'_m \quad . \tag{5.9}$$

Analogously to Eq. (5.7), we obtain the CRB for this signal:

$$\mathrm{CRB}_{\delta,\mathrm{STD}} = \frac{1}{\sqrt{\sum_{m=0}^{M'-1} (m t_s)^2 \exp(-2\alpha m t_s)}} \frac{\sigma'}{c'} \quad . \tag{5.10}$$

This expression is a lower bound on the uncertainty for independent spins against which we shall benchmark the quantum strategy. As the signal-to-noise ratio (SNR) $\frac{c'}{\sigma'}$ scales with the square root of the number of spins in the sample, we get the same scaling behaviour as for the SQL. For a high SNR achieved by a sufficiently large number of molecules N, there exists an efficient estimator which matches the accuracy predicted by the CRB [35]. Hence, we can directly use Eqs. (5.7) and (5.10) to compare the two strategies.

5.3 Observation of the entire free induction decay

First, we need to specify a fair comparison with the same resource allocation for both strategies. For conventional quantum metrology with projective measurements, the challenging question of a fair resource comparison has recently been addressed in Ref. [210]. In the present case of ensemble quantum metrology, we will, at first, allow both strategies to observe the entire FID while consuming the von Neumann entropy of $1 \cdot N$ spins. As we have defined it, the quantum strategy consumes one spin per molecule (the central spin A) in the measurement, and all other spins remain pure. This implies that we must also only measure $1 \cdot N$ spins instead of $K \cdot N$ spins for the classical strategy, meaning that the SNRs of both measurements are equal $\frac{c'}{\sigma'} = \frac{c}{\sigma}$.

At first sight, this way of counting resources may look biased towards the quantum case, as we do not seem to take the satellite spins into account. Nonetheless, our comparison is fair: The $K-1$ satellite spins act as an antenna to pick up phase more rapidly, yet they are not 'consumed' (this is a direct consequence of the dephasing model of decoherence). After the quantum strategy is complete, the central spin is measured (its polarisation is lost), but all satellite spins are back in the pure state $|\underline{0}\rangle$ and could be recycled to obtain a further parameter estimate. The accuracy of such an estimate, made using any sensible protocol on these remaining $(K-1)N$ spins, can be no worse than that obtained using the standard strategy. This observation validates the classical resource count stated in the previous paragraph.

The ratio of Eq. (5.10) and Eq. (5.7) can be approximated by an integral

expression (assuming the sampling rate resolves the decay, i.e. $t_s \ll T_2^*$):

$$R_\infty := \frac{\mathrm{CRB}_{\delta,\mathrm{STD}}}{\mathrm{CRB}_{\delta,\mathrm{GHZ}}} \approx \sqrt{\frac{\int_0^\infty (KT_w + t)^2 \exp(-2\alpha t)\, dt}{e^{2\beta T_w} \int_0^\infty t^2 \exp(-2\alpha t)\, dt}} \tag{5.11}$$

$$= e^{-\beta T_w} \sqrt{1 + 2K\alpha T_w (1 + K\alpha T_w)} \quad . \tag{5.12}$$

Whenever $R_\infty > 1$, the quantum strategy outperforms the classical strategy with respect to the precision of the parameter estimation.

So far we have not yet specified how the dephasing rate β of the GHZ state relates to the dephasing rate α of a single spin, and now, we will discuss a number of different decoherence models for the GHZ state.

First, we consider $\beta = \alpha$, implying that the GHZ state does not decohere faster than a single spin; this is expected for a given macroscopic magnetic field inhomogeneity. In this case, there is, for any $K > 1$, a wait time T_w, for which the quantum strategy surpasses the classical one. Conversely, completely correlated or collective noise over each molecule has the most aggressive effect on the GHZ state [173, 148]. Here, the noise can be described with a single Lindblad operator $\sum_{j=1}^K \sigma_z$ and $\beta = K^2\alpha$, while, for uncorrelated noise $\beta = K\alpha$ [10]. In general, we consider a power-law dependence of β on α, i.e. $\beta = K^p\alpha$, where $0 \leq p \leq 2$. In recent experiments the decoherence rates for highly correlated solid-state spin states were obtained experimentally [102, 103], revealing $p \approx 1/2$. The authors attributed this to non-Markovian correlated noise. A significantly smaller value for p was found in Ref. [178], where the T_2^* time of a single spin was determined to be 0.37 s and that of a 13-particle GHZ state to be 0.28 s, which can be interpreted as a factor of $p \approx 0.11$.

The performance of the quantum sensor depends critically on the value of p. One can easily check that, for $1 \leq p \leq 2$, $R_\infty < 1$ for any $T_w > 0$, and $R_\infty = 1$ only for $T_w = 0$. Therefore, we conclude that the precision of the quantum

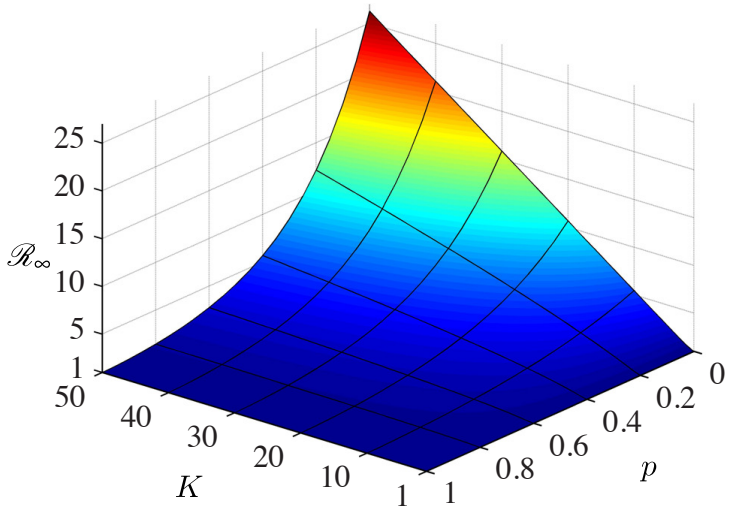

Figure 5.3: The maximal $\mathcal{R}_\infty$ for a given K as a function of K and p, where p is given by $\beta = K^p\alpha$. $\mathcal{R}_\infty > 1$ implies that the quantum strategy outperforms the standard strategy.

method never outperforms the precision of the standard method, if $1 \leq p \leq 2$. In contrast, for $p < 1$, there is an optimal non-zero, K-dependent, wait time T_w for which $R_\infty > 1$. Specifically, calculating the optimal waiting time T_w that gives rise to a maximum of $\mathcal{R}_\infty$ (for a given K and $p < 1$) yields

$$\mathcal{R}_\infty = \max_{T_w} R_\infty = \frac{K^{\frac{1}{2}-p}\sqrt{K + \sqrt{K^2 - K^{2p}}}}{\exp\left[\frac{1}{2}\left(1 - K^{p-1} + \sqrt{1 - K^{2p-2}}\right)\right]} \quad , \tag{5.13}$$

which scales like $\frac{\sqrt{2}}{e}K^{1-p}$ to leading order (see Fig. 5.3). Therefore, the standard strategy can indeed be beaten with a quantum strategy if the decoherence of the GHZ state is not too aggressive, i.e. for $p < 1$. Moreover, we see that, under this condition, the precision of the estimation improves monotonically as K increases. As a special case, we consider $p = 0$, here, $\mathcal{R}_\infty$ increases linearly in K; this means that the uncertainty of the parameter estimation with the optimised quantum strategy scales as $1/K$, analogously to the Heisenberg limit.

5.4 Restricted process time

So far, we have neglected time as a resource, focusing instead on system size and the consumption of initial polarisation (maximising the von Neumann entropy of one spin per molecule). It is interesting to extend our analysis to a restricted process time, meaning only a part of the FID can be observed. Since the first part of the FID contains most information, this would enable a 'better' sensor by a series of repeated runs in a given time window T_{tot} if one had the ability to instantly reset the spins to their initial state after time T, for example, with an optical switch. For a first comparison, both strategies are allocated the same amount of time $T = M' t_s < \infty$ implying $M = (T - T_w)/t_s$, where M/M' are the number of measurements in the quantum/standard strategy [see Eq. (5.7)/(5.10)]. As before, we compare measurements of the same number of spins, i.e. $\frac{c'}{\sigma'} = \frac{c}{\sigma}$, and the ratio of the CRBs can again be approximated by an integral expression:

$$R_T := \frac{\mathrm{CRB}_{\delta,\mathrm{STD}}}{\mathrm{CRB}_{\delta,\mathrm{GHZ}}} \approx e^{-\beta T_w} \sqrt{\frac{\int_0^{T-T_w} (KT_w + t)^2 \exp(-2\alpha t)}{\int_0^T t^2 \exp(-2\alpha t)}} \quad . \tag{5.14}$$

We have not been able to find an analytic expression for the maximal ratio $\mathcal{R}_T := \max_{T_w} R_T$, and the optimisation over T_w was done numerically in Fig. 5.4. However, one can show that $\lim_{K\to\infty} \mathcal{R}_T|_{p<1} = \infty$ and $\lim_{K\to\infty} \mathcal{R}_T|_{1<p\leq 2} = 1$. This implies that for any $p \in (1, 2]$ there is a specific K_p for which the quantum strategy assumes a minimal uncertainty for the parameter estimation, while any other size of the sensor produces a higher uncertainty (note that $\mathrm{CRB}_{\delta,\mathrm{STD}}$ is independent of p and K). When $p < 1$ the uncertainty in the parameter estimation decreases monotonically with increasing K. It is worth pointing out that in contrast to the time-independent comparison, the quantum strategy now also beats the standard strategy in the region $1 < p \leq 2$. Moreover for $p < 1$ the attained ratios are higher than in the first comparison and these become higher for

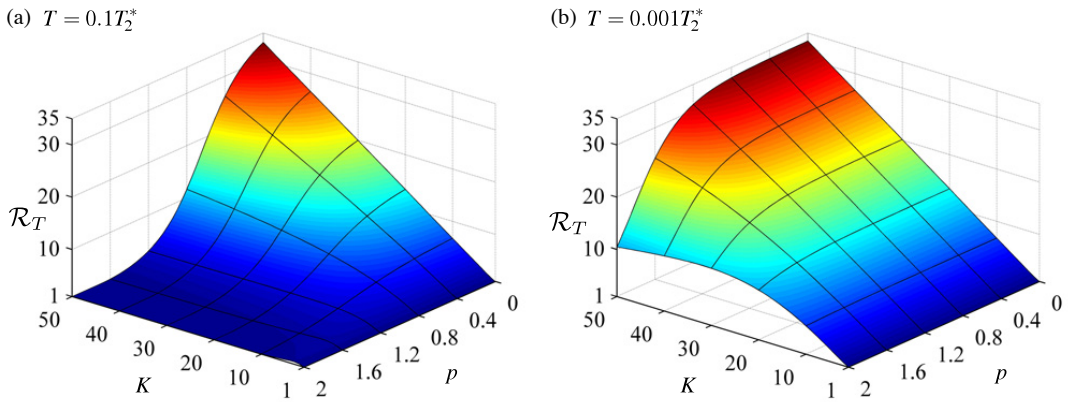

Figure 5.4: The maximal ratio $\mathcal{R}_T$ as a function of K and p. The total time available for the first/second comparison is $T = 0.1T_2^*$ and $T = 0.001T_2^*$.

smaller T. In summary, adding time to the resource count thus always favours the quantum strategy over the classical strategy.

We can improve both strategies by also optimising over the duration T of each cycle. For this purpose we consider the uncertainty of the parameter estimation of a series of T_{tot}/T repetitions. It is given by

$$\frac{1}{\sqrt{T_{\text{tot}}/T}}\text{CRB}_{\text{STD/GHZ}} =: \frac{1}{\sqrt{T_{\text{tot}}}}S_{\text{STD/GHZ}} \quad . \tag{5.15}$$

Obviously one would choose the length of a time slice T optimally, i.e. in such a way that the uncertainty per $\sqrt{\text{Hz}}$, i.e. $S_{\text{STD/GHZ}}$ is minimal. For the classical strategy, we find by using the integral approximation for the CRB from before and numerical optimisation that

$$S^*_{\text{STD}} := \min_T S_{\text{STD}} = \kappa\sqrt{t_s}\alpha^{3/2}\frac{\sigma'}{c'} \quad , \tag{5.16}$$

with $\kappa \approx 3.21\ \sqrt{\text{s}}$, which is attained for the optimal time $T^* \approx 1.69T_2^*$.

In the quantum strategy, S_{GHZ} also depends on T_w, the amount of time for which the spins are in the GHZ state. In contrast to the classical strategy, the minimum here depends on the system parameters K and p. We have not been

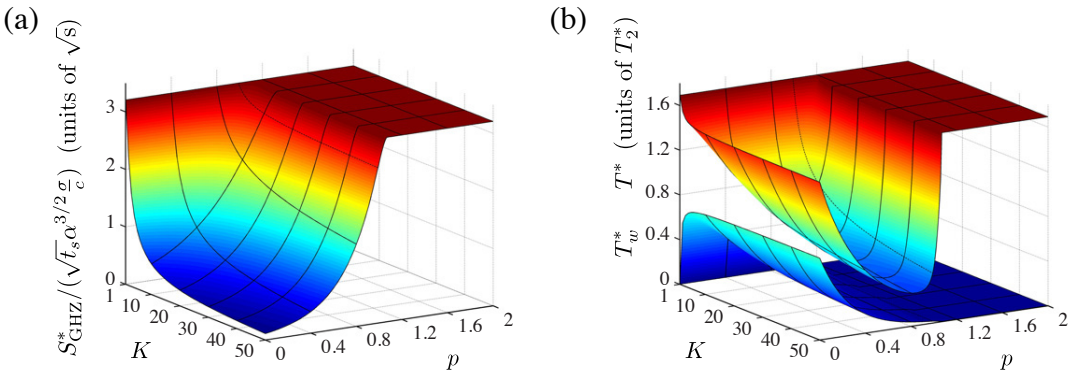

Figure 5.5: (a) Minimal (optimised over T and T_w) uncertainty of the parameter estimation for the quantum strategy per $\sqrt{\mathrm{Hz}}$, i.e. $S^*_{\mathrm{GHZ}}/(\sqrt{t_s}\alpha^{3/2}\frac{\sigma}{c})$ in dependence of K and p. (b) The corresponding optimal times T^* (upper surface) and T_w^* (lower surface) as units of T_2^* for which the minimum in (a) is attained in dependence of K and p.

able to find an analytic expression for $S^*_{\mathrm{GHZ}} := \min_{T,T_w} S_{\mathrm{GHZ}}$; and, we therefore performed a numerical optimisation with the results displayed in Fig. 5.5. As in our first comparison, we assume that the SNRs for both strategies are equal. If aggressive noise is affecting the GHZ state, the optimal quantum strategy is basically the optimal standard strategy, as $T^* \to 1.69T_2^*$ and $T_w^* \to 0$, when $p \to 2$. For small p and large K, however, the quantum strategy significantly outperforms the standard strategy. Again, the quantum strategy can now beat the optimised standard strategy for values p that are slightly larger than 1.

5.5 Summary and discussion

In conclusion, we have presented a framework for analysing the performance of quantum metrology using spin ensembles. This framework incorporates the special nature of the non-projective measurement process, and leads one to consider the polarisation change during the protocol as kind of a resource consumption. We find that the decoherence model plays a defining role in this framework, and we have identified the parameter regime where a certain quantum strategy can

beat the standard classical strategy.

We have seen in this chapter that the framework presented here is based on the fact that in NMR/EPR the measurement does not usually alter the system, as there are so many spins in a typical sample. However, it would be very interesting to see how the results in this chapter change once there is a back-action onto the system induced by the measurement. Such an analysis is an open question and would require a generalisation of the free induction decay as a first step.

Bibliography

[1] A. Abragam. *Principles of Nuclear Magnetism*. International Series of Monographs on Physics. Oxford University Press, 1983.

[2] V. M. Acosta, E. Bauch, A. Jarmola, L. J. Zipp, M. P. Ledbetter and D. Budker. Broadband magnetometry by infrared-absorption detection of nitrogen-vacancy ensembles in diamond. *Applied Physics Letters*, 97(17):174104, 2010. doi:10.1063/1.3507884.

[3] V. M. Acosta, E. Bauch, M. P. Ledbetter, C. Santori, K.-M. C. Fu, P. E. Barclay, R. G. Beausoleil, H. Linget, J. F. Roch, F. Treussart, S. Chemerisov, W. Gawlik and D. Budker. Diamonds with a high density of nitrogen-vacancy centers for magnetometry applications. *Physical Review B*, 80(11):115202, 2009. doi:10.1103/PhysRevB.80.115202.

[4] L. M. Adleman, J. Demarrais and M.-D. A. Huang. Quantum computability. *SIAM Journal on Computing*, 26(5):1524–1540, 1997. doi:10.1137/S0097539795293639.

[5] I. Afek, O. Ambar and Y. Silberberg. High-NOON states by mixing quantum and classical light. *Science*, 328(5980):879–881, 2010. doi:10.1126/science.1188172.

[6] D. Aharonov and I. Arad. The BQP-hardness of approximating the Jones polynomial. 2006. arXiv:quant-ph/0605181.

[7] D. Aharonov and I. Arad. The BQP-hardness of approximating the Jones

polynomial. *New Journal of Physics*, 13(3):035019, 2011. doi:10.1088/1367-2630/13/3/035019.

[8] D. Aharonov, V. Jones and Z. Landau. A polynomial quantum algorithm for approximating the Jones polynomial. In *Proceedings of the 38th Annual ACM Symposium on Theory of Computing*, STOC '06, pages 427–436, New York, 2006. ACM. doi:10.1145/1132516.1132579.

[9] T. Almeida Murphy, T. Pawlik, A. Weidinger, M. Höhne, R. Alcala and J.-M. Spaeth. Observation of atomlike nitrogen in nitrogen-implanted solid C_{60}. *Physical Review Letters*, 77(6):1075–1078, 1996. doi:10.1103/PhysRevLett.77.1075.

[10] L. Aolita, R. Chaves, D. Cavalcanti, A. Acín and L. Davidovich. Scaling laws for the decay of multiqubit entanglement. *Physical Review Letters*, 100(8):080501, 2008. doi:10.1103/PhysRevLett.100.080501.

[11] S. Ashhab, A. O. Niskanen, K. Harrabi, Y. Nakamura, T. Picot, P. C. de Groot, C. J. P. M. Harmans, J. E. Mooij and F. Nori. Interqubit coupling mediated by a high-excitation-energy quantum object. *Physical Review B*, 77(1):014510, 2008. doi:10.1103/PhysRevB.77.014510.

[12] G. Balasubramanian, I. Y. Chan, R. Kolesov, M. Al-Hmoud, J. Tisler, C. Shin, C. Kim, A. Wojcik, P. R. Hemmer, A. Krueger, T. Hanke, A. Leitenstorfer, R. Bratschitsch, F. Jelezko and J. Wrachtrup. Nanoscale imaging magnetometry with diamond spins under ambient conditions. *Nature*, 455(7213):648–651, 2008. doi:10.1038/nature07278.

[13] G. Balasubramanian, P. Neumann, D. Twitchen, M. Markham, R. Kolesov, N. Mizuochi, J. Isoya, J. Achard, J. Beck, J. Tissler, V. Jacques, P. R. Hemmer, F. Jelezko and J. Wrachtrup. Ultralong spin coherence time in isotopically engineered diamond. *Nature Materials*, 8:383–387, 2009.

doi:10.1038/nmat2420.

[14] A. Barenco, C. H. Bennett, R. Cleve, D. P. DiVincenzo, N. Margolus, P. Shor, T. Sleator, J. A. Smolin and H. Weinfurter. Elementary gates for quantum computation. *Physical Review A*, 52:3457–3467, 1995. doi:10.1103/PhysRevA.52.3457.

[15] A. B. Barnes, G. De Paëpe, P. C. A. van der Wel, K.-N. Hu, C.-G. Joo, V. S. Bajaj, M. L. Mak-Jurkauskas, J. R. Sirigiri, J. Herzfeld, R. J. Temkin and R. G. Griffin. High-field dynamic nuclear polarization for solid and solution biological NMR. *Applied Magnetic Resonance*, 34(3):237–263, 2008. doi:10.1007/s00723-008-0129-1.

[16] S. D. Barrett and P. Kok. Efficient high-fidelity quantum computation using matter qubits and linear optics. *Physical Review A*, 71(6):060310, 2005. doi:10.1103/PhysRevA.71.060310.

[17] S. C. Benjamin, A. Ardavan, G. A. D. Briggs, D. A. Britz, D. Gunlycke, J. Jefferson, M. A. G. Jones, D. F. Leigh, B. W. Lovett, A. N. Khlobystov, S. A. Lyon, J. J. L. Morton, K. Porfyrakis, M. R. Sambrook and A. M. Tyryshkin. Towards a fullerene-based quantum computer. *Journal of Physics: Condensed Matter*, 18(21):S867–S883, 2006. doi:10.1088/0953-8984/18/21/S12.

[18] S. C. Benjamin and S. Bose. Quantum computing with an always-on Heisenberg interaction. *Physical Review Letters*, 90(24):247901, 2003. doi:10.1103/PhysRevLett.90.247901.

[19] S. C. Benjamin, D. E. Browne, J. Fitzsimons and J. J. L. Morton. Brokered graph-state quantum computation. *New Journal of Physics*, 8(8):141, 2006. doi:10.1088/1367-2630/8/8/141.

[20] S. C. Benjamin, B. W. Lovett and J. H. Reina. Optical quantum compu-

tation with perpetually coupled spins. *Physical Review A*, 70(6):060305, 2004. doi:10.1103/PhysRevA.70.060305.

[21] C. H. Bennett. Logical reversibility of computation. *IBM Journal of Research and Development*, 17(6):525–532, 1973. doi:10.1147/rd.176.0525.

[22] C. H. Bennett, E. Bernstein, G. Brassard and U. Vazirani. Strengths and weaknesses of quantum computing. *SIAM Journal on Computing*, 26(5):1510–1523, 1997. doi:10.1137/S0097539796300933.

[23] C. H. Bennett, H. J. Bernstein, S. Popescu and B. Schumacher. Concentrating partial entanglement by local operations. *Physical Review A*, 53(4):2046–2052, 1996. doi:10.1103/PhysRevA.53.2046.

[24] C. H. Bennett, D. P. DiVincenzo, J. A. Smolin and W. K. Wootters. Mixed-state entanglement and quantum error correction. *Physical Review A*, 54(5):3824–3851, 1996. doi:10.1103/PhysRevA.54.3824.

[25] V. Bergholm, J. J. Vartiainen, M. Möttönen and M. M. Salomaa. Quantum circuits with uniformly controlled one-qubit gates. *Physical Review A*, 71:052330, 2005. doi:10.1103/PhysRevA.71.052330.

[26] E. Bernstein and U. Vazirani. Quantum complexity theory. In *Proceedings of the 25th Annual ACM Symposium on Theory of Computing*, STOC '93, pages 11–20, New York, 1993. ACM. doi:10.1145/167088.167097.

[27] M. A. Bernstein, K. F. King and X. J. Zhou. *Handbook of MRI Pulse Sequences*. Elsevier, 2004.

[28] A. Beveratos, R. Brouri, T. Gacoin, A. Villing, J.-P. Poizat and P. Grangier. Single photon quantum cryptography. *Physical Review Letters*, 89(18):187901, 2002. doi:10.1103/PhysRevLett.89.187901.

[29] B. B. Blinov, D. L. Moehring, L.-M. Duan and C. Monroe. Observation of

entanglement between a single trapped atom and a single photon. *Nature*, 428:153–157, 2004. doi:10.1038/nature02377.

[30] G. Boero, M. Demierre, P.-A. Besse and R. S. Popovic. Micro-Hall devices: performance, technologies and applications. *Sensors and Actuators A: Physical*, 106(1-3):314 – 320, 2003. doi:10.1016/S0924-4247(03)00192-4.

[31] S. Bosi, T. D. Ros, G. Spalluto and M. Prato. Fullerene derivatives: an attractive tool for biological applications. *European Journal of Medicinal Chemistry*, 38(11-12):913–923, 2003. doi:10.1016/j.ejmech.2003.09.005.

[32] D. Bouwmeester and A. Ekert. *The Physics of Quantum Information*. Springer, 2001.

[33] C. Bradac, T. Gaebel, N. Naidoo, M. J. Sellars, J. Twamley, L. J. Brown, A. S. Barnard, T. Plakhotnik, A. V. Zvyagin and J. R. Rabeau. Observation and control of blinking nitrogen-vacancy centres in discrete nanodiamonds. *Nature Nanotechnology*, 5:345–349, 2010. doi:10.1038/nnano.2010.56.

[34] S. L. Braunstein and C. M. Caves. Statistical distance and the geometry of quantum states. *Physical Review Letters*, 72(22):3439–3443, 1994. doi:10.1103/PhysRevLett.72.3439.

[35] Y. Bresler and A. Macovski. Exact maximum likelihood parameter estimation of superimposed exponential signals in noise. *Acoustics, Speech and Signal Processing, IEEE Transactions on*, 34(5):1081–1089, 1986. doi:10.1109/TASSP.1986.1164949.

[36] H. P. Breuer and F. Petruccione. *The Theory of Open Quantum Systems*. Oxford University Press, 2002.

[37] R. M. Brown, Y. Ito, J. H. Warner, A. Ardavan, H. Shinohara, G. A. D. Briggs and J. J. L. Morton. Electron spin coherence in metallofullerenes: Y, Sc, and La@C_{82}. *Physical Review B*, 82(3):033410, 2010. doi:10.1103/PhysRevB.82.033410.

[38] D. Bruß, J. I. Cirac, P. Horodecki, F. Hulpke, B. Kraus, M. Lewenstein and A. Sanpera. Reflections upon separability and distillability. *Journal of Modern Optics*, 49(8):1399–1418, 2002. doi:10.1080/09500340110105975.

[39] D. Bruß and G. Leuchs, editors. *Lectures on Quantum Information*. Wiley-VCH, 2007.

[40] J. Cai, G. G. Guerreschi and H. J. Briegel. Quantum control and entanglement in a chemical compass. *Physical Review Letters*, 104(22):220502, 2010. doi:10.1103/PhysRevLett.104.220502.

[41] E. T. Campbell and S. C. Benjamin. Measurement-based entanglement under conditions of extreme photon loss. *Physical Review Letters*, 101(13):130502, 2008. doi:10.1103/PhysRevLett.101.130502.

[42] H. Carmichael. *An Open Systems Approach to Quantum Optics: Lectures Presented at the Universite Libre De Bruxelles October 28 to November 4, 1991*. Lecture Notes in Physics New Series M. Springer, 1993.

[43] S. Cavassila, S. Deval, C. Huegen, D. van Ormondt and D. Graveron-Demilly. Cramér-Rao bound expressions for parametric estimation of overlapping peaks: Influence of prior knowledge. *Journal of Magnetic Resonance*, 143(2):311–320, 2000. doi:10.1006/jmre.1999.2002.

[44] Y. Chai, T. Guo, C. Jin, R. E. Haufler, L. P. F. Chibante, J. Fure, L. Wang, J. M. Alford and R. E. Smalley. Fullerenes with metals inside. *The Journal of Physical Chemistry*, 95(20):7564–7568, 1991. doi:

10.1021/j100173a002.

[45] D. E. Chang, A. S. Sørensen, P. R. Hemmer and M. D. Lukin. Quantum optics with surface plasmons. *Physical Review Letters*, 97(5):053002, 2006. doi:10.1103/PhysRevLett.97.053002.

[46] A. Chi-Chih Yao. Quantum circuit complexity. In *Proceedings of the 34th Annual Symposium on Foundations of Computer Science*, pages 352–361, 1993. doi:10.1109/SFCS.1993.366852.

[47] G. Christou, D. Gatteschi, D. N. Hendrickson and R. Sessoli. Single-molecule magnets. *MRS Bulletin*, 25(11):66–71, 2000. doi:10.1557/mrs2000.226.

[48] J. I. Cirac, A. K. Ekert, S. F. Huelga and C. Macchiavello. Distributed quantum computation over noisy channels. *Physical Review A*, 59(6):4249–4254, 1999. doi:10.1103/PhysRevA.59.4249.

[49] V. L. Colvin. The potential environmental impact of engineered nanomaterials. *Nature Biotechnology*, 21:1166–1170, 2003. doi:10.1038/nbt875.

[50] S. A. Cook. The complexity of theorem-proving procedures. In *Proceedings of the 3rd Annual ACM Symposium on Theory of Computing*, STOC '71, pages 151–158, New York, 1971. ACM. doi:10.1145/800157.805047.

[51] H. Cramér. *Mathematical Methods of Statistics*. Princeton University Press, 1946.

[52] C. Degen. Nanoscale magnetometry: Microscopy with single spins. *Nature Nanotechnology*, 3:643, 2008. doi:10.1038/nnano.2008.328.

[53] C. L. Degen. Scanning magnetic field microscope with a diamond single-spin sensor. *Applied Physics Letters*, 92:243111, 2008. doi:10.1063/1.2943282.

[54] C. L. Degen, M. Poggio, H. J. Mamin, C. T. Rettner and D. Rugar. Nanoscale magnetic resonance imaging. *Proceedings of the National Academy of Sciences*, 106:1313, 2009. doi:10.1073/pnas.0812068106.

[55] D. Deutsch. Quantum theory, the Church-Turing principle and the universal quantum computer. *Proceedings of the Royal Society A*, 400(1818):97–117, 1985. doi:10.1098/rspa.1985.0070.

[56] D. Deutsch and R. Jozsa. Rapid solution of problems by quantum computation. *Proceedings of the Royal Society A*, 439(1907):553–558, 1992. doi:10.1098/rspa.1992.0167.

[57] D. Dieks. Communication by EPR devices. *Physics Letters A*, 92(6):271–272, 1982. doi:10.1016/0375-9601(82)90084-6.

[58] F. Dolde, H. Fedder, M. W. Doherty, T. Nobauer, F. Rempp, G. Balasubramanian, T. Wolf, F. Reinhard, L. C. L. Hollenberg, F. Jelezko and J. Wrachtrup. Electric-field sensing using single diamond spins. *Nature Physics*, 7:459–463, 2011. doi:10.1038/nphys1969.

[59] M. C. J. M. Donckers, A. M. Schwencke, E. J. J. Groenen and J. Schmidt. An electron–nuclear double resonance study of the lowest triplet state of pyrazine. *Journal of Chemical Physics*, 97(1):110–117, 1992. doi:10.1063/1.463609.

[60] M. V. G. Dutt, L. Childress, L. Jiang, E. Togan, J. Maze, F. Jelezko, A. S. Zibrov, P. R. Hemmer and M. D. Lukin. Quantum register based on individual electronic and nuclear spin qubits in diamond. *Science*, 316:1312, 2007. doi:10.1126/science.1139831.

[61] A. Einstein, B. Podolsky and N. Rosen. Can quantum-mechanical description of physical reality be considered complete? *Physical Reviews*, 47(10):777–780, 1935. doi:10.1103/PhysRev.47.777.

[62] R. J. Epstein, F. M. Mendoza, Y. K. Kato and D. D. Awschalom. Anisotropic interactions of a single spin and dark-spin spectroscopy in diamond. *Nature Physics*, 1(2):94–98, 2005. doi:10.1038/nphys141.

[63] D. Estève, J.-M. Raimond and J. Dalibard, editors. *Quantum Entanglement and Information Processing: Lecture Notes of the Les Houches Summer School 2003 (Les Houches)*. Elsevier Science & Technology, 2004.

[64] P. Facchi, S. Tasaki, S. Pascazio, H. Nakazato, A. Tokuse and D. A. Lidar. Control of decoherence: Analysis and comparison of three different strategies. *Physical Review A*, 71(2):022302, 2005. doi:10.1103/PhysRevA.71.022302.

[65] R. P. Feynman. Simulating physics with computers. *International Journal of Theoretical Physics*, 21:467–488, 1982. doi:10.1007/BF02650179.

[66] V. Filidou et al. (manuscript in preparation).

[67] R. A. Fisher. Theory of statistical estimation. *Mathematical Proceedings of the Cambridge Philosophical Society*, 22(5):700–725, 1925. doi:10.1017/S0305004100009580.

[68] E. Fredkin and T. Toffoli. Conservative Logic. *International Journal of Theoretical Physics*, 21(3/4):219–253, 1982. doi:10.1007/BF01857724.

[69] M. H. Freedman, A. Kitaev and Z. Wang. Simulation of topological field theories by quantum computers. *Communications in Mathematical Physics*, 227(3):587–603, 2002. doi:10.1007/s002200200635.

[70] M. H. Freedman, M. Larsen and Z. Wang. A modular functor which is universal for quantum computation. *Communications in Mathematical Physics*, 227(3):605–622, 2002. doi:10.1007/s002200200645.

[71] T. Gaebel, M. Domhan, I. Popa, C. Wittmann, P. Neumann, F. Jelezko, J. R. Rabeau, N. Stavrias, A. D. Greentree, S. Prawer, J. Meijer, J. Twam-

ley, P. R. Hemmer and J. Wrachtrup. Room-temperature coherent coupling of single spins in diamond. *Nature Physics*, 2:408–413, 2006. doi:10.1038/nphys318.

[72] C. W. Gardiner and P. Zoller. *Quantum Noise: A Handbook of Markovian and Non-Markovian Quantum Stochastic Methods With Applications to Quantum Optics*. Springer, 2nd edition, 2000.

[73] B. W. Gardner, J. C. Wynn, P. G. Björnsson, E. W. J. Straver, K. A. Moler, J. R. Kirtley and M. B. Ketchen. Scanning superconducting quantum interference device susceptometry. *Review of Scientific Instruments*, 72:2361, 2001. doi:10.1063/1.1364668.

[74] E. M. Gauger, S. C. Benjamin, A. Nazir and B. W. Lovett. High-fidelity all-optical control of quantum dot spins: Detailed study of the adiabatic approach. *Physical Review B*, 77(11):115322, 2008. doi:10.1103/PhysRevB.77.115322.

[75] E. M. Gauger, A. Nazir, S. C. Benjamin, T. M. Stace and B. W. Lovett. Robust adiabatic approach to optical spin entangling in coupled quantum dots. *New Journal of Physics*, 10(7):073016, 2008. doi:10.1088/1367-2630/10/7/073016.

[76] E. M. Gauger, E. Rieper, J. J. L. Morton, S. C. Benjamin and V. Vedral. Sustained quantum coherence and entanglement in the avian compass. *Physical Review Letters*, 106(4):040503, 2011. doi:10.1103/PhysRevLett.106.040503.

[77] E. M. Gauger, P. P. Rohde, A. M. Stoneham and B. W. Lovett. Strategies for entangling remote spins with unequal coupling to an optically active mediator. *New Journal of Physics*, 10:073027, 2008. doi:10.1088/1367-2630/10/7/073027.

[78] V. Giovannetti, S. Lloyd and L. Maccone. Quantum-enhanced measurements: Beating the standard quantum limit. *Science*, 306:1330–1336, 2004. doi:10.1126/science.1104149.

[79] V. Giovannetti, S. Lloyd and L. Maccone. Quantum metrology. *Physical Review Letters*, 96(1):010401, 2006. doi:10.1103/PhysRevLett.96.010401.

[80] M. S. Grinolds, P. Maletinsky, S. Hong, M. D. Lukin, R. L. Walsworth and A. Yacoby. Quantum control of proximal spins using nanoscale magnetic resonance imaging. *Nature Physics*, 7(9):687–692, 2011. doi:10.1038/nphys1999.

[81] B. Grotz, J. Beck, P. Neumann, B. Naydenov, R. Reuter, F. Reinhard, F. Jelezko, J. Wrachtrup, D. Schweinfurth, B. Sarkar and P. Hemmer. Sensing external spins with nitrogen-vacancy diamond. *New Journal of Physics*, 13(5):055004, 2011. doi:10.1088/1367-2630/13/5/055004.

[82] L. K. Grover. A fast quantum mechanical algorithm for database search. In *Proceedings of the 28th Annual ACM symposium on Theory of Computing*, STOC '96, pages 212–219, New York, 1996. ACM. doi:10.1145/237814.237866.

[83] A. Gruber, A. Drabenstedt, C. Tietz, L. Fleury, J. Wrachtrup and C. von Borczyskowski. Scanning confocal optical microscopy and magnetic resonance on single defect centers. *Science*, 276(5321):2012–2014, 1997. doi:10.1126/science.276.5321.2012.

[84] O. Gühne, P. Hyllus, D. Bruß, A. Ekert, M. Lewenstein, C. Macchiavello and A. Sanpera. Detection of entanglement with few local measurements. *Physical Review A*, 66(6):062305, 2002. doi:10.1103/PhysRevA.66.062305.

[85] O. Gühne, P. Hyllus, D. Bruss, A. Ekert, M. Lewenstein, C. Macchiavello and A. Sanpera. Experimental detection of entanglement via witness operators and local measurements. *Journal of Modern Optics*, 50(6 & 7):1079–1102, 2003. doi:10.1080/09500340308234554.

[86] E. Hagley, X. Maître, G. Nogues, C. Wunderlich, M. Brune, J. M. Raimond and S. Haroche. Generation of Einstein-Podolsky-Rosen pairs of atoms. *Physical Review Letters*, 79(1):1–5, 1997. doi:10.1103/PhysRevLett.79.1.

[87] J. Harrison, M. J. Sellars and N. B. Manson. Measurement of the optically induced spin polarisation of N-V centres in diamond. *Diamond and Related Materials*, 15(4-8):586–588, 2006. Diamond 2005. doi:10.1016/j.diamond.2005.12.027.

[88] M. Herz, F. J. Giessibl and J. Mannhart. Probing the shape of atoms in real space. *Physical Review B*, 68(4):045301, 2003. doi:10.1103/PhysRevB.68.045301.

[89] K. Hirahara, K. Suenaga, S. Bandow, H. Kato, T. Okazaki, H. Shinohara and S. Iijima. One-dimensional metallofullerene crystal generated inside single-walled carbon nanotubes. *Physical Review Letters*, 85(25):5384–5387, 2000. doi:10.1103/PhysRevLett.85.5384.

[90] M. E. Huber, N. C. Koshnick, H. Bluhm, L. J. Archuleta, T. Azua, P. G. Björnsson, B. W. Gardner, S. T. Halloran, E. A. Lucero and K. A. Moler. Gradiometric micro-SQUID susceptometer for scanning measurements of mesoscopic samples. *Review of Scientific Instruments*, 79:053704, 2008. doi:10.1063/1.2932341.

[91] S. F. Huelga, C. Macchiavello, T. Pellizzari, A. K. Ekert, M. B. Plenio and J. I. Cirac. Improvement of frequency standards with quantum

entanglement. *Physical Review Letters*, 79(20):3865–3868, 1997. doi:10.1103/PhysRevLett.79.3865.

[92] F. Jelezko, T. Gaebel, I. Popa, A. Gruber and J. Wrachtrup. Observation of coherent oscillations in a single electron spin. *Physical Review Letters*, 92(7):076401, 2004. doi:10.1103/PhysRevLett.92.076401.

[93] G. Jeschke and Y. Polyhach. Distance measurements on spin-labelled biomacromolecules by pulsed electron paramagnetic resonance. *Physical Chemistry Chemical Physics*, 9(16):1895–1910, 2007. doi:10.1039/B614920K.

[94] J. A. Jones, S. D. Karlen, J. Fitzsimons, A. Ardavan, S. C. Benjamin, G. A. D. Briggs and J. J. L. Morton. Magnetic field sensing beyond the standard quantum limit using 10-spin NOON states. *Science*, 324(5931):1166–1168, 2009. doi:10.1126/science.1170730.

[95] R. Jozsa and A. Miyake. Matchgates and classical simulation of quantum circuits. *Proceedings of the Royal Society A*, 464(2100):3089–3106, 2008. doi:10.1098/rspa.2008.0189.

[96] R. M. Karp. Reducibility among combinatorial problems. In R. E. Miller and J. W. Thatcher, editors, *Complexity of Computer Computations, Proc. Sympos. IBM Thomas J. Watson Res. Center*, pages 85–103, 1972. URL: http://www.cs.berkeley.edu/~luca/cs172/karp.pdf.

[97] T. A. Kennedy, J. S. Colton, J. E. Butler, R. C. Linares and P. J. Doering. Long coherence times at 300 K for nitrogen-vacancy center spins in diamond grown by chemical vapor deposition. *Applied Physics Letters*, 83(20):4190–4192, 2003. doi:10.1063/1.1626791.

[98] J. R. Kirtley, M. B. Ketchen, K. G. Stawiasz, J. Z. Sun, W. J. Gallagher, S. H. Blanton and S. J. Wind. High-resolution scanning squid microscope.

Applied Physics Letters, 66:1138, 1995. doi:10.1063/1.113838.

[99] A. Kitaev. Quantum measurements and the Abelian stabilizer problem. 1995. arXiv:quant-ph/9511026.

[100] T. Klove. *Codes for Error Detection*. World Scientific Publishing Company, 2007.

[101] P. Kok and B. W. Lovett. *Introduction to Optical Quantum Information Processing*. Cambridge University Press, 2010.

[102] H. G. Krojanski and D. Suter. Scaling of decoherence in wide NMR quantum registers. *Physical Review Letters*, 93(9):090501, 2004. doi:10.1103/PhysRevLett.93.090501.

[103] H. G. Krojanski and D. Suter. Reduced decoherence in large quantum registers. *Physical Review Letters*, 97(15):150503, 2006. doi:10.1103/PhysRevLett.97.150503.

[104] H. W. Kroto, J. R. Heath, S. C. O'Brien, R. F. Curl and R. E. Smalley. C_{60}: Buckminsterfullerene. *Nature*, 318:162–163, 1985. doi:10.1038/318162a0.

[105] W. Krätschmer, L. D. Lamb, K. Fostiripoulos and D. R. Huffman. Solid C_{60}: a new form of carbon. *Nature*, 347:354–358, 1990. doi:10.1038/347354a0.

[106] T. D. Ladd, D. Maryenko, Y. Yamamoto, E. Abe and K. M. Itoh. Coherence time of decoupled nuclear spins in silicon. *Physical Review B*, 71(1):014401, 2005. doi:10.1103/PhysRevB.71.014401.

[107] R. Landauer. Irreversibility and heat generation in the computing process. *IBM Journal of Research and Development*, 5(3):183–191, 1961. doi:10.1147/rd.53.0183.

[108] H. Lee, P. Kok and J. P. Dowling. A quantum Rosetta stone for interferometry. *Journal of Modern Optics*, 49:2325–2338, 2002. doi:10.1080/0950034021000011536.

[109] D. Leibfried, E. Knill, S. Seidelin, J. Britton, R. B. Blakestad, J. Chiaverini, D. B. Hume, W. M. Itano, J. D. Jost, C. Langer, R. Ozeri, R. Reichle and D. J. Wineland. Creation of a six-atom 'Schrödinger cat' state. *Nature*, 438(7068):639–642, 2005. doi:10.1038/nature04251.

[110] A. K. Lenstra and H. W. Lenstra, Jr., editors. *The Development of the Number Field Sieve, Lecture Notes in Mathematics*, volume 1554. Springer, 1993.

[111] A. K. Lenstra, H. W. Lenstra, Jr., M. S. Manasse and J. M. Pollard. The number field sieve. In *Proceedings of the 22nd Annual ACM Symposium on Theory of Computing*, STOC '90, pages 564–572, New York, 1990. ACM. doi:10.1145/100216.100295.

[112] M. H. Levitt. *Spin Dynamics: Basics of Nuclear Magnetic Resonance*. John Wiley & Sons, 2nd edition, 2008.

[113] Y. Li, S. D. Barrett, T. M. Stace and S. C. Benjamin. Fault tolerant quantum computation with nondeterministic gates. *Physical Review Letters*, 105(25):250502, 2010. doi:10.1103/PhysRevLett.105.250502.

[114] Y. L. Lim, A. Beige and L. C. Kwek. Repeat-until-success linear optics distributed quantum computing. *Physical Review Letters*, 95(3):030505, 2005. doi:10.1103/PhysRevLett.95.030505.

[115] M. Lindgren, G. R. Eaton, S. S. Eaton, B.-H. Jonsson, P. Hammarström, M. Svensson and U. Carlsson. Electron spin echo decay as a probe of aminoxyl environment in spin-labeled mutants of human carbonic anhydrase II. *Journal of the Chemical Society, Perkin Transactions 2*,

(12):2549–2554, 1997. doi:10.1039/A702470C.

[116] S. Lloyd. Universal quantum simulators. *Science*, 273(5278):1073–1078, 1996. doi:10.1126/science.273.5278.1073.

[117] S. Lloyd. Universal quantum simulators: Correction. *Science*, 279(5354):1117, 1998. doi:10.1126/science.279.5354.1113h.

[118] B. W. Lovett and S. C. Benjamin. Comment on "Multipartite entanglement among single spins in diamond". *Science*, 323(5918):1169c, 2009. doi:10.1126/science.1168458.

[119] P. Maletinsky, S. Hong, M. S. Grinolds, B. Hausmann, M. D. Lukin, R.-L. Walsworth, M. Loncar and A. Yacoby. A robust, scanning quantum system for nanoscale sensing and imaging. 2011. arXiv:1108.4437.

[120] T. Maly, G. T. Debelouchina, V. S. Bajaj, K.-N. Hu, C.-G. Joo, M. L. Mak-Jurkauskas, J. R. Sirigiri, P. C. A. van der Wel, J. Herzfeld, R. J. Temkin and R. G. Griffin. Dynamic nuclear polarization at high magnetic fields. *Journal of Chemical Physics*, 128(5):052211, 2008. doi:10.1063/1.2833582.

[121] H. J. Mamin, T. H. Oosterkamp, M. Poggio, C. L. Degen, C. T. Rettner and D. Rugar. Isotope-selective detection and imaging of organic nanolayers. *Nano Letters*, 9(8):3020–3024, 2009. doi:10.1021/nl901466p.

[122] L. Mandel and E. Wolf. *Optical Coherence and Quantum Optics*. Cambridge University Press, 1995.

[123] M. Mannini, F. Pineider, C. Danieli, F. Totti, L. Sorace, P. Sainctavit, M.-A. Arrio, E. Otero, L. Joly, J. C. Cezar, A. Cornia and R. Sessoli. Quantum tunnelling of the magnetization in a monolayer of oriented single-molecule magnets. *Nature*, 468(7322):417–421, 2010. doi:10.1038/nature09478.

[124] D. N. Matsukevich, P. Maunz, D. L. Moehring, S. Olmschenk and C. Mon-

roe. Bell inequality violation with two remote atomic qubits. *Physical Review Letters*, 100(15):150404, 2008. doi:10.1103/PhysRevLett.100.150404.

[125] J. R. Maze, P. L. Stanwix, J. S. Hodges, S. Hong, J. M. Taylor, P. Cappellaro, L. Jiang, M. V. G. Dutt, E. Togan, A. S. Zibrov, A. Yacoby, R. L. Walsworth and M. D. Lukin. Nanoscale magnetic sensing with an individual electronic spin in diamond. *Nature*, 455(7213):644–647, 2008. doi:10.1038/nature07279.

[126] D. P. S. McCutcheon, A. Nazir, S. Bose and A. J. Fisher. Long-lived spin entanglement induced by a spatially correlated thermal bath. *Physical Review A*, 80(2):022337, 2009. doi:10.1103/PhysRevA.80.022337.

[127] P. H. Michal Horodeckia and R. Horodeckic. Separability of mixed states: necessary and sufficient conditions. *Physics Letters A*, 223(1-2):1–8, 1996. doi:10.1016/S0375-9601(96)00706-2.

[128] K. Modi, M. Williamson, H. Cable and V. Vedral. Entanglement versus classical correlations in quantum metrology with thermal states. 2010. arXiv:1003.1174.

[129] D. L. Moehring, P. Maunz, S. Olmschenk, K. C. Younge, D. N. Matsukevich, L.-M. Duan and C. Monroe. Entanglement of single-atom quantum bits at a distance. *Nature*, 449:68–71, 2007. doi:10.1038/nature06118.

[130] T. K. Moon. *Error Correction Coding: Mathematical Methods and Algorithms*. Wiley-Interscience, 2005.

[131] G. E. Moore. Cramming more components on integrated circuits. *Electronics*, 38(8), 1965. URL: ftp://download.intel.com/research/silicon/moorespaper.pdf.

[132] G. W. Morley, B. J. Herbert, S. M. Lee, K. Porfyrakis, T. J. S. Dennis, D. Nguyen-Manh, R. Scipioni, J. van Tol, A. P. Horsfield, A. Ardavan, D. G. Pettifor, J. C. Green and G. A. D. Briggs. Hyperfine structure of $Sc@C_{82}$ from ESR and DFT. *Nanotechnology*, 16(11):2469, 2005. doi:10.1088/0957-4484/16/11/001.

[133] J. J. L. Morton. *Electron Spins in Fullerenes as Prospective Qubits*. PhD thesis, University of Oxford, Department of Materials, 2006.

[134] J. J. L. Morton and B. W. Lovett. Hybrid solid-state qubits: The powerful role of electron spins. *Annual Review of Condensed Matter Physics*, 2(1):189–212, 2011. doi:10.1146/annurev-conmatphys-062910-140514.

[135] J. J. L. Morton, A. M. Tyryshkin, A. Ardavan, K. Porfyrakis, S. A. Lyon and G. A. D. Briggs. Electron spin relaxation of $N@C_{60}$ in CS_2. *Journal of Chemical Physics*, 124:014508, 2006. doi:10.1063/1.2147262.

[136] J. J. L. Morton, A. M. Tyryshkin, R. M. Brown, S. Shankar, B. W. Lovett, A. Ardavan, T. Schenkel, E. E. Haller, J. W. Ager and S. A. Lyon. Solid state quantum memory using the ^{31}P nuclear spin. *Nature*, 455:1085–1088, 2008. doi:10.1038/nature07295.

[137] M. Möttönen, J. J. Vartiainen, V. Bergholm and M. M. Salomaa. Quantum circuits for general multiqubit gates. *Physical Review Letters*, 93(13):130502, 2004. doi:10.1103/PhysRevLett.93.130502.

[138] T. Nagata, R. Okamoto, J. L. O'Brien, K. Sasaki and S. Takeuchi. Beating the standard quantum limit with four-entangled photons. *Science*, 316(5825):726–729, 2007. doi:10.1126/science.1138007.

[139] B. Naydenov, F. Dolde, L. T. Hall, C. Shin, H. Fedder, L. C. L. Hollenberg, F. Jelezko and J. Wrachtrup. Dynamical decoupling of a single-electron spin at room temperature. *Physical Review B*, 83(8):081201, 2011. doi:

10.1103/PhysRevB.83.081201.

[140] P. Neumann, J. Beck, M. Steiner, F. Rempp, H. Fedder, P. R. Hemmer, J. Wrachtrup and F. Jelezko. Single-shot readout of a single nuclear spin. *Science*, 329(5991):542–544, 2010. doi:10.1126/science.1189075.

[141] P. Neumann, N. Mizuochi, F. Rempp, P. Hemmer, H. Watanabe, S. Yamasaki, V. Jacques, T. Gaebel, F. Jelezko and J. Wrachtrup. Multipartite entanglement among single spins in diamond. *Science*, 320(5881):1326–1329, 2008. doi:10.1126/science.1157233.

[142] P. Neumann, N. Mizuochi, F. Rempp, P. Hemmer, H. Watanabe, S. Yamasaki, V. Jacques, T. Gaebel, F. Jelezko and J. Wrachtrup. Response to comment on "Multipartite entanglement among single spins in diamond". *Science*, 323(5918):1169d, 2009. doi:10.1126/science.1168459.

[143] M. A. Nielsen and I. L. Chuang. *Quantum Computation and Quantum Information*. Cambridge University Press, 2000.

[144] M. A. Nielsen and J. Kempe. Separable states are more disordered globally than locally. *Physical Review Letters*, 86(22):5184–5187, 2001. doi:10.1103/PhysRevLett.86.5184.

[145] E. Ōsawa. Superaromaticity (in japanese). *Kagaku*, 25:854–863, 1970.

[146] E. Ōsawa, H. W. Kroto, P. W. Fowler and E. Wasserman. The evolution of the football structure for the C_{60} molecule: A retrospective [and discussion]. *Philosophical Transactions: Physical Sciences and Engineering*, 343(1667):1–8, 1993. URL: http://www.jstor.org/stable/54129.

[147] Z.-Y. J. Ou and L. Mandel. Violation of Bell's inequality and classical probability in a two-photon correlation experiment. *Physical Review Letters*, 61(1):50–53, 1988. doi:10.1103/PhysRevLett.61.50.

[148] G. M. Palma, K.-A. Suominen and A. K. Ekert. Quantum computers and

dissipation. *Proceedings of the Royal Society A*, 452(1946):567–584, 1996. doi:10.1098/rspa.1996.0029.

[149] M. G. A. Paris. Quantum estimation for quantum technology. *International Journal of Quantum Information*, 7(supp01):125—137, 2009. doi:10.1142/S0219749909004839.

[150] A. Peres. Separability criterion for density matrices. *Physical Review Letters*, 77(8):1413–1415, 1996. doi:10.1103/PhysRevLett.77.1413.

[151] L. Pezzé and A. Smerzi. Mach-Zehnder interferometry at the Heisenberg limit with coherent and squeezed-vacuum light. *Physical Review Letters*, 100(7):073601, 2008. doi:10.1103/PhysRevLett.100.073601.

[152] L. Pezzé and A. Smerzi. Entanglement, nonlinear dynamics, and the Heisenberg limit. *Physical Review Letters*, 102(10):100401, 2009. doi:10.1103/PhysRevLett.102.100401.

[153] M. B. Plenio and S. Virmani. An introduction to entanglement measures. 2006. arXiv:quant-ph/0504163.

[154] M. Poggio and C. L. Degen. Force-detected nuclear magnetic resonance: recent advances and future challenges. *Nanotechnology*, 21(34):342001, 2010. doi:10.1088/0957-4484/21/34/342001.

[155] E. Ramsden. *Hall-Effect Sensors*. Newnes, 2006.

[156] R. L. Rivest, A. Shamir and L. Adleman. A method for obtaining digital signatures and public-key cryptosystems. *Communications of the ACM*, 21(2):120–126, 1978. doi:10.1145/359340.359342.

[157] M. A. Rowe, D. Kielpinski, V. Meyer, C. A. Sackett, W. M. Itano, C. Monroe and D. J. Wineland. Experimental violation of a Bell's inequality with efficient detection. *Nature*, 409:791–794, 2001. doi:10.1038/35057215.

[158] D. Rugar, R. Budakian, H. J. Mamin and B. W. Chui. Single spin detection by magnetic resonance force microscopy. *Nature*, 430:329–332, 2004. doi:10.1038/nature02658.

[159] J. J. Ryan, H. R. Bateman, A. Stover, G. Gomez, S. K. Norton, W. Zhao, L. B. Schwartz, R. Lenk and C. L. Kepley. Fullerene nanomaterials inhibit the allergic response. *The Journal of Immunology*, 179:665–672, 2007. URL: http://jimmunol.org/content/179/1/665.abstract.

[160] M. Saunders, H. A. Jimenez-Vazquez, R. J. Cross and R. J. Poreda. Stable compounds of helium and neon: He@C_{60} and Ne@C_{60}. *Science*, 259(5100):1428–1430, 1993. doi:10.1126/science.259.5100.1428.

[161] M. Schaffry, S. C. Benjamin and Y. Matsuzaki. Quantum entanglement distribution using a magnetic field sensor. 2011. arXiv:1106.0613.

[162] M. Schaffry, V. Filidou, S. D. Karlen, E. M. Gauger, S. C. Benjamin, H. L. Anderson, A. Ardavan, G. A. D. Briggs, K. Maeda, K. B. Henbest, F. Giustino, J. J. L. Morton and B. W. Lovett. Entangling remote nuclear spins linked by a chromophore. *Physical Review Letters*, 104(20):200501, 2010. doi:10.1103/PhysRevLett.104.200501.

[163] M. Schaffry, E. M. Gauger, J. J. L. Morton and S. C. Benjamin. Proposed spin amplification for magnetic sensors employing crystal defects. *Physical Review Letters*, 107(20):207210, 2011. doi:10.1103/PhysRevLett.107.207210.

[164] M. Schaffry, E. M. Gauger, J. J. L. Morton, J. Fitzsimons, S. C. Benjamin and B. W. Lovett. Quantum metrology with molecular ensembles. *Physical Review A*, 82(4):042114, 2010. doi:10.1103/PhysRevA.82.042114.

[165] M. Schaffry, B. W. Lovett and E. M. Gauger. Creating nuclear spin entanglement using an optical degree of freedom. *Physical Review A*,

84(3):032332, 2011. doi:10.1103/PhysRevA.84.032332.

[166] L. Schiff. *Quantum Mechanics Volume 1*. McGraw-Hill, 1949.

[167] R. S. Schoenfeld and W. Harneit. Real time magnetic field sensing and imaging using a single spin in diamond. *Physical Review Letters*, 106(3):030802, 2011. doi:10.1103/PhysRevLett.106.030802.

[168] E. Schrödinger. Die gegenwärtige Situation in der Quantenmechanik. *Naturwissenschaften*, 23:807–812, 1935. doi:10.1007/BF01491891.

[169] B. W. Schumacher. Quantum coding. *Physical Review A*, 51(4):2738–2747, 1995. doi:10.1103/PhysRevA.51.2738.

[170] F. Schwabl. *Quantum Mechanics*. Springer, 4th edition, 2007.

[171] A. Shaji and C. M. Caves. Qubit metrology and decoherence. *Physical Review A*, 76(3):032111, 2007. doi:10.1103/PhysRevA.76.032111.

[172] V. V. Shende, S. S. Bullock and I. L. Markov. Synthesis of quantum logic circuits. In *Proceedings of the 2005 Asia and South Pacific Design Automation Conference*, ASP-DAC '05, pages 272–275, New York, 2005. ACM. doi:10.1145/1120725.1120847.

[173] A. Shimizu and T. Miyadera. Stability of quantum states of finite macroscopic systems against classical noises, perturbations from environments, and local measurements. *Physical Review Letters*, 89(27):270403, 2002. doi:10.1103/PhysRevLett.89.270403.

[174] P. W. Shor. Algorithms for quantum computation: discrete logarithms and factoring. In *Proceedings of the 35th Annual Symposium on Foundations of Computer Science*, pages 124–134, 1994. doi:10.1109/SFCS.1994.365700.

[175] P. W. Shor. Scheme for reducing decoherence in quantum computer

memory. *Physical Review A*, 52(4):R2493–R2496, 1995. doi:10.1103/PhysRevA.52.R2493.

[176] P. W. Shor. Fault-tolerant quantum computation. In *Proceedings of the 37th Annual Symposium on Foundations of Computer Science*, pages 56–65, 1996. doi:10.1109/SFCS.1996.548464.

[177] P. W. Shor. Polynomial-time algorithms for prime factorization and discrete logarithms on a quantum computer. *SIAM Journal of Computing*, 26:1484–1509, 1997. doi:10.1137/S0097539795293172.

[178] S. Simmons, J. A. Jones, S. D. Karlen, A. Ardavan and J. J. L. Morton. Magnetic field sensors using 13-spin cat states. *Physical Review A*, 82(2):022330, 2010. doi:10.1103/PhysRevA.82.022330.

[179] C. P. Slichter. *Principles of Magnetic Resonance*. Solid states sciences 1. Springer, 3rd enlarged and updated edition, 1996.

[180] D. J. Sloop, H. Yu, T. Lin and S. I. Weissman. Electron spin echoes of a photoexcited triplet: Pentacene in p-terphenyl crystals. *Journal of Chemical Physics*, 75(8):3746–3757, 1981. doi:10.1063/1.442520.

[181] A. M. Steane. Error correcting codes in quantum theory. *Physical Review Letters*, 77:793–797, 1996. doi:10.1103/PhysRevLett.77.793.

[182] M. Stobińska, G. J. Milburn and L. Stobiński. Scalable quantum computing based on spin qubits in CNT QD. 2009. arXiv:0912.3547.

[183] J. Stolze and D. Suter. *Quantum Computing, Revised and Enlarged: A Short Course from Theory to Experiment*. Wiley-VCH, 2008.

[184] A. M. Stoneham, A. J. Fisher and P. T. Greenland. Optically driven silicon-based quantum gates with potential for high-temperature operation. *Journal of Physics: Condensed Matter*, 15(27):L447–L451, 2003. doi:10.1088/0953-8984/15/27/102.

[185] J. M. Taylor, P. Cappellaro, L. Childress, L. Jiang, D. Budker, P. R. Hemmer, A. Yacoby, R. Walsworth and M. D. Lukin. High-sensitivity diamond magnetometer with nanoscale resolution. *Nature Physics*, 4(10):810–816, 2008. doi:10.1038/nphys1075.

[186] J. Tisler, G. Balasubramanian, B. Naydenov, R. Kolesov, B. Grotz, R. Reuter, J.-P. Boudou, P. A. Curmi, M. Sennour, A. Thorel, M. Börsch, K. Aulenbacher, R. Erdmann, P. R. Hemmer, F. Jelezko and J. Wrachtrup. Fluorescence and spin properties of defects in single digit nanodiamonds. *ACS Nano*, 3(7):1959–1965, 2009. doi:10.1021/nn9003617.

[187] M. Tsang, H. M. Wiseman and C. M. Caves. Fundamental quantum limit to waveform estimation. *Physical Review Letters*, 106(9):090401, 2011. doi:10.1103/PhysRevLett.106.090401.

[188] R. R. Tucci. Rudimentary quantum compiler (2nd ed.). 1999. arXiv:quant-ph/9902062.

[189] A. M. Turing. On computable numbers, with an application to the Entscheidungsproblem. *Proceedings of the London Mathematical Society*, s2-42(1):230–265, 1937. doi:10.1112/plms/s2-42.1.230.

[190] A. M. Tyryshkin, S. Tojo, J. J. L. Morton, H. Riemann, N. V. Abrosimov, P. Becker, H.-J. Pohl, T. Schenkel, M. L. W. Thewalt, K. M. Itoh and S. A. Lyon. Electron spin coherence exceeding seconds in high purity silicon. 2011. arXiv:1105.3772.

[191] G. J. B. van den Berg, D. J. van den Heuvel, O. G. Poluektov, I. Holleman, G. Meijer and E. J. J. Groenen. Pulsed ENDOR studies at 95 GHz of the triplet state of $^{13}C_{60}$. *Journal of Magnetic Resonance*, 131(1):39–45, 1998. doi:10.1006/jmre.1997.1343.

[192] A. van den Bos. *Handbook of Measurement Science*. Wiley, 1982.

[193] J. J. Vartiainen, M. Möttönen and M. M. Salomaa. Efficient decomposition of quantum gates. *Physical Review Letters*, 92:177902, 2004. doi:10.1103/PhysRevLett.92.177902.

[194] J. von Neumann. *Mathematische Grundlagen der Quantenmechanik*. Springer, 1932.

[195] R. Ward, A. Bowman, E. Sozudogru, H. El-Mkami, T. Owen-Hughes and D. G. Norman. EPR distance measurements in deuterated proteins. *Journal of Magnetic Resonance*, 207(1):164–167, 2010. doi:10.1016/j.jmr.2010.08.002.

[196] R. F. Werner. Quantum states with Einstein-Podolsky-Rosen correlations admitting a hidden-variable model. *Physical Review A*, 40(8):4277–4281, 1989. doi:10.1103/PhysRevA.40.4277.

[197] T. Wilk, S. C. Webster, A. Kuhn and G. Rempe. Single-atom single-photon quantum interface. *Science*, 317:488–490, 2007. doi:10.1126/science.1143835.

[198] P. Wocjan and J. Yard. The Jones polynomial: quantum algorithms and applications in quantum complexity theory. 2007. arXiv:quant-ph/0603069.

[199] J. Wong-Ekkabut, S. Baoukina, W. Triampo, I.-M. Tang, D. P. Tieleman and L. Monticelli. Computer simulation study of fullerene translocation through lipid membranes. *Nature Nanotechnology*, 3:363–368, 2008. doi:10.1038/nnano.2008.130.

[200] W. K. Wootters. Entanglement of formation of an arbitrary state of two qubits. *Physical Review Letters*, 80(10):2245–2248, 1998. doi:10.1103/PhysRevLett.80.2245.

[201] W. K. Wootters and W. H. Zurek. A single quantum cannot be cloned.

Nature, 299:802–803, 1982. doi:10.1038/299802a0.

[202] J. Wrachtrup and F. Jelezko. Processing quantum information in diamond. *Journal of Physics: Condensed Matter*, 18(21):S807, 2006. doi:10.1088/0953-8984/18/21/S08.

[203] J. Wrachtrup, S. Y. Kilin and A. P. Nizovtsev. Quantum computation using the ^{13}C nuclear spins near the single NV defect center in diamond. *Optics and Spectroscopy*, 91(3):429–437, 2001. doi:10.1134/1.1405224.

[204] T. Yago, G. Link, G. Kothe and T.-S. Lin. Pulsed electron nuclear double resonance studies of the photoexcited triplet state of pentacene in p-terphenyl crystals at room temperature. *Journal of Chemical Physics*, 127(11):114503, 2007. doi:10.1063/1.2771145.

[205] Z. Yoshida and E. Ōsawa. *Aromaticity (in Japanese)*. Kagaku Dojin, 1971.

[206] K. Yun, S. Park, H. Pyo, S. Kim and S. Lee. Regiospecific orientation of single-chain antibody and atomic force microscope (AFM) images. *Biotechnology and Bioprocess Engineering*, 4(1):72–77, 1999. doi:10.1007/BF02931919.

[207] P. Zanardi, C. Zalka and L. Faoro. Entangling power of quantum evolutions. *Physical Review A*, 62(3):030301(R), 2000. doi:10.1103/PhysRevA.62.030301.

[208] N. Zhao, J.-L. Hu, S.-W. Ho, J. T. K. Wan and R. B. Liu. Atomic-scale magnetometry of distant nuclear spin clusters via nitrogen-vacancy spin in diamond. *Nature Nanotechnology*, 6:242–246, 2011. doi:10.1038/nnano.2011.22.

[209] V. Zimmermann, M. Schwoerer and H. C. Wolf. Endor of triplet fluorene in fluorene (X-traps). Intramolecular hyperfine structure. *Chemical Physics Letters*, 31(3):401–405, 1975. doi:10.1016/0009-2614(75)85051-2.

[210] M. Zwierz, C. A. Pérez-Delgado and P. Kok. General optimality of the Heisenberg limit for quantum metrology. *Physical Review Letters*, 105(18):180402, 2010. doi:10.1103/PhysRevLett.105.180402.